Non-perturbative Aspects of *Sp(2N)* Gauge Theories

Jack Holligan

Department of Physics

Swansea University

Submitted to Swansea University in fulfilment of the requirements for the Degree of Doctor of Philosophy

Swansea University
Prifysgol Abertawe

Abstract

Yang-Mills theories based on the symplectic groups – denoted by $Sp(2N)$ – are interesting for both theoretical and phenomenological reasons. $Sp(2N)$ theories with two fundamental Dirac fermions give rise to pseudo-Nambu-Goldstone bosons which can be interpreted as a composite Higgs particle. This framework can describe the existing Higgs boson without the need for unnatural fine-tuning. This justifies a programme of wider investigations of $Sp(2N)$ gauge theories aimed at understanding their general behaviour. In this work, we study the glueball mass spectrum for $Sp(2N)$ Yang-Mills theories using the variational method applied to Monte-Carlo generated gauge configurations. This is carried out both for finite N and in the limit $N \to \infty$. The results are compared to existing results for $SU(N)$ Yang-Mills theories, again, for finite- and large-N. Our glueball analysis is then used to investigate some conjectures related to the behaviour of the spectrum in Yang-Mills theories based on a generic non-Abelian gauge group $\mathcal{G}$. We also find numerical evidence that $Sp(2N)$ groups confine both for finite and large N. As well as studying the glueball spectrum, we examine the quenched-meson spectrum for fermions in the fundamental, antisymmetric and symmetric representations for $N = 2$ and $N = 3$. This study enables us to provide a first account of how the related observables vary with N. The investigations presented in this work contribute to our understanding of the non-perturbative dynamics of $Sp(2N)$ gauge theories in connection with Higgs compositeness and, more in general, with fundamental open problems in non-Abelian gauge theories such as confinement and global symmetry breaking.

Declaration

This work has not previously been accepted in substance for any degree and is not being concurrently submitted in candidature for any degree.

Signed: [redacted] ..... (candidate)

Date: 17th Aug 2021

Statement 1

This thesis is the result of my own investigations, except where otherwise stated. Where correction services have been used, the extent and nature of the correction is clearly marked in a footnote(s).

Other sources are acknowledged by footnotes giving explicit references. A bibliography is appended.

Signed: [redacted] ..... (candidate)

Date: 17th Aug 2021

Statement 2

I hereby give consent for my thesis, if accepted, to be available for photocopying and for inter-library loan, and for the title and summary to be made available to outside organisations.

Signed: [redacted] ..... (candidate)

Date: 17th Aug 2021

Contents

List of Figures

List of Tables

Acknowledgements

Huge thanks are due, first to Professors Biagio Lucini and Maurizio Piai, my two supervisors, who have been unwavering in their support both personally and academically with this work. I have gained a huge range of skills and knowledge since I began which will be invaluable throughout my career.

This work was funded by both the Science and Technology Facilities Council (STFC) and the Physics Department at Swansea University. Without financial help from these institutions, I would not have been able to carry out this PhD. The computations for this thesis were carried out on the Supercomputing Wales cluster using HiRep code written by Claudio Pica and other members of the collaboration.

I am also immeasurably grateful to Davide Vadacchino and Ed Bennett who gave enormous assistance to me when I both wrote and used computer code. The seeds of my programming knowledge are to be found in the tasks I carried out in the first year of this project and their assistance has helped me refine these skills further.

Finally, great thanks are due to my friend Robert Clayton who not only gave me a home during the Coronavirus pandemic. His company as well as that of Victoria Isaac has supported me mentally and academically for several years. In addition, my parents have provided tremendous support of all kinds throughout this PhD especially during the Coronavirus pandemic.

Notations and Conventions

Throughout this thesis we use Natural Units:

$$\hbar = c = 1, \tag{0.0.1}$$

where the above quantities are – from left to right – the reduced Planck constant and the speed of light. All dimensionful quantities can be measured in units of mass to some power.

The Kronecker-Delta symbol is defined as

$$\delta_{ij} = \begin{cases} 1 & i = j \\ 0 & \text{otherwise} \end{cases}. \tag{0.0.2}$$

The notations for quantities and operations on the hypercubic lattice are shown in table 1.

The plaquette is defined in terms of four lattice links:

$$U_{\mu\nu}(x) = U_\mu(x) U_\nu(x + \hat{\mu}) U_\mu^\dagger(x + \hat{\nu}) U_\nu^\dagger(x). \tag{0.0.3}$$

The quantity $\hat{\mu}$ is the unit vector in the direction of μ. This shape is demonstrated in

Quantity/Operation	Symbol
Lattice spacing	a
Lattice width	L
Number of sites in each spatial direction	N_s
Number of sites in temporal direction	N_t
Number of charges/colours	N_c
String tension	σ
Coupling strength	g
Inverse coupling	$\beta = 2N_c/g^2$
Unit vector in μ direction (μ=1, 2, 3, 4)	$\hat{\mu}$
Lattice link from site x in direction μ	$U_\mu(x)$
Plaquette at site x in (μ, ν) plane	$U_{\mu\nu}(x)$
Real part	$\Re$
Trace	tr
Dimension	dim
Sum of staples	Σ

Table 1: Lattice Definitions.

fig. 2.1.

A lattice link, $U_\mu(x)$, has six associated staples. Their sum is given by

$$\Sigma(U_\mu(x)) = \sum_{\nu \neq \mu} (U_\nu(x+\hat{\mu})U_\mu^\dagger(x+\hat{\nu})U_\nu^\dagger(x) + U_\nu^\dagger(x+\hat{\mu}-\hat{\nu})U_\mu^\dagger(x-\hat{\nu})U_\nu(x-\hat{\mu})) \quad (0.0.4)$$

where the sum over ν goes from 1 to 4 excluding the value of μ. A diagram of the staples in given in fig. 2.2.

The notation for unit vectors follows the convention that Greek letters run from 1 to 4 (e.g. $\hat{\mu}$), whereas Roman letters run from 1 to 3 (e.g. $\hat{i}$). This distinction is important for the description of the blocking and smearing algorithms in section 3.3.

The symplectic groups are commonly denoted by $Sp(2N)$ in order to emphasise that the corresponding matrices must be of even dimension. In some cases, such as

Casimir scaling in section 3.7, it is convenient to denote the group by the number of charges associated with it: $Sp(N_c)$. This means that both $Sp(N_c)$ and, say, $SU(N_c)$ have N_c charges rather than the former having $2N$ and the latter having N.

The notations defined in this section are used throughout this thesis to avoid repetition. Quantities will be identified but they will not be defined unless the notation in context conflicts with the notation in this section.

Introduction

The Standard Model (SM) of particle physics is our current understanding of Nature at the subatomic scale. It is a Quantum Field Theory (QFT) with tremendous predictive power, but one that still leaves some open problems. The SM cannot be a complete description of Nature for several reasons: it does not explain the gravitational force, several of its couplings are not UV safe and it does not contain a dark matter candidate. As such, we must treat the SM as an Effective Field Theory (EFT) valid up to some energy scale Λ_{SM}; above this energy scale, new physics must emerge. It is natural to estimate quantum corrections to observables using Λ_{SM} as a regulator. If this is the case, the Higgs potential receives a quadratically divergent renormalisation. Strong cancellations between calculable and non-calculable terms are required to make the Electroweak (EW) scale far less than the SM cutoff. This introduces a new problem known as the *hierarchy problem*. One instance of cancellations concerns the mass of the Higgs boson. For the SM to produce the observed Higgs mass of 125 GeV requires an extreme level of fine-tuning. Loop corrections to the Higgs mass shown in fig. 1.1 diverge and, thus, require counter-terms to keep the mass finite. This is a common feature of QFTs but in order to produce the observed mass of the Higgs boson, the counter-terms must cancel the divergences to an implausibly high precision. This is known as the *naturalness problem*; such a phenomenal coincidence of two unrelated numbers seems

highly unlikely. The motivation for the studying of the symplectic groups – denoted by $Sp(2N)$ – is that these models have the potential to describe the Higgs boson as a composite particle which would reduce the need for fine-tuning [1–4] and we use the lattice to investigate them. A model that can give rise to a composite Higgs is based on the $SU(4) \to Sp(4)$ global symmetry breaking [1]. The motivation largely stems from Occam's razor. This symmetry breaking pattern is a simple mechanism that satisfies the necessary requirement of being compatible with phenomenology [5]. One of the main activities in lattice implementations of physics beyond the SM is to test the viability of this mechanism.

In order to gain a better understanding of the $Sp(2N)$ groups we study them in their own right as pure gauge models, without introducing dynamical fermions. We do not know *a priori* which value of N is best suited for a composite Higgs model so we study several values of N as well as the behaviour as $N \to \infty$. Studies of these models are ongoing [5–15]. This allows us to get an idea of how $Sp(2N)$ gauge theories change with N as well as to highlight any features that are common to all values of N. We study the glueball mass spectrum for finite N, and extrapolate to the large-N limit. We also study the quenched meson spectrum for finite N. The exploration of these theories is the topic of this thesis.

Solving a strongly coupled Yang-Mills theory is an old and formidable challenge for particle physicists. The advent of Lattice Field Theory (LFT) in 1974 by Ken Wilson [16] made previously intractable calculations amenable to supercomputers. This has allowed us to gain tremendous insight into theories that would otherwise be beyond our reach. In this thesis we use the techniques of LFT to explore the behaviour of Yang-Mills theories based on the symplectic groups. Lattice studies of candidate composite Higgs Models (CHM) have been carried out before with $SU(2)$ [17–23], $SU(4)$ [24–28] and $Sp(4)$ symmetries [5, 13, 29].

In Chapter 1, we give a more detailed summary of the motivation for the $Sp(2N)$ gauge theories. Firstly, we describe the Higgs sector of the SM as well as the origin of the naturalness problem. Composite Higgs models are discussed as a possible resolution to the naturalness problem; in particular, we discuss chiral symmetry breaking and the Higgs as a pseudo-Nambu-Goldstone boson (PNGB) which has been discussed before [30,31]. We then describe the EFT of $Sp(4)$ with 2 fermion flavours in the fundamental representation and demonstrate that symmetry breaking patterns can give rise to a more natural explanation for the low mass of the Higgs.

We then demonstrate how to implement Yang-Mills and, specifically, symplectic groups on the lattice, which is a robust first-principle approach to understand the non-perturbative behaviour of such theories. After exposing the general principles of the lattice formulation of gauge theories, we describe the method of generating random elements of $Sp(2N)$ by the generation of its $SU(2)$ subgroups.

Chapter 3 describes the methodology of computing glueball masses and string tensions on the lattice. These are key probes of the dynamics of a Yang-Mills theory. As well as this, we demonstrate how the discrete results are extrapolated to the continuum, how finite volume is extrapolated to the thermodynamic limit as well as how finite N is extrapolated to large N. Finally, it contains the results from lattice calculations of the glueball mass spectrum as well as string tension in pure $Sp(2N)$ Yang-Mills. Results are displayed for $N = 1, 2, 3$ and 4 as well as the extrapolation to $N \to \infty$.

Chapter 4 describes the addition of quenched fermions to the lattice and the method of the computation of meson masses. The quenched calculations provide an initial limit towards which we can evaluate dynamical calculations which are computationally more expensive. Although our model requires two flavours of fermion in the fundamental representation, the quenched calculations apply to a generic number of flavours. As a first step towards a large-N extrapolation, results are stated for $N = 2$

and 3 each in the fundamental, symmetric and antisymmetric representations.

We summarise our findings in Chapter 5 as well as discussing future avenues of research. In addition, we discuss motives for studying symplectic Yang-Mills besides composite Higgs models.

The appendices discuss more technical details related to the calculations reported in this work. Appendix A explicitly states a set of generators of the group $SU(4)$, a subset of which is the generators of $Sp(4)$. These generators are stated in order to describe in better detail the global symmetry breaking $SU(4) \to Sp(4)$. The generators of $SU(4)$ are also stated in the form of generalised Gell-Mann matrices. Appendix B derives the block structure of all $Sp(2N)$ matrices. The computation of meson masses requires finding a plateau in a plot of effective masses. Appendix C describes an algorithm that seeks the optimum fit-range for the computation of the meson masses, which was used in this thesis.

Chapter 1

Sp(2N) Gauge Theories as a Framework for Higgs Compositeness

Higgs compositeness is a viable mechanism that is, in principle, a way to soften the hierarchy problem of the SM (i.e. why the Higgs boson does not have a mass at the Planck scale) and the little hierarchy problem (i.e. why we do not see particles other than the Higgs at the EW scale). However, only a first-principle non-perturbative study of concrete realisations of these ideas can ultimately enable us to assess their robustness.

Chiral symmetry breaking (as demonstrated in section 1.2.1) is responsible for the parametrically small masses of the pions in QCD. Composite Higgs models are based on the same mechanism thus providing an elegant symmetry argument for the observed low mass of the Higgs boson.

There are several patterns of chiral symmetry breaking (χSB). See, for example, [2, 32]. Here, we focus on $SU(4) \to Sp(4)$, which has not been studied in much detail

on the lattice until recently, in relation to Higgs compositeness. This pattern, which arises when the gauge group is $Sp(2N)$ and the theory has two fundamental flavours of Dirac fermions, motivates the study of $Sp(2N)$ EFT and chiral symmetry breaking in such models [32].

In addition, it is not known quantitatively how the physics of $Sp(2N)$ depends on N. For this reason we study several values of finite N as well as the limit of $N \to \infty$ in order to understand this behaviour. In this chapter we describe the need for the Higgs mechanism and the origin of the naturalness problem. We go on to describe composite Higgs models and how the method of χSB can be used to generate parametrically small masses. This method is then applied to $Sp(4)$ EFT. Finally, we describe the behaviour and motive of Yang-Mills theories in the limit of an infinite number of charges ("large-N").

1.1 The Standard Model and its Limitations

The SM describes the three non-gravitational forces (Weak, Strong and Electromagnetic) in the language of QFT. One of the greatest achievements of the SM is its prediction of the anomalous magnetic moment of the electron. This is the deviation of the magnetic moment of the electron from its value as computed with classical physics and has been computed perturbatively [33] as well as numerically. The numerical [34] and experimental [35] values are, respectively,

$$a_e(\text{num}) = 1159652182.032(13)(12)(720) \times 10^{-12}, \tag{1.1.1}$$

$$a_e(\text{exp}) = 1159652180.91(26) \times 10^{-12}. \tag{1.1.2}$$

The SM requires a mass-giving field (for reasons explained in section 1.1.1) which, itself, predicts the existence of the Higgs boson. The existence of this particle was confirmed by the ATLAS [36] and CMS [37] collaborations in 2012.

Despite this unparalleled success, there remain some issues with the SM one of which is the mass of the Higgs boson. Below, we describe the Higgs field and why the fine-tuning issue arises.

1.1.1 The Need for the Higgs Mechanism

The SM possesses an $SU(3)_C \otimes SU(2)_L \otimes U(1)_Y$ gauge symmetry corresponding to colour, weak-isospin and hypercharge, respectively. The fact that the gauge bosons for the weak force ($W^{\pm}$ and Z) possess mass poses a problem for the aforementioned symmetry. An explicit mass term added to the SM Lagrangian would destroy the gauge invariance.

A mechanism proposed by Peter Higgs [38, 39] as well as (and independently) Brout, Englert [40], Anderson [41] and many others demonstrates that a scalar field inducing spontaneous symmetry breaking (SSB) can endow gauge-bosons with mass without sacrificing gauge invariance. Since the early 1960s it had been understood that when a scalar field undergoes SSB there exists one massless scalar particle for every symmetry generator lost in the process. This is known as Goldstone's theorem [42, 43] and the massless particles are known as Nambu-Goldstone bosons (NGB). Since no massless scalar particles had been observed in the Electroweak sector of the SM this was thought to preclude the possibility of SSB within the Standard Model itself.

The Higgs mechanism (as it has become known) manages to circumvent this issue by showing that the NGBs are "eaten" by the gauge fields causing the gauge bosons to acquire mass. The massless scalars become the longitudinal components

of the (otherwise massless) gauge boson polarisations. In addition to explaining the masses of the Weak bosons, the theory predicts the existence of a new scalar particle: the now famous Higgs boson.

Before SSB, the Standard Model contains the three weak-isospin fields, $\mathbf{W}_\mu$ with coupling g_W, and the hypercharge field, B_μ with coupling g'. $\mathbf{W}_\mu$ and B_μ correspond to $SU(2)_\mathrm{L}$ and $U(1)_\mathrm{Y}$, respectively. The Higgs sector of the SM has the Lagrangian density[1]

$$\mathcal{L}_\mathrm{Higgs} = (D_\mu\phi)^\dagger(D^\mu\phi) - \mu^2(\phi^\dagger\phi) - \lambda(\phi^\dagger\phi)^2 \tag{1.1.3}$$

with $\mu^2 < 0$ and $\lambda > 0$. Let us explain eq. (1.1.3).

- The complex, two-component Higgs doublet $\phi = \begin{bmatrix} \phi^+ \\ \phi^0 \end{bmatrix} = \frac{1}{\sqrt{2}} \begin{bmatrix} \phi_1 + i\phi_2 \\ \phi_3 + i\phi_4 \end{bmatrix}$ where the four $\{\phi_i\}$ fields are real

- The covariant derivative $D_\mu = \partial_\mu + ig_W\boldsymbol{\tau}\cdot\mathbf{W}_\mu + ig'\frac{Y}{2}B_\mu$. The $\{\tau^i\}$ terms are the three Pauli matrices each multiplied by a factor of $1/2$; they are normalised to $\mathrm{tr}(\tau^i\tau^j) = \frac{1}{2}\delta_{ij}$. The Y term is given by $Y = 2(Q - I_3)$ with Q being electric charge and I_3 being the third component of isospin. In full

$$D_\mu = \frac{1}{2}\begin{bmatrix} 2\partial_\mu + ig_W W_\mu^{(3)} + ig'YB_\mu & ig_W\left(W_\mu^{(1)} - iW_\mu^{(2)}\right) \\ ig_W\left(W_\mu^{(1)} + iW_\mu^{(2)}\right) & 2\partial_\mu - ig_W W_\mu^{(3)} + ig'YB_\mu \end{bmatrix} \tag{1.1.4}$$

- λ is the Higgs self-coupling

- μ is related to the Higgs mass, m_H, via $m_H^2 = -2\mu^2$.

[1] Hereafter, all Lagrangian densities are referred to as Lagrangians for brevity

If we define the vacuum expectation value (VEV) of the Higgs doublet as

$$\langle 0|\phi|0\rangle = \frac{1}{\sqrt{2}} \begin{bmatrix} 0 \\ v \end{bmatrix} \tag{1.1.5}$$

we can rewrite the Higgs doublet in the unitary gauge as [44]

$$\phi = \frac{1}{\sqrt{2}} \begin{bmatrix} 0 \\ v + h(x) \end{bmatrix}. \tag{1.1.6}$$

The new scalar, $h(x)$, is the Higgs field.

1.1.2 The Little Hierarchy Problem

The mass of the Higgs boson poses a new problem. The SM is valid up to some cutoff, Λ_{SM}, and the loop corrections to the Higgs mass, m_H, are dependent upon this quantity. These loop-corrections to m_H (denoted by δm_H) give rise to quadratic divergences which necessitate quadratic counter terms to reproduce the measured mass. The one-loop diagrams are shown in fig. 1.1.

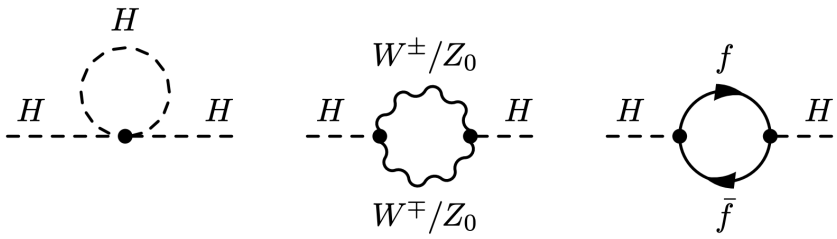

Figure 1.1: One-loop corrections to the mass of the Higgs boson.

The one-loop correction to the Higgs boson mass (squared) is given by [8]

$$\delta m_H^2 = \frac{3\Lambda_{\text{SM}}^2}{8\pi^2}\left[y_t^2 - g_W^2\left(\frac{1}{4} + \frac{1}{8\cos^2\theta_W}\right) - \lambda\right] \tag{1.1.7}$$

where

- Λ_{SM} is the SM cutoff (i.e. the energy level up to which the Standard Model EFT is valid);
- y_t is the Higgs coupling to the top-quark (which is far greater than the Higgs coupling to each of the other fundamental fermions);
- θ_W is the Weinberg angle or weak-mixing angle;
- λ is the Higgs self-coupling as in eq. (1.1.3).

The absence of new physics at the tera electron-volt (TeV) scale pushes the quantity Λ_{SM} ever higher relative to the symmetry breaking scale. Consequently, the term required to cancel the divergence also increases in magnitude. If the correction to the squared mass of the Higgs within the SM is denoted by $\delta_{\text{SM}} m_H^2$ and the fine-tuning scale, Δ, is defined as $\Delta \equiv \frac{\delta_{\text{SM}} m_H^2}{m_H^2}$ as in [8] then

$$\Delta \approx \frac{3y_t^2\Lambda_{\text{SM}}^2}{8\pi^2 m_H^2} \approx \left(\frac{\Lambda_{\text{SM}}}{450\text{GeV}}\right)^2, \tag{1.1.8}$$

where the contribution from the top quark dominates due to its large Yukawa coupling and colour multiplicity. If the SM is valid up to the scale of Grand Unification ($\Lambda_{\text{SM}} \sim 10^{15}$ GeV), then $\Delta \sim 10^{24}$ [8]. Therefore, in order to reproduce the measured mass of 125 GeV, we need two terms to cancel out correctly to one part in 10^{24} since the quantity Λ_{SM} is many orders of magnitude larger than the Higgs mass. Such extreme fine-

tuning seems highly unlikely to occur. We must either accept that such a phenomenal coincidence has occurred in Nature or seek an alternative model. Such a new model must eliminate the need for fine-tuning while also producing the current theory of the EW sector (for which there is a great deal of experimental evidence).

1.2 Composite Higgs Models

As reported earlier, Goldstone's theorem states that an exact symmetry undergoing spontaneous breaking gives rise to massless scalar particles known as Nambu-Goldstone bosons. A corollary is that when the spontaneously broken symmetry is approximate (as opposed to exact), the would-be Goldstone bosons are no longer massless but, instead, have a parametrically small mass controlled by the coupling of the symmetry breaking term. These are known as pseudo-Nambu-Goldstone bosons. This is a more natural explanation for the low mass of a particle compared to extreme fine-tuning.

1.2.1 Chiral Symmetry Breaking

Having described the little hierarchy problems in the SM, we discuss composite Higgs models and, in particular, chiral symmetry breaking as a fundamental mechanism for Electroweak symmetry breaking (EWSB) through a novel interaction. A concrete example of PNGBs, which we will review to set the scene for strongly interacting extensions of the Standard Model, is given by the pions of QCD. At very low energies, the up and down quarks are the only ones light enough to be produced. We first demonstrate the existence of chiral symmetry for strictly massless quarks. Even in this case, χSB occurs causing the quarks to acquire mass.

We then include an explicit mass term and demonstrate that the NGBs acquire

a small mass which we interpret as the pions of QCD. (This approximate flavour symmetry can be supplemented with the strange quark as in the Eightfold Way [45] giving rise to the $K^{\pm}$, K^0, $\bar{K}^0$ and η mesons.)

1.2.2 Massless, Low-Energy QCD

For massless quarks, the Lagrangian is

$$\mathcal{L} = i\bar{q}\not{D}q - \frac{1}{4}F^a_{\mu\nu}F^{a\mu\nu} \quad , \quad q = \begin{bmatrix} u \\ d \end{bmatrix} \tag{1.2.1}$$

where u and d, respectively, are the spinors for up and down quarks; $F^a_{\mu\nu}$ is the gluon field strength tensor; and D_μ is the covariant derivative of QCD.

We can separate the spinors into left- and right-handed components using the corresponding operators:

$$P_L\psi = \tfrac{1}{2}(\mathbb{1} - \gamma_5)\psi = \psi_L, \tag{1.2.2}$$

$$P_R\psi = \tfrac{1}{2}(\mathbb{1} + \gamma_5)\psi = \psi_R. \tag{1.2.3}$$

The matrix γ_5 is given in terms of the other four Dirac matrices:

$$\gamma_5 = i\gamma_0\gamma_1\gamma_2\gamma_3. \tag{1.2.4}$$

Decomposing q into its left- and right-handed components gives us

$$\mathcal{L} = i\bar{q}_L\not{D}q_L + i\bar{q}_R\not{D}q_R - \frac{1}{4}F^a_{\mu\nu}F^{a\mu\nu}. \tag{1.2.5}$$

There is no mixing of the left- and right-handed components. This means that the

Symmetry	Noether current
$U(1)_L$	$j^{\mu}_L = \bar{q}_L \gamma^{\mu} q_L$
$U(1)_R$	$j^{\mu}_R = \bar{q}_R \gamma^{\mu} q_R$
$SU(2)_L$	$j^{\mu a}_L = \bar{q}_L \gamma^{\mu} \tau^a q_L$
$SU(2)_R$	$j^{\mu a}_R = \bar{q}_R \gamma^{\mu} \tau^a q_R$

Table 1.1: Left- and right-handed Noether currents of low-energy QCD.

Symmetry	Noether current
$U(1)_V$	$j^{\mu} = \bar{q} \gamma^{\mu} q$
$U(1)_A$	$j^{\mu 5} = \bar{q} \gamma^{\mu} \gamma^5 q$
$SU(2)_V$	$j^{\mu a} = \bar{q} \gamma^{\mu} \tau^a q$
$SU(2)_A$	$j^{\mu 5 a} = \bar{q} \gamma^{\mu} \gamma^5 \tau^a q$

Table 1.2: Vector and axial-vector Noether currents of low-energy QCD.

Lagrangian possesses a $U(2)_L \otimes U(2)_R$ symmetry:

$$q_L \longrightarrow U_L q_L \tag{1.2.6}$$

$$q_R \longrightarrow U_R q_R, \tag{1.2.7}$$

where U_L and U_R are independent elements of the $U(2)$ group. This symmetry can be decomposed into:

$$SU(2)_L \otimes SU(2)_R \otimes U(1)_L \otimes U(1)_R. \tag{1.2.8}$$

By Noether's theorem, there is a conserved current associated with each continuous symmetry, and these are shown in table 1.1. The left- and right-handed components of the conserved currents can be combined to make vector (right plus left) and axial-vector (right minus left) currents and these are shown in table 1.2. In both cases, the $\{\tau^a\}$ are the three Pauli matrices each divided by two. The $\{\tau^a\}$ matrices are normalised such that $\mathrm{tr}(\tau^a \tau^b) = \frac{1}{2}\delta^{ab}$.

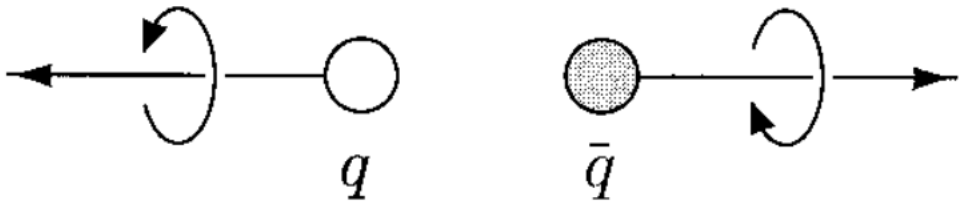

Figure 1.2: A quark antiquark pair produced from the vacuum whose linear- and angular-momentum are equal and opposite. This results in a net increase in chiral charge. The image has been taken from [46].

Since the quarks are massless in this example, they can be produced from the vacuum in quark-antiquark pairs at little energy cost. In order to conserve linear- and angular-momentum, they must be moving in opposite directions and have opposite spins. Consequently, the produced quarks must both have their spin and linear momentum either aligned or anti-aligned. This results in the two quarks either being both right-handed or both left-handed causing an increase in magnitude of chiral charge. The symmetry that preserves chiral charge has, thus, been broken by the vacuum. This condensate of quark-antiquark pairs is quantified as [46]

$$\langle 0|\bar{q}q|0\rangle = \langle 0|\bar{q}_L q_R + \bar{q}_R q_L|0\rangle \neq 0. \tag{1.2.9}$$

Because the left- and right-handed terms mix, the full $U(2) \otimes U(2)$ symmetry no longer holds and the quarks acquire an effective mass as they move through the condensate of quark-antiquark pairs. $SU(2)_A$ symmetry is spontaneously broken giving rise to 3 NGBs as per Goldstone's theorem:

$$SU(2)_A \otimes SU(2)_V \otimes U(1)_V \longrightarrow SU(2)_V \otimes U(1)_V. \tag{1.2.10}$$

The $U(1)_A$ current is broken by the chiral anomaly [47–49] so it is not included in eq. (1.2.10). This is the reason the η' meson has a relatively large mass compared to the other light mesons of the Eightfold Way.

We refer to the three Goldstone bosons in this case as pions, but with the reminder that the real pions of QCD are not massless. Inserting the $j^{\mu 5a}$ current between the vacuum and a pion state gives [50]:

$$\left\langle 0\middle|j^{\mu 5a}(x)\middle|\pi^b(p)\right\rangle = ip^\mu f_\pi \delta^{ab} e^{-ip\cdot x}. \tag{1.2.11}$$

Given the conservation of the axial-isospin current, we find:

$$\begin{aligned} \left\langle 0\middle|\partial_\mu j^{\mu 5a}(x)\middle|\pi^b(p)\right\rangle &= p^2 f_\pi \delta^{ab} e^{-ip\cdot x} && (1.2.12)\\ \implies 0 &= p^2 f_\pi \delta^{ab} e^{-ip\cdot x}, && (1.2.13) \end{aligned}$$

which, as expected, only holds if $p^2 = 0 \iff m_\pi = 0$.

Using the methods of the σ model first described in [51] and following the method of [50] we can describe the dynamics of the spontaneously broken field. We introduce a new set of scalar fields $\Sigma_{ij}(x)$ that transform as

$$\Sigma' = g_L \Sigma g_R^\dagger \quad , \quad \Sigma^{\dagger\prime} = g_R \Sigma^\dagger g_L^\dagger \ . \tag{1.2.14}$$

Expanding Σ around the VEV, we can write the full fields in terms of a modular field, σ, and angular fields, $\{\pi^a\}$, in a similar fashion to eq. (1.1.6):

$$\Sigma = \frac{v + \sigma(x)}{\sqrt{2}} \exp\left(\frac{2i}{f_\pi}\pi^a \tau^a\right) \quad , \quad \langle \Sigma \rangle = \frac{v}{\sqrt{2}}. \tag{1.2.15}$$

Decoupling σ from the π^a fields and defining

$$U(x) = \exp\left(\frac{2i}{f_\pi}\pi^a\tau^a\right) \tag{1.2.16}$$

we then write the most general Lagrangian in terms of $U(x)$. The fact that $U^\dagger U = \mathbb{1}$ means that the only relevant terms are those that contain derivatives. In order to maintain the gauge invariance, we must use covariant derivatives of QCD, D_μ, as opposed to ordinary derivatives, ∂_μ.

A term containing a single derivative would be of the form

$$\text{tr}\left[UD_\mu U^\dagger\right], \tag{1.2.17}$$

but this evaluates to 0 due to the trace term and the presence of a single generator matrix brought down by the derivative. The terms containing two derivatives are

$$\text{tr}\left[(UD_\mu U^\dagger)^2\right], \quad \text{tr}\left[(D_\mu U)(D^\mu U^\dagger)\right] \tag{1.2.18}$$

but the cyclic property of the trace operator as well as the fact that $U\partial_\mu U^\dagger = -(\partial_\mu U)U^\dagger$ means that they are, in fact, equivalent. Thus the simplest non-trivial term is [50, 52]

$$\mathcal{L} = \frac{f_\pi^2}{4}\,\text{tr}[(D_\mu U)(D^\mu U^\dagger)]. \tag{1.2.19}$$

where, for reasons that will become clear, the coefficient has been included. Expanding out this term yields

$$\frac{f_\pi^2}{4}\,\text{tr}[(D_\mu U)(D^\mu U^\dagger)] = \text{tr}\{(\partial_\mu\pi)(\partial^\mu\pi)\} + \frac{1}{3f_\pi^2}\,\text{tr}\{[\partial_\mu\pi,\pi]\,[\partial^\mu\pi,\pi]\} + \mathcal{O}(\pi^6), \tag{1.2.20}$$

which shows that we can create a theory of interacting pions.

1.2.3 Chiral Symmetry Breaking with low-mass quarks

In reality, the quarks of QCD each possess a small mass. The Lagrangian in this case takes the form:

$$\mathcal{L} = i\bar{q}\not{D}q - \bar{q}Mq - \frac{1}{4}F^a_{\mu\nu}F^{a\mu\nu} \tag{1.2.21}$$

where M is the mass matrix:

$$M = \begin{bmatrix} m_u & 0 \\ 0 & m_d \end{bmatrix}. \tag{1.2.22}$$

We can treat the constant matrix, M, as a field in its own right; this is known as a spurion field. We know that the chiral symmetry is spontaneously broken and we quantify this via

$$\langle 0|\bar{q}q|0\rangle = v^3, \tag{1.2.23}$$

where v has mass-dimension 1. The simplest Lagrangian term for the masses is

$$\mathcal{L}_{\text{mass}} = \frac{v^3}{2}\,\text{tr}(MU + M^\dagger U^\dagger) \tag{1.2.24}$$

where the coefficient is inserted to reproduce the VEV of eq. (1.2.23). Expanding out this term gives us

$$\mathcal{L}_{\text{mass}} \;=\; v^3(m_u + m_d) - \frac{v^3}{2f_\pi^2}(m_u + m_d)\pi^a\pi^a + \mathcal{O}(\pi^3). \tag{1.2.25}$$

Combining the above with eq. (1.2.20) gives us

$$\mathcal{L}_\chi = \frac{1}{2}(\partial_\mu\pi^a)(\partial^\mu\pi^a) + v^3(m_u + m_d) - \underbrace{\frac{v^3}{2f_\pi^2}(m_u + m_d)\pi^a\pi^a}_{\frac{1}{2}m_\pi^2\pi^a\pi^a} + \mathcal{O}(\pi^3). \tag{1.2.26}$$

Comparing this with the standard Klein-Gordon Lagrangian for scalar fields $\{\phi^a\}$ each with mass m:

$$\mathcal{L}_{\text{KG}} = \frac{1}{2}(\partial_\mu \phi^a)(\partial^\mu \phi^a) - \frac{1}{2}m^2 \phi^a \phi^a + (\text{interaction terms}), \tag{1.2.27}$$

we see that the pions each have a mass, m_π, such that

$$m_\pi^2 = (m_u + m_d)\frac{v^3}{f_\pi^2}. \tag{1.2.28}$$

Equation (1.2.28) is known as the Gell-Mann–Oakes–Renner (GMOR) relation.

We see that the NGBs have acquired a small mass due to the M term which explicitly breaks chiral symmetry. This is the motivation for constructing the Higgs boson as a composite Goldstone particle of a spontaneously broken approximate global symmetry of a novel strong interaction. The mass of the Higgs would be low by construction rather than due to the presence of extreme fine-tuning.

1.3 *SU(4)/Sp(4)* Symmetry Breaking

In this section, we describe the EFT of $Sp(4)$ as well as supplying the precise definition of the generic group $Sp(2N)$. There are certain constraints that all CHMs must obey and these are laid out in this section. We demonstrate that the same mechanism of chiral symmetry breaking that occurs for QCD (shown in section 1.2.3) also occurs in the symmetry breaking pattern $SU(4) \to Sp(4)$ with two flavours of Dirac fermion in the fundamental representation.

1.3.1 Constraints on Composite Higgs Models

The SM makes very accurate predictions in the Electroweak sector and these should not be upset by any additions we make by way of a composite Higgs. We follow much of the motivation contained in [5, 53, 54] for a simple model of a composite Higgs: the breaking of $SU(4)/Sp(4)$ symmetry as well as showing that the methods of χSB in section 1.2.1 can be used in this context.

In order to define the symplectic groups, we first define the special unitary groups denoted by $SU(N)$. If $SL(N, \mathbb{C})$ is the group of $N \times N$ complex-valued, matrices with determinant 1 (the special linear group) then the group $SU(N)$ is defined as

$$SU(N) = \{U \in SL(N, \mathbb{C}) : U^\dagger U = \mathbb{1}_N\}, \tag{1.3.1}$$

where $\mathbb{1}_N$ is the $N \times N$ identity matrix and $U^\dagger \equiv U^{*T}$ denotes the hermitean conjugate of U. The group $SU(N)$ has dimension $N^2 - 1$ and rank $N - 1$.

The symplectic group, $Sp(2N)$, is defined in terms of the special unitary group of odd rank, $SU(2N)$, as

$$Sp(2N) = \{M \in SU(2N) : M^* = \Omega^\dagger M \Omega\} \tag{1.3.2}$$

where

$$\Omega = \begin{bmatrix} 0 & \mathbb{1}_N \\ -\mathbb{1}_N & 0 \end{bmatrix}. \tag{1.3.3}$$

The group $Sp(2N)$ has dimension $N(2N + 1)$ and rank N.

The notation "$2N$" emphasises the fact that the matrices in the $Sp(2N)$ group must be of even dimension, but it should be noted that the number of charges of the corresponding Yang-Mills theory (often termed "colours") is given by $N_c = 2N$. Since

$\Omega^\dagger = \Omega^{-1}$, we see from the definition that the group, $Sp(2N)$, is pseudo-real; i.e. each representation is equivalent to its complex conjugate but cannot be expressed as a real matrix. (A necessary condition for pseudo-reality is that the matrices are of even dimension [55].) This has consequences for the computation of the glueball spectrum of $Sp(2N)$ gauge theories discussed in section 3.1.

If we write a general element of $Sp(2N)$ as consisting of four $N \times N$ block matrices, we find

$$U = \begin{bmatrix} A & B \\ -B^* & A^* \end{bmatrix} \tag{1.3.4}$$

such that $AA^\dagger + BB^\dagger = \mathbb{1}_N$ and $AB^T = BA^T$ [56]. A derivation of this structure is given in Appendix B.

The skeleton for the composite Higgs is an approximate symmetry, G, undergoing SSB to the group H [5, 9, 13]. The coset space G/H is spanned by the PNGBs by analogy with the pions of chiral symmetry breaking (see section 1.2.1). There are several constraints that must be placed on the new model. The first of those is that the EW symmetry group $SU(2)_L \otimes U(1)_Y$ must be contained in the symmetry group of the new gauge sector, H. This will later undergo the Standard Model EWSB endowing the W and Z bosons with mass.

The new gauge sector must also satisfy the $SU(2)_c$ custodial symmetry of the SM. The masses of the two weak bosons, W and Z, are related by the Weinberg angle, θ_W:

$$M_W = M_Z \cos\theta_W. \tag{1.3.5}$$

If the weak-isospin ($SU(2)_L$) and weak-hypercharge ($U(1)_Y$) couplings are g_W and g', respectively, then

$$\cos\theta_W = \frac{g_W}{\sqrt{g_W^2 + g'^2}}. \tag{1.3.6}$$

Equation (1.3.5) can be written as in [57]:

$$\rho \equiv \frac{M_W^2}{M_Z^2 \cos^2 \theta_W} = 1. \tag{1.3.7}$$

A custodial symmetry is an approximate global symmetry that protects eq. (1.3.7) from higher order corrections [1] and stems from the $SU(2)$ symmetry that remains after the chiral symmetry breaking laid out in eq. (1.2.10) [57]. No deviation from eq. (1.3.7) has been observed and, as such, our new composite Higgs model must respect it.

One motivation for studying symplectic groups arises from their relevance for the PNGB mechanism of electroweak symmetry breaking. In this context, an EFT approach provides a valuable insight. We describe the coset $SU(4)/Sp(4)$ in the same fashion as [5, 13, 53, 54] which uses similar methods to χSB described in section 1.2.1.

1.3.2 *Sp(4)* Effective Field Theory

Since $Sp(4) \subset SU(4)$, we can embed the generators of $Sp(4)$ into those of $SU(4)$. The fifteen generators of $SU(4)$ satisfy the two conditions

$$T^a = (T^a)^\dagger, \quad \mathrm{tr}(T^a) = 0 \qquad a = 1, 2, \ldots, 15. \tag{1.3.8}$$

Eq. (1.3.8) is derived by writing a general element of $SU(N)$ in the form $e^{i\alpha^a T^a}$ and treating the α terms as infinitesimal. Applying the same method to $Sp(2N)$, we find

$$\begin{aligned} e^{-i\alpha^A T^{A*}} &= \Omega^\dagger e^{i\alpha^B T^B} \Omega \\ \implies \mathbb{1} - i\alpha^A T^{A*} &= \Omega^\dagger (\mathbb{1} + i\alpha^B T^B) \Omega \end{aligned}$$

$$
\begin{aligned}
\implies \mathbb{1} - i\alpha^A T^{A*} &= \Omega^\dagger\Omega + i\Omega^\dagger\alpha^B T^B\Omega \\
\implies \mathbb{1} - i\alpha^A T^{A*} &= \mathbb{1} + i\Omega^\dagger\alpha^B T^B\Omega \\
\implies \alpha^A T^{A*} &= -\Omega^\dagger\alpha^A T^A\Omega \\
\implies (T^{A*})^\dagger &= -\Omega^\dagger T^A\Omega \\
\implies \Omega(T^A)^T &= -T^A\Omega \\
\implies T^A\Omega + \Omega(T^A)^T &= 0. \qquad (1.3.9)
\end{aligned}
$$

The ten generators of $Sp(4)$ — as well as obeying eq. (1.3.8) — must also satisfy eq. (1.3.9). All fifteen generators are normalised such that $\mathrm{tr}(T^aT^b) = \frac{1}{2}\delta^{ab}$. An explicit embedding of these generators is stated in Appendix A. Using the notation provided in that appendix,

$$
\begin{aligned}
SU(4) &= \{e^{i\alpha^a T^a} : a = 1, \ldots, 15\}, \qquad (1.3.10) \\
Sp(4) &= \{e^{i\alpha^a T^a} : a = 6, \ldots, 15\}. \qquad (1.3.11)
\end{aligned}
$$

The broken generators describe the coset as

$$
SU(4)/Sp(4) = \{e^{i\alpha^a T^a} : a = 1, \ldots, 5\}, \qquad (1.3.12)
$$

and these are used to parameterise the pions of the $Sp(4)$ group.

The full Lagrangian for $Sp(4)$ Yang-Mills theory with N_f fermions in the fundamental representation is

$$
\mathcal{L} = -\frac{1}{2}\,\mathrm{tr}\, V_{\mu\nu}V^{\mu\nu} + \sum_{f=1}^{N_f} \overline{\psi}_f{}^c(i\not{D} - m_f)\psi_{fc} \qquad (1.3.13)
$$

with summation over charge indices ($c = 1, \ldots, 4$). The field strength tensor is $V_{\mu\nu} \equiv \partial_\mu V_\nu - \partial_\nu V_\mu + ig[V_\mu, V_\nu]$, the covariant derivative is $D_\mu \psi_c = \partial_\mu \psi_c + igV_\mu \psi_c$ and g is the coupling constant.

We write the four-component spinors ψ^{fc} in terms of two-component Weyl spinors q^{fc} as in [5, 13, 54]. We can construct the antisymmetric combination

$$\Sigma_0^{nm} = \sum_{a,b=1}^{4} \Omega_{ab} q^{naT} \widetilde{C} q^{mb} \tag{1.3.14}$$

where Ω is the 4×4 symplectic matrix (the matrix of eq. (1.3.3) with $N = 2$). In this context, the mass matrix can be conveniently written in the form $M = m\Omega$.

In the same fashion as [5, 54], we examine the EFT by introducing the new field Σ as in eq. (1.2.14) but in the form

$$\Sigma = e^{2i\pi(x)/f}\Omega. \tag{1.3.15}$$

The field Σ transforms as

$$\Sigma \longrightarrow U\Sigma U^T \tag{1.3.16}$$

and the lowest order term in the Chiral Lagrangian is

$$\mathcal{L}_0 = \frac{f^2}{4} \operatorname{tr}\{(\partial_\mu \Sigma)(\partial^\mu \Sigma)^\dagger\} \tag{1.3.17}$$

$$\Longrightarrow \mathcal{L}_0 = \operatorname{tr}\{(\partial_\mu \pi)(\partial^\mu \pi)\} + \frac{1}{3f^2} \operatorname{tr}\{[\partial_\mu \pi, \pi]\,[\partial^\mu \pi, \pi]\} + \mathcal{O}(\pi^6) \tag{1.3.18}$$

$$\Longrightarrow \mathcal{L}_0 = \operatorname{tr}\{(\partial_\mu \pi)(\partial^\mu \pi)\} + \frac{2}{3f^2} \operatorname{tr}\{\pi(\partial_\mu \pi)\pi(\partial^\mu \pi) - \pi^2(\partial_\mu \pi)(\partial^\mu \pi)\} + \mathcal{O}(\pi^6). \tag{1.3.19}$$

It is clear from the above that the decay constant for the new pions (i.e. the composite

Higgs) is f in the above parameterisation.

Treating the mass as a spurion field, M, transforming as

$$M \longrightarrow U^* M U^\dagger, \tag{1.3.20}$$

the Lagrangian term is

$$\begin{aligned} \mathcal{L}_{\text{mass}} &= -\frac{v^3}{2}\,\text{tr}\{M\Sigma + M^\dagger\Sigma^\dagger\} && (1.3.21)\\ \implies \mathcal{L}_{\text{mass}} &= 2mv^3 - \frac{mv^3}{f^2}\,\text{tr}\{\pi^2\} + \frac{mv^3}{3f^4}\,\text{tr}\{\pi^4\} + \mathcal{O}(\pi^6), && (1.3.22) \end{aligned}$$

from which we see that the GMOR relation holds in this case:

$$m_\pi^2 = m\frac{v^3}{f^2}. \tag{1.3.23}$$

The EFT treatment shown above demonstrates that the methods of χSB and the generation of small masses emerges from an $SU(4)$ symmetry spontaneously broken to $Sp(4)$. Four of the five PNGBs are interpreted as the familiar Higgs doublet.

The method of χSB captures the low energy behaviour as shown for our $Sp(4)$ model as well as QCD. The methods of lattice field theory will allow us to understand the non-perturbative behaviour of $Sp(2N)$ Yang-Mills theories generally. In addition, lattice calculations enable us to match the parameters of the fundamental theory to the EFT. In the following chapter, we will provide an overview of the lattice methods that have been used in this dissertation.

1.4 Yang-Mills in the Large-N Limit

The large-N limit framework enables us to understand how central observables of the theory depend on N without having to compute them explicitly at all values of N.

The idea of studying Yang-Mills with an infinite number of charges was proposed by 't Hooft in 1973 [58] (coincidentally, the same year as Wilson's paper on LFT [16] was published). QCD is a Yang-Mills theory with gauge group $SU(3)$ and, hence, has three charges (known as colours). 't Hooft showed that Yang-Mills theories with N charges possess an expansion in powers of $\mathcal{O}(1/N)$. The first order corrections for special unitary groups are, in fact, $\mathcal{O}(1/N^2)$. Studying QCD in this limit is not to make the claim that 3 is close to infinity but to say that 1/9 is close to zero and we can obtain results that will be correct to within approximately 10%. A nice exercise involving a large-N limit, given by David Tong in his lecture notes [59], solves the hydrogen atom with $SO(\infty)$ rotational symmetry as opposed to the true $SO(3)$ rotational symmetry. The ground state energy in the large-N limit is approximated as

$$E_{\text{ground}} = \frac{m\alpha^2}{N^2}\left(2 + \mathcal{O}\left(\frac{1}{N}\right)\right). \tag{1.4.1}$$

It is understood that the symplectic, orthogonal and unitary groups all coincide in the limit $N \to \infty$ [14,60,61]. This not only offers a comparison of our numerical data with those already in the literature but allows us to examine the large-N behaviour of all groups by studying just one of them.

In addition, we want to study the behaviour of $Sp(2N)$ gauge theories for different finite values of N. When we have data for three or more values of N, we can extrapolate our observables to large-N by plotting the behaviour as a function of $1/N$ in the case of symplectic groups on the assumption that the first order corrections are

sufficient to extrapolate to $N \to \infty$. As explained in the Introduction, the quenched results provide an initial limit towards which we can evaluate dynamical simulations. In addition, fermions in the fundamental representation have their loops suppressed relative to gauge loops in the large-N limit. Therefore, we expect that dynamical- and quenched-calculations for fundamental fermions will coincide as $N \to \infty$.

Chapter 2

Sp(2N) Gauge Theories on the Lattice

Lattice field theory, in combination with Monte-Carlo calculations, enables us to provide robust results for strongly interacting systems, for which, in contrast with the case of weakly interacting ones, a general framework for analytic calculations is not known. The theory of Quantum Electrodynamics (QED) is an example of a theory that cannot be solved exactly but whose solutions can be approximated via perturbation theory thanks to the fact that the coupling is small. In fact, its coupling constant, α_e, gives a "measurement" as to how insoluble the theory is. It is defined as

$$\alpha_e = \frac{e^2}{4\pi}, \tag{2.0.1}$$

where e is the unit of fundamental electric charge. α_e is a dimensionless parameter whose numerical value is

$$\alpha_e \approx \frac{1}{137} \ll 1. \tag{2.0.2}$$

The smallness of this quantity allows us to treat the theory perturbatively with the familiar expansion in Feynman diagrams. Observables, such as scattering cross-sections and decay widths, can be approximated in this fashion to a high degree of accuracy.

By virtue of asymptotic freedom, QCD is weakly-coupled at short-distances and high-energies. This allows us to recycle most of the perturbative methods used in the case of QED in this limit. Although QCD is more complex than QED, due to the self-interactions of the gauge bosons, the same process can be carried out in principle.

However, at low energies and large distances, the strong coupling constant is

$$\alpha_s = \mathcal{O}(1) \tag{2.0.3}$$

and perturbation theory is no longer applicable. In this regime, Feynman diagrams have very little currency and we require a fully non-perturbative treatment to determine the qualitative and quantitative behaviour. This is the *raison d'être* of Lattice Field Theory. It is the best method we currently have to explore the non-perturbative regime. This chapter provides an introduction to LFT tailored to our investigations of $Sp(2N)$. In section 2.1 we describe pure Yang-Mills theory in the continuum then shift to the Euclidean spacetime lattice in section 2.2. The methodology of extracting observable quantities from the lattice is explained in section 2.3. The Kennedy-Pendleton algorithm for generating random elements of the $SU(2)$ group is described in section 2.4 and the supplementary method of overrelaxation is contained in section 2.5. The generalisation of the Kennedy-Pendleton algorithm to an $Sp(2N)$ matrix is explained in section 2.6. Finally, the method of resymplectisation is described in section 2.7. We remark that this chapter focusses only on simulation methods. Details of the computation of observables will be provided contextually with the numerical results.

Lattice calculations for this thesis have been carried out using the HiRep code.

This is a collaborative work headed by Claudio Pica that has been supplemented with code that incorporates symplectic Yang-Mills.

2.1 Pure Yang-Mills Theory in the continuum

We define a pure Yang-Mills theory with gauge group $\mathcal{G}$, coupling strength g and N_c charges. (In the case of QCD, $N_c = 3$, the three colour charges.) The group is generated by the matrices $\{t^a : a = 1, 2, \ldots, \dim(\mathcal{G})\}$:

$$\exp(i\alpha^a(x)t^a) \in \mathcal{G}, \tag{2.1.1}$$

with summation over the repeated index a and each t^a is a $N_c \times N_c$ matrix.

The commutator of two generators gives rise to the structure constants f^{abc} via

$$[t^a, t^b] \equiv t^a t^b - t^b t^a = i f^{abc} t^c, \tag{2.1.2}$$

where f^{abc} is real and totally antisymmetric. Also, the generators are normalised such that

$$\mathrm{tr}(t^a t^b) = \frac{1}{2}\delta^{ab}, \tag{2.1.3}$$

where δ^{ab} is the Kronecker-Delta.

Fermion fields are denoted by

$$\Psi(x) = \begin{bmatrix} \psi_1(x) \\ \psi_2(x) \\ \vdots \\ \psi_{N_c}(x) \end{bmatrix} \tag{2.1.4}$$

where each $\psi_i(x)$ is a four-component Dirac spinor. Assuming the fermions are in the fundamental representation of the gauge group (as is the case for quarks), the fermions transform under the gauge group as

$$\Psi'(x) = V(x)\Psi(x) \tag{2.1.5}$$

where $V(x)$ is an arbitrary element of $\mathcal{G}$. The gauge fields are denoted by

$$A_\mu(x) = A^a_\mu(x)t^a \tag{2.1.6}$$

and their corresponding transformation under the gauge group is

$$A'_\mu(x) = V(x)A_\mu(x)V^\dagger(x) - i(\partial_\mu V(x))V^\dagger(x). \tag{2.1.7}$$

which is the transformation in the adjoint representation.

The fact that the gauge invariance is local (i.e. different at every spacetime coordinate) means that the ordinary derivative, ∂_μ, is not a gauge invariant operator. Since the fields transform differently at all points in spacetime, the ordinary derivative cannot determine if the fields are changing because of the gauge transformation or because of a genuine gradient. The ordinary derivative determines the net change from these two contributions. For this reason we construct a covariant derivative, D_μ, that removes the effects of the gauge transformation and is, thus, a gauge invariant quantity

$$D_\mu = \partial_\mu - iA_\mu. \tag{2.1.8}$$

Under a gauge transformation

$$D'_\mu = V(x) D_\mu V^\dagger(x) \tag{2.1.9}$$

and, hence,

$$D'_\mu \Psi'(x) = V(x) D_\mu \Psi(x). \tag{2.1.10}$$

From the covariant derivative, we can construct a field-strength tensor for pure Yang-Mills theory by computing its commutator,

$$F_{\mu\nu} = [D_\mu, D_\nu] = \partial_\mu A_\nu - \partial_\nu A_\mu - i[A_\mu, A_\nu]. \tag{2.1.11}$$

(In the abelian case, the commutator of the gauge fields vanishes and we are left with the Faraday tensor of QED.) The non-abelian field strength tensor, $F_{\mu\nu}(x)$, transforms the same way as the covariant derivative:

$$F'_{\mu\nu}(x) = V(x) F_{\mu\nu}(x) V^\dagger(x). \tag{2.1.12}$$

The action for the theory is a functional of the gauge fields, $S[A]$, and must be a gauge-invariant quantity, as per Noether's theorem. A natural candidate for S is

$$S[A] = -\frac{1}{2g^2} \int \mathrm{d}^4x \ \mathrm{tr}(F_{\mu\nu} F^{\mu\nu}) \tag{2.1.13}$$

by analogy with that of QED. The trace term guarantees that the Lagrangian is gauge invariant. Yang-Mills theory, described by eq. (2.1.13), is a non-Abelian generalisation of QED.

We can write $F_{\mu\nu}$ in a similar form to that of eq. (2.1.6).

$$
\begin{aligned}
F_{\mu\nu} &= \partial_\mu A^a_\nu t^a - \partial_\nu A^a_\mu t^a - i[t^a, t^b] A^a_\mu A^b_\nu && (2.1.14)\\
\implies F^a_{\mu\nu} t^a &= \partial_\mu A^a_\nu t^a - \partial_\nu A^a_\mu t^a + f^{abc} t^c A^a_\mu A^b_\nu && (2.1.15)\\
\implies F^a_{\mu\nu} t^a &= (\partial_\mu A^a_\nu - \partial_\nu A^a_\mu + f^{abc} A^b_\mu A^c_\nu) t^a && (2.1.16)\\
\implies F^a_{\mu\nu} &= \partial_\mu A^a_\nu - \partial_\nu A^a_\mu + f^{abc} A^b_\mu A^c_\nu. && (2.1.17)
\end{aligned}
$$

Using eq. (2.1.3), the action becomes

$$
S = -\frac{1}{4g^2} \int \mathrm{d}^4 x \, F^a_{\mu\nu} F^{a\mu\nu}. \tag{2.1.18}
$$

In order to measure observable quantities, we construct the path integral:

$$
Z \equiv \int \mathcal{D}A \, e^{iS[A]}, \tag{2.1.19}
$$

from which we can compute the expectation value of an observable, $\hat{O}$, through

$$
\langle \hat{O} \rangle = \frac{1}{Z} \int \mathcal{D}A \, \hat{O} e^{iS[A]}. \tag{2.1.20}
$$

The functional integral is formally defined as

$$
\mathcal{D}A = \prod_x \prod_{\mu,a} \mathrm{d} A^a_\mu(x) \, . \tag{2.1.21}
$$

2.2 Pure Yang-Mills on the Lattice

The calculation of eq. (2.1.20) is analytically intractable, except in a few special cases, due to the infinite number of integrals. To make the computation of eq. (2.1.20)

amenable to numerical evaluation, we first perform a Wick rotation to Euclidean space:

$$x_0 \longrightarrow -ix_4, \tag{2.2.1}$$

$$\partial_0 \longrightarrow i\partial_4. \tag{2.2.2}$$

Under such a transformation, the Minkowski spacetime metric becomes the 4×4 identity matrix:

$$\eta_{\mu\nu} \longrightarrow \delta_{\mu\nu} = \mathbb{1}_4 \tag{2.2.3}$$

and there is no longer any distinction between upper- and lower-Lorentz indices. In addition, the action becomes

$$S_E[A] = \frac{1}{4g^2}\int \mathrm{d}^4x_E\, F^a_{E\mu\nu}F^a_{E\mu\nu}, \tag{2.2.4}$$

where the subscript $_E$ denotes a quantity in Euclidean spacetime, and the partition function, eq. (2.1.19), becomes

$$Z_E = \int \mathcal{D}A\, e^{-S_E[A]}. \tag{2.2.5}$$

The partition function is now exponentially suppressed at large actions allowing for rapid convergence in its computation.

At this point, we shift to a four-dimensional, discrete spacetime lattice denoted by Λ^4. The lattice quantities are defined in table 1. Hereafter, all quantities are measured in Euclidean spacetime unless stated otherwise. (We drop the subscript $_E$.) A two-dimensional slice of a Euclidean lattice is shown in fig. 2.1. Each lattice link,

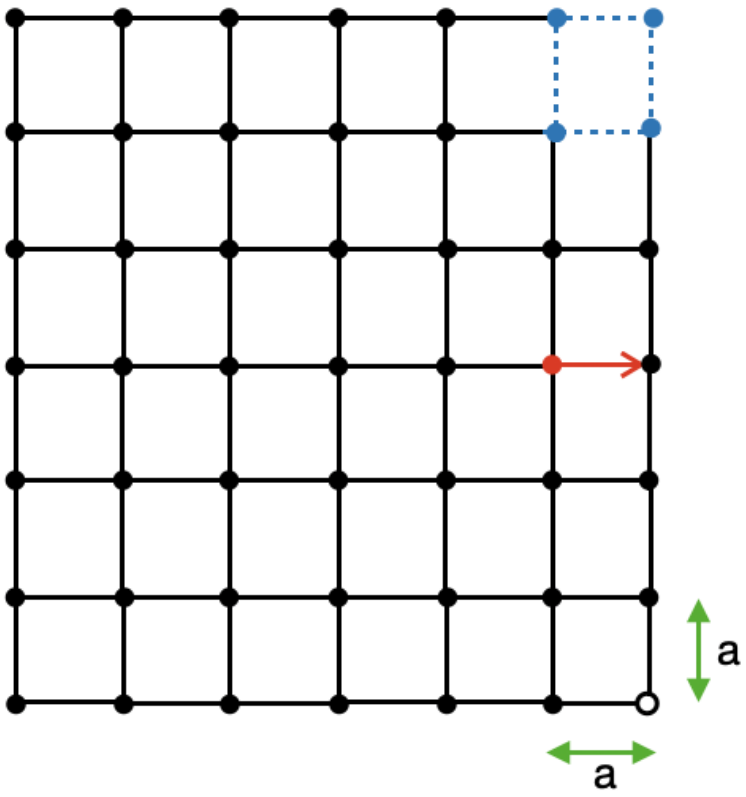

Figure 2.1: A two-dimensional slice of a four-dimensional Euclidean lattice. The blue-dotted lines in the top-right form a plaquette; the red-arrowed line is a lattice link; the hollow circle in the bottom-right is a lattice site. The double-edged green arrows are the lattice spacing denoted by a.

$U_\mu(x)$, is an element of the gauge group, $\mathcal{G}$:

$$U_\mu(x) = \exp(iagA_\mu(x)) \tag{2.2.6}$$

where a is the lattice spacing. Due to the finite volume of the lattice and the discreteness of spacetime, the infinite dimensional integral in eq. (2.1.21) becomes

$$\mathcal{D}U = \prod_{x\in\Lambda^4}\prod_{\mu=1}^{4} \mathrm{d}U_\mu(x) \tag{2.2.7}$$

whose dimension is finite, though it may be very large.

The simplest discretised version of eq. (2.2.4) is the Wilson Action

$$S_W[U] = \beta \sum_{x\in\Lambda^4}\sum_{\mu<\nu}\left(1 - \frac{1}{N_c}\Re\,\mathrm{tr}\,U_{\mu\nu}(x)\right). \tag{2.2.8}$$

The variables β and $U_{\mu\nu}(x)$ are the inverse coupling and plaquette, respectively, and are defined in table 1. Expanding eq. (2.2.8) to leading order in a and taking the limit $a \to 0$ reproduces the continuum action in Euclidean space: eq. (2.2.4).

Thus, we have recast the computation of the partition function as

$$Z = \int \prod_{x\in\Lambda^4}\prod_{\mu=1}^{4} \mathrm{d}U_\mu(x)\, e^{-S_W[U]}. \tag{2.2.9}$$

Such a computation can be carried out with Monte-Carlo methods. We can generate a lattice configuration $\{U_\mu(x) : x \in \Lambda^4,\ \mu = 1,2,3,4\}$ with probability $e^{-S_W[U]}$. If we construct N_{cfg} configurations, computing the observable O from each, we can approximate

$\langle O \rangle$ via

$$\langle O \rangle = \frac{1}{N_{\text{cfg}}} \sum_{i=1}^{N_{\text{cfg}}} O_i + \mathcal{O}\left(\frac{1}{\sqrt{N_{\text{cfg}}}}\right) \tag{2.2.10}$$

where O_i is the measurement of O from the i^{th} configuration. The corrections to the true average are of the order $1/\sqrt{N_{\text{cfg}}}$ due to the central limit theorem. We have, thus, reduced the measurement of observable quantities in Yang-Mills theory to a Monte-Carlo calculation.

The generation of configurations according to a probability distribution is known as "Importance Sampling". We could, in principle, generate lattice configurations entirely uniformly and then weight the measurement of each observable according to the total action of the lattice. This would be highly inefficient due to the enormous number of lattice configurations available to us and the minute contribution to $\langle O \rangle$ that most of them make. A better plan is to generate the configurations with a built-in probability and then average our measurements with equal weight since we have already accounted for the factor $e^{-S_W[U]}$.

2.3 Monte-Carlo Methods for Lattice Yang-Mills

The partition function in eq. (2.2.5) shows that the configurations with the smallest action, $S[U]$, are the most probable as we would anticipate from the principle of least action. A new lattice configuration is generated by updating each individual link on the lattice; this is defined as a lattice "sweep".

When we update a link, which we denote by U, we consider its "staples". These are the six combinations of three links that can combine with the original link to make a plaquette; four of these are shown visually in fig. 2.2. Because the action is local, when updating a single link, we need only consider the staples of the link as opposed

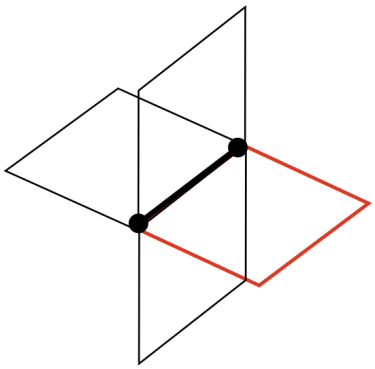

Figure 2.2: A diagram showing a link and four of its six staples. The link is shown bold and and the (three-link) staples are shown as thin lines with a single staple highlighted in red. Since the lattice is four-dimensional, there are two more staples lying in the fourth dimension.

to the whole lattice.

The method for updating a single lattice link depends on the gauge group, $\mathcal{G}$, but this can generally be achieved by updating individual $SU(2)$ subgroups. The algorithm devised by Kennedy and Pendleton is an efficient method for the update of a single $SU(2)$ matrix and is described in section 2.4. In order to update the link fully, we must determine how the $SU(2)$ subgroups are embedded in the group $\mathcal{G}$.

The Cabbibo-Marinari method for updating $SU(N)$ matrices works by updating $SU(2)$ subgroups [62]. By the definition in eq. (1.3.2), we see that $Sp(2N)$ is a subgroup of $SU(2N)$ and we can use the same approach for updating symplectic matrices.

The Kennedy-Pendleton algorithm belongs to a class that can go from any configuration to any other configuration in a finite number of steps. This is known as "ergodicity". Although this means that the entirety of configuration space is available to our simulation, it may be the case that the system evolves through configuration-space very slowly and we must apply a great many update steps to obtain a representative sample and, thus, acquire reliable measurements. If we move through configuration

space too slowly, our lattice configurations will become more and more correlated (each one has a strong dependence on its predecessors in the Markov chain) and we cannot treat consecutive configurations as being independent. We need a way to make our algorithm more efficient and explore configuration-space more quickly.

One way to improve our heat bath algorithm is to supplement it with non-ergodic update steps known as "overrelaxations". By construction, these do not change the action of the lattice and are, thus, always accepted as update steps. They exploit symmetry properties of the action to move the lattice rapidly through configuration space.

The results obtained herein define an update as one heatbath (HB) and four overrelaxation (OR) steps on each link.

2.4 Heatbath algorithm for *SU(2)* matrices

In this section we describe the heatbath algorithm used to update a single $SU(2)$ matrix [63] which we then generalise to an $Sp(2N)$ matrix. The crucial feature for the heatbath algorithm is that the sum of any two $SU(2)$ matrices is equal to a scalar multiple of another $SU(2)$ matrix; the constant of proportionality is the square root of the determinant.

An $SU(2)$ matrix can be written as a linear combination of the three Pauli matrices and the 2×2 identity matrix:

$$U = a_0 \mathbb{1} + i\underline{a} \cdot \underline{\sigma} \tag{2.4.1}$$

where the four a variables are real and obey $a_0^2 + a_1^2 + a_2^2 + a_3^2 = 1$.[1] This is equivalent

[1] This also demonstrates that $SU(2)$ is topologically equivalent to the three-sphere.

to imposing $\det(U) = 1$. The Pauli matrices are

$$\sigma_1 = \begin{bmatrix} 0 & 1 \\ 1 & 0 \end{bmatrix}, \quad \sigma_2 = \begin{bmatrix} 0 & -i \\ i & 0 \end{bmatrix}, \quad \sigma_3 = \begin{bmatrix} 1 & 0 \\ 0 & -1 \end{bmatrix}. \tag{2.4.2}$$

Therefore

$$U = \begin{bmatrix} a_0 + ia_3 & a_2 + ia_1 \\ -a_2 + ia_1 & a_0 - ia_3 \end{bmatrix}. \tag{2.4.3}$$

The hermitean conjugate of U can be easily computed as

$$U^\dagger = a_0 \mathbb{1} - i\underline{a} \cdot \underline{\sigma}. \tag{2.4.4}$$

The three matrices $i\sigma_k$ for $k = 1, 2$ and 3 satisfy the definition of quaternions. Note that, in this representation, $\mathrm{tr}(U) = 2a_0$. The probability distribution used to update a generalised $SU(N)$ matrix U is given by

$$\mathrm{d}P(U) = \mathrm{d}U \exp\left(\frac{\beta}{N} \Re \,\mathrm{tr}[U\ \Sigma]\right) \tag{2.4.5}$$

where Σ is the sum of the link staples, defined in eq. (0.0.4), and $\mathrm{d}U$ is the Haar measure of the group. The sum of all staples, Σ, is proportional to an $SU(2)$ matrix, V:

$$\Sigma = sV \tag{2.4.6}$$

$$s = \sqrt{\det(\Sigma)}. \tag{2.4.7}$$

Hence,

$$\mathrm{d}P(U) = \mathrm{d}U \exp\left(\frac{1}{2} s\beta \Re \,\mathrm{tr}[U\ V]\right). \tag{2.4.8}$$

There is the possibility that Σ is, in fact, the zero-matrix. If this is the case, the updated

link is constructed by choosing four random numbers $\{r_i : i = 1, ..., 4\}$, normalised such that $\sum_{i=1}^{4} r_i^2 = 1$. From this, the new matrix is constructed via

$$U = r_0 \mathbb{1} + i\underline{r} \cdot \underline{\sigma}. \tag{2.4.9}$$

If $\Sigma \neq 0$, we proceed as below.

Define the matrix $X = UV$. The Haar measure is unchanged by the multiplication of a group element, so

$$\mathrm{d}P(X) = \mathrm{d}X \, \exp\left(\frac{1}{2} s\beta \Re \, \mathrm{tr}[X]\right). \tag{2.4.10}$$

Thus, the candidate link

$$U' = XV^\dagger = \frac{1}{s} X\Sigma^\dagger \tag{2.4.11}$$

and

$$X = x_0 \mathbb{1} + i\underline{x} \cdot \underline{\sigma}. \tag{2.4.12}$$

The Haar measure is

$$\begin{aligned}
\mathrm{d}X &= \frac{1}{\pi^2} \mathrm{d}^4x \, \delta(x_0^2 + |\underline{x}|^2 - 1) && (2.4.13)\\
\implies \mathrm{d}X &= \frac{1}{\pi^2} \mathrm{d}^4x \, \frac{\theta(1 - x_0^2)}{2\sqrt{1 - x_0^2}} \\
&\quad \times \left(\delta\left(|\underline{x}| + \sqrt{1 - x_0^2}\right) + \delta\left(|\underline{x}| - \sqrt{1 - x_0^2}\right)\right) && (2.4.14)\\
\implies \mathrm{d}X &= \frac{1}{\pi^2} \mathrm{d}^4x \, \frac{\theta(1 - x_0^2)}{2\sqrt{1 - x_0^2}} \delta\left(|\underline{x}| - \sqrt{1 - x_0^2}\right) && (2.4.15)\\
\implies \mathrm{d}X &= \frac{1}{\pi^2} |\underline{x}|^2 \frac{\theta(1 - x_0^2)}{2\sqrt{1 - x_0^2}} \delta\left(|\underline{x}| - \sqrt{1 - x_0^2}\right) \mathrm{d}x_0 \, \mathrm{d}|\underline{x}| \, \mathrm{d}\phi \, \mathrm{d}\cos\vartheta && (2.4.16)
\end{aligned}$$

$$\implies \mathrm{d}X = \frac{1}{2\pi^2}(1-x_0^2)\frac{\theta(1-x_0^2)}{\sqrt{1-x_0^2}}\,\mathrm{d}x_0\;\mathrm{d}|\underline{x}|\;\mathrm{d}\phi\;\mathrm{d}\cos\vartheta \tag{2.4.17}$$

$$\implies \mathrm{d}X = \frac{1}{2\pi^2}\,\mathrm{d}x_0\;\mathrm{d}\phi\;\mathrm{d}\cos\vartheta\,\sqrt{1-x_0^2}\;\theta(1-x_0^2). \tag{2.4.18}$$

Thus

$$\mathrm{d}P(X) = \frac{1}{2\pi^2}\,\mathrm{d}x_0\;\mathrm{d}\phi\;\mathrm{d}\cos\vartheta\,\sqrt{1-x_0^2}\;\theta(1-x_0^2)e^{s\beta x_0} \tag{2.4.19}$$

with $x_0 \in [-1,1]$, $\cos\vartheta \in [-1,1]$ and $\phi \in [0,2\pi)$.

The computation of x_0 must follow the distribution

$$\sqrt{1-x_0^2}e^{s\beta x_0}. \tag{2.4.20}$$

At this point, we introduce the method of Kennedy and Pendleton [63] (first described in [64]) by introducing a new variable λ:

$$x_0 = 1-2\lambda^2 \tag{2.4.21}$$

$$\implies \mathrm{d}x_0\,\sqrt{1-x_0^2}e^{s\beta x_0} = -4\lambda\,\mathrm{d}\lambda\,\sqrt{4\lambda^2-4\lambda^4}e^{s\beta(1-2\lambda^2)} \tag{2.4.22}$$

$$\implies \mathrm{d}x_0\,\sqrt{1-x_0^2}e^{s\beta x_0} \propto \lambda^2\sqrt{1-\lambda^2}e^{-2s\beta\lambda^2}\,\mathrm{d}\lambda\,. \tag{2.4.23}$$

In addition, the interval $x_0 \in [-1,1]$ is equivalent to $\lambda \in [0,1]$. Therefore, we have to generate λ according to the modified Gaussian

$$\lambda^2\sqrt{1-\lambda^2}e^{-2s\beta\lambda^2}. \tag{2.4.24}$$

The method of [63] is to generate three random numbers (r_1, r_2 and r_3) each uniformly

distributed in the interval $(0, 1]$ then obtain λ via

$$\lambda^2 = -\frac{1}{2s\beta}(\ln(r_1) + \cos^2(2\pi r_2)\ln(r_3)). \tag{2.4.25}$$

The factor of $\sqrt{1-\lambda^2}$ is accounted for by generating a new random number, r, uniformly distributed in the same interval $(0, 1]$ and accepting the value in eq. (2.4.25) if and only if

$$r^2 \leqslant 1 - \lambda^2. \tag{2.4.26}$$

In computing a value for λ^2 we can compute x_0 using eq. (2.4.21).

The Dirac delta in eq. (2.4.13) means that once we have x_0 we get $|\underline{x}| = \sqrt{1-x_0^2}$ for free. The remaining variables are ϕ and $\cos\vartheta$; these can be made by generating a new triplet of random numbers t_1, t_2 and t_3 each uniformly distributed in the interval $[-1, 1)$. If these satisfy $t_1^2 + t_2^2 + t_3^2 \leqslant 1$, the three numbers are accepted and normalised to the length of $|\underline{x}|$:

$$x_i = \frac{t_i\sqrt{1-x_0^2}}{\sqrt{t_1^2+t_2^2+t_3^2}} \tag{2.4.27}$$

These give us the four numbers $(x_0, \underline{x})$ from which we can construct the $SU(2)$ matrix, X. The new link in place of U is $U' = XV^\dagger$. There is no need to carry out an acceptance test for the new link.

To summarise the process for constructing an $SU(2)$ matrix from an initial link U and distributed according to eq. (2.4.5):

1. Compute Σ, the sum of the surrounding staples of U.

2. Compute $s = \sqrt{\det(\Sigma)}$. If $s = 0$, generate four random numbers uniformly distributed in the interval $[-1, 1)$, normalise to 1 and this is the updated matrix.

If $s \neq 0$, then compute the $SU(2)$ matrix $V = \frac{1}{s}\Sigma$.

3. Generate three random numbers r_1, r_2 and r_3 each uniformly distributed in the interval $(0, 1]$ and compute the variable $\lambda^2 = -\frac{1}{2s\beta}(\ln(r_1) + \cos^2(2\pi r_2)\ln(r_3))$.

4. Generate a new random number r in the uniform interval $[0, 1)$.

5. Accept the above value for λ^2 if and only if $r^2 \leqslant 1 - \lambda^2$. If this condition is not met, repeat items 3 to 5 until it is.

6. Compute the variables $x_0 = 1 - 2\lambda^2$ and $|\underline{x}| = \sqrt{1 - x_0^2}$.

7. Generate three random numbers t_1, t_2 and t_3 distributed in the uniform interval $[-1, 1)$. Accept them when they satisfy $t_1^2 + t_2^2 + t_3^2 \leqslant 1$.

8. When the three t-variables have been generated, normalise each of them as follows:

$$x_i = \frac{t_i\sqrt{1 - x_0^2}}{\sqrt{t_1^2 + t_2^2 + t_3^2}} \quad \text{for } i = 1, 2, 3. \tag{2.4.28}$$

9. The variables above give the matrix X

$$X = \begin{bmatrix} x_0 + ix_3 & x_2 + ix_1 \\ -x_2 + ix_1 & x_0 - ix_3 \end{bmatrix} \tag{2.4.29}$$

and the updated link is $U' = XV^\dagger$.

The above procedure can be generalised to construct a matrix in the $Sp(2N)$ group.

2.5 Overrelaxation

Section 2.4 describes the heatbath step for $SU(2)$ matrices. As stated earlier, these can be supplemented with one or more overrelaxation steps. As in [64], define the $SU(2)$ matrix V as in eqs. (2.4.6) and (2.4.7). The matrix U after an overrelaxation step is given by

$$U' = V^\dagger U^\dagger V^\dagger. \tag{2.5.1}$$

Examining the exponent of eq. (2.4.8), we see that the overrelaxation update does not change the action [64]:

$$\begin{aligned}
\Re\,\mathrm{tr}[U'V] &= \Re\,\mathrm{tr}[V^\dagger U^\dagger V^\dagger V] && (2.5.2)\\
\Longrightarrow \Re\,\mathrm{tr}[U'V] &= \Re\,\mathrm{tr}[V^\dagger U^\dagger] && (2.5.3)\\
\Longrightarrow \Re\,\mathrm{tr}[U'V] &= \Re\,\mathrm{tr}[(UV)^\dagger] && (2.5.4)\\
\Longrightarrow \Re\,\mathrm{tr}[U'V] &= \Re\,\mathrm{tr}[UV]. && (2.5.5)
\end{aligned}$$

So the overrelaxation step changes the lattice link, U, without changing the action, S, allowing for more rapid movement through phase-space.

2.6 Generating *Sp(2N)* matrices

If the group $Sp(2N)$ is generated by the matrices

$$\{T^A : A = 1, 2, ..., N(2N+1)\} \tag{2.6.1}$$

then an arbitrary element of M of $Sp(2N)$ can be written in the form

$$M = e^{i\alpha^A T^A}. \tag{2.6.2}$$

where the $\{\alpha^A\}$ are real constants. Since $Sp(2N)$ is a subgroup of $SU(2N)$, the former generators must be hermitean and traceless:

$$(T^A)^\dagger = T^A \tag{2.6.3}$$

$$\mathrm{tr}(T^A) = 0. \tag{2.6.4}$$

In order to be an element of $Sp(2N)$, the matrix M must also satisfy the condition in section 1.3.2. The method described below is the one used in [5, 13, 14].

The method of updating $SU(N)$ matrices starts with the Cartan subalgebra: the subset of $SU(N)$ generators that are mutually commuting. The Cartan generators are denoted by (i, j) which is the matrix with 1 on the i^{th} diagonal, -1 on the j^{th} diagonal and 0's everywhere else. The indices i and j are in the range $1 \leqslant i < j \leqslant N$, hence there are $\frac{1}{2}N(N-1)$ such matrices. An example for $SU(2)$ is familiar as the algebra of spin-$\frac{1}{2}$. The only Cartan generator is

$$(1,2) = \begin{bmatrix} 1 & 0 \\ 0 & -1 \end{bmatrix} = \sigma_3 \tag{2.6.5}$$

with the corresponding raising and lowering operators

$$\sigma_\pm = \sigma_1 \pm i\sigma_2 : \tag{2.6.6}$$

$$\sigma_+ = \begin{bmatrix} 0 & 1 \\ 0 & 0 \end{bmatrix}, \quad \sigma_- = \begin{bmatrix} 0 & 0 \\ 1 & 0 \end{bmatrix}. \tag{2.6.7}$$

For $SU(3)$, the Cartan generators are

$$(1,2) = \begin{bmatrix} 1 & 0 & 0 \\ 0 & -1 & 0 \\ 0 & 0 & 0 \end{bmatrix}, \quad (2,3) = \begin{bmatrix} 0 & 0 & 0 \\ 0 & 1 & 0 \\ 0 & 0 & -1 \end{bmatrix} \text{ and } (1,3) = \begin{bmatrix} 1 & 0 & 0 \\ 0 & 0 & 0 \\ 0 & 0 & -1 \end{bmatrix}. \tag{2.6.8}$$

Each matrix in 2.6.8 is the Pauli matrix σ_3 embedded in a 3×3 matrix and the corresponding raising and lowering operators are $\sigma_\pm$ embedded in the same section of the 3×3 matrix.

For $SU(N)$ in general, we can write the fundamental representation, $[N]_{SU}$, as a direct sum

$$[N]_{SU} = \{2\} \oplus \mathbb{1}_{N-2} \tag{2.6.9}$$

where $\{2\}$ is the fundamental representation of $SU(2)$. When considering $Sp(2N)$, we restrict our attention to such embeddings that obey the block structure in eq. (1.3.4). We use N^2 such subgroups; this redundancy is used to decrease correlation between successive updates. There are three unitarily distinct classes of $SU(2)$ embeddings for general $Sp(2N)$ (i.e. embeddings that are not related by a unitary transformation) and we give concrete examples for $Sp(6)$.

The embedding $(1,2)$ is unitarily equivalent to all those for which ($i < N$,

$j < N$):

$$\begin{bmatrix} 1 & 0 & 0 & 0 & 0 & 0 \\ 0 & a & b & 0 & 0 & 0 \\ 0 & -b^* & a^* & 0 & 0 & 0 \\ 0 & 0 & 0 & 1 & 0 & 0 \\ 0 & 0 & 0 & 0 & a^* & b^* \\ 0 & 0 & 0 & 0 & -b & a \end{bmatrix}, \begin{bmatrix} a & 0 & b & 0 & 0 & 0 \\ 0 & 1 & 0 & 0 & 0 & 0 \\ -b^* & 0 & a^* & 0 & 0 & 0 \\ 0 & 0 & 0 & a^* & 0 & b^* \\ 0 & 0 & 0 & 0 & 1 & 0 \\ 0 & 0 & 0 & -b & 0 & a \end{bmatrix} \text{ and } \begin{bmatrix} a & b & 0 & 0 & 0 & 0 \\ -b^* & a^* & 0 & 0 & 0 & 0 \\ 0 & 0 & 1 & 0 & 0 & 0 \\ 0 & 0 & 0 & a^* & b^* & 0 \\ 0 & 0 & 0 & -b & a & 0 \\ 0 & 0 & 0 & 0 & 0 & 1 \end{bmatrix} \tag{2.6.10}$$

where a and b are complex numbers such that $|a|^2+|b|^2= 1$ and $a^*b = b^*a$. There are $N(N-1)/2$ such embeddings for $Sp(2N)$ all of which are listed in (2.6.10) for $Sp(6)$.

The second class of embeddings is similar to those above except that one of the $SU(2)$ blocks is embedded in the other:

$$\begin{bmatrix} 1 & 0 & 0 & 0 & 0 & 0 \\ 0 & a & 0 & 0 & 0 & b \\ 0 & 0 & -a^* & 0 & -b^* & 0 \\ 0 & 0 & 0 & 1 & 0 & 0 \\ 0 & 0 & -b^* & 0 & a^* & 0 \\ 0 & b & 0 & 0 & 0 & -a \end{bmatrix}, \begin{bmatrix} a & 0 & 0 & 0 & 0 & b \\ 0 & 1 & 0 & 0 & 0 & 0 \\ 0 & 0 & -a^* & -b^* & 0 & 0 \\ 0 & 0 & -b^* & a^* & 0 & 0 \\ 0 & 0 & 0 & 0 & 1 & 0 \\ b & 0 & 0 & 0 & 0 & -a \end{bmatrix} \text{ and } \begin{bmatrix} a & 0 & 0 & 0 & b & 0 \\ 0 & -a^* & 0 & -b^* & 0 & 0 \\ 0 & 0 & 1 & 0 & 0 & 0 \\ 0 & -b^* & 0 & a^* & 0 & 0 \\ b & 0 & 0 & 0 & -a & 0 \\ 0 & 0 & 0 & 0 & 0 & 1 \end{bmatrix} \tag{2.6.11}$$

where a and b are complex numbers such that $|a|^2+|b|^2= 1$ and $a^*b = b^*a$. There are $N(N-1)/2$ such embeddings for $Sp(2N)$ all of which are listed in (2.6.11) for $Sp(6)$.

The embedding $(1, 1+N)$ is unitarily equivalent to the embeddings $(i, i+N)$:

$$\begin{bmatrix} a & 0 & 0 & b & 0 & 0 \\ 0 & 1 & 0 & 0 & 0 & 0 \\ 0 & 0 & 1 & 0 & 0 & 0 \\ -b^* & 0 & 0 & a^* & 0 & 0 \\ 0 & 0 & 0 & 0 & 1 & 0 \\ 0 & 0 & 0 & 0 & 0 & 1 \end{bmatrix}, \quad \begin{bmatrix} 1 & 0 & 0 & 0 & 0 & 0 \\ 0 & a & 0 & 0 & b & 0 \\ 0 & 0 & 1 & 0 & 0 & 0 \\ 0 & 0 & 0 & 1 & 0 & 0 \\ 0 & -b^* & 0 & 0 & a^* & 0 \\ 0 & 0 & 0 & 0 & 0 & 1 \end{bmatrix} \text{ and } \begin{bmatrix} 1 & 0 & 0 & 0 & 0 & 0 \\ 0 & 1 & 0 & 0 & 0 & 0 \\ 0 & 0 & a & 0 & 0 & b \\ 0 & 0 & 0 & 1 & 0 & 0 \\ 0 & 0 & 0 & 0 & 1 & 0 \\ 0 & 0 & -b^* & 0 & 0 & a^* \end{bmatrix} \tag{2.6.12}$$

where a and b are complex numbers such that $|a|^2+|b|^2= 1$ and $a^*b = b^*a$. There are N such embeddings for $Sp(2N)$ all of which are listed in (2.6.12) for $Sp(6)$. The number of generators, as stated before, is $N(N-1)/2+N(N-1)/2+N = N^2$. Note that each matrix in eqs. (2.6.10) to (2.6.12) satisfies the block structure of eq. (1.3.4).

The total number of $SU(2)$ generators is bigger than the dimension of the group. As a consequence, the group can be covered in a non-unique way by the product of matrices belonging to the $SU(2)$ subgroups identified above. (This redundancy can serve to decrease the correlation between successive elements in our Markov chain of pure gauge configurations.) We can thus apply the Heatbath algorithm for $SU(2)$ matrices to each of the aforementioned subgroups along with four overrelaxation steps to construct a Markov chain of lattice configurations.

2.7 Resymplectisation

After each update step, floating point errors will accumulate and result in a deviation of each updated matrix from the group manifold. After each lattice sweep, we project each lattice link back onto the group manifold using a resymplectisation algorithm (the

equivalent for $SU(N)$ simulations being reunitarisation algorithms).

Once again, the block structure can be used to project each matrix back to the group manifold:

$$U = \begin{bmatrix} A & B \\ -B^* & A^* \end{bmatrix}. \tag{2.7.1}$$

Note that

$$\begin{bmatrix} B \\ A^* \end{bmatrix} = -\begin{bmatrix} 0 & \mathbb{1}_N \\ -\mathbb{1}_N & 0 \end{bmatrix} \begin{bmatrix} A \\ -B^* \end{bmatrix}^* \tag{2.7.2}$$

$$\begin{bmatrix} B \\ A^* \end{bmatrix} = -\Omega \begin{bmatrix} A \\ -B^* \end{bmatrix}^*. \tag{2.7.3}$$

Hence, from each of the N columns on the left of the updated matrix U, we can determine each of the N columns on the right.

$$U_{i,j+N} = -\sum_{k=1}^{2N} \Omega_{ik} U^*_{kj} \quad \text{for } 1 \leqslant i \leqslant 2N \text{ and } 1 \leqslant j \leqslant N. \tag{2.7.4}$$

As well as the above, the matrix, U, must satisfy unitarity which corresponds to each of its columns (and rows) being mutually orthonormal. This process can be carried out using the modified Gram-Schmidt process. The full process for resymplectisation is:

- Normalise column 1 to unit length.
- Compute column $(1 + N)$ using eq. (2.7.4).
- Compute column 2 by orthonormalising with respect to columns 1 and $1 + N$.
- Compute column $(2 + N)$ using eq. (2.7.4).

- Repeat the above until all columns have been determined.

Chapter 3

Glueballs and Strings

A main motivation for the work carried out in this thesis was the exploration of $Sp(2N)$ gauge theories in the limit of large-N. More precisely, if the theory has coupling strength g, we examine the behaviour as $N \to \infty$ with the quantity $\lambda \equiv 2Ng^2$ held fixed. This is known as the 't Hooft-limit or planar-limit. Yang-Mills theories based on orthogonal, symplectic or unitary groups possess an expansion in powers of $1/N$ and the Feynman diagrams can be ordered according to their topology with the planar diagrams dominating in the large-N limit [58].

In this chapter, our main focus will be the determination of glueball masses in $Sp(2N)$ gauge theories and their extrapolation to $N \to \infty$. Glueballs are massive particles composed solely of gauge bosons. Their existence is a consequence of confinement and self-interaction of gauge bosons in non-Abelian gauge theories. Glueball masses can be computed in lattice simulations, and their determination provides a non-perturbative characterisation of gauge field dynamics. Besides glueballs, another signature of confinement is the existence of gluon flux tubes whose dynamics are described by an effective string theory. The main parameter of the effective dynamics,

the string tension σ, can be extracted from the interaction potential between a static quark and its antiquark, which can be parameterised as:

$$V(r) = -\frac{\alpha}{r} + \sigma r + C, \tag{3.0.1}$$

where α, and C are two constants the discussion of which is beyond our scope. The term σ can be measured in lattice simulations.

This chapter provides a description of the methods used in our calculations to extract glueball masses and the string tension at fixed N and to extrapolate them to $N \to \infty$, together with our numerical results and a discussion of what we have learned from this investigation. In section 3.1 we briefly describe the implementation of $Sp(2N)$ Yang-Mills on the lattice. A reminder of notation as well as the action governing the dynamics is given. In section 3.2 the variational method used to compute glueball masses is outlined. Section 3.3 describes blocking and improved smearing techniques used to improve the signal of the glueball and, thus, obtain more accurate measurements. The construction of glueball operators is outlined in section 3.4 and the computation of the string tension in section 3.5. The method of extrapolation to continuum, thermodynamic and large-N limits is described in section 3.6. The hypothesis of Casimir Scaling is described in section 3.7. The results and final discussion are in sections 3.8 and 3.9, respectively.

3.1 Our Lattice Model

In the continuum, glueballs are labelled in the form J^{PC} where J is its (integer) spin, P is its parity ($+$ or $-$) and C is its charge conjugation (again, $+$ or $-$). Due to the pseudo-reality of the symplectic groups (demonstrated explicitly in eq. (1.3.2)), charge

conjugation is always positive and this quantum number is left implicit hereafter. In addition, we label the n-th excited state of a particular channel by the addition of n asterisks (*) after the parity sign. For example, the ground state of the spin-0 glueball with positive parity would be denoted by 0^+ and 0^{+**} denotes the corresponding second excited state.

When we shift from continuous Minkowski spacetime to discrete Euclidean spacetime, the continuous $SO(3)$ symmetry of the former is broken to the discrete O_h symmetry of the cube. For this reason, we label the lattice glueballs differently from the continuum ones. The five irreducible representations of the cubic group are denoted conventionally by A_1, A_2, E, T_1 and T_2. We label the lattice glueballs in the form R^P where R is the representation of O_h. In other words, we replace the spin value, J, with the representation label, R; the notations for parity and excitations are unchanged.

In addition to the glueball spectrum, we can also determine the string tension, σ. If two static, infinitely-massive fermions carrying opposite charges of the theory – e.g. a quark-antiquark pair in the case of QCD – are separated by a distance r, then the potential between the two is given by eq. (3.0.1). At large distances, the linear term dominates and the two quarks require infinite energy to be separated from each other. The motivation for measuring σ is that it allows a test of confinement as well as setting the scale for the glueball spectrum mentioned above. Dimensional analysis shows that σ has mass dimension 2 allowing $\sqrt{\sigma}$ to be interpreted as a mass scale.

The mass spectrum of the glueballs is determined by the variational method described in sections 3.2 to 3.4, inclusive. The string tension is determined in a similar way in section 3.5. Throughout the aforementioned sections, we describe a Yang-Mills theory with gauge group $Sp(2N)$ on a four-dimensional, hypercubic lattice with periodic boundary conditions in all directions. For concreteness, we also refer to fermions as "quarks" and gauge bosons as "gluons" to allow an analogy with QCD.

Throughout these calculations, we use the standard Wilson Action:

$$S = \beta \sum_{x \in \Lambda^4} \sum_{\mu < \nu} \left(1 - \frac{1}{N_c} \Re \operatorname{tr} U_{\mu\nu}(x) \right) \tag{3.1.1}$$

where

$$\beta = \frac{2N_c}{g^2} \tag{3.1.2}$$

and g is the bare coupling. N_c is the number of charges of the theory ($N_c = 2N$ for $Sp(2N)$), $\Re(x)$ denotes the real part of quantity x, tr is the trace operator and $U_{\mu\nu}(x)$ is the plaquette in the $\mu\nu$-plane originating at lattice site x:

$$U_{\mu\nu}(x) = U_\mu(x) U_\nu(x + \hat{\mu}) U_\mu^\dagger(x + \hat{\nu}) U_\nu^\dagger(x). \tag{3.1.3}$$

3.2 Determining the Glueball Spectrum

In the continuum, we would extract the glueball masses by finding the location of the singular points in the propagator. On the lattice we adopt a different approach called the variational method. The variational method for determining the glueball spectrum involves fitting an exponential decay to a correlation function of creation and annihilation operators in coordinate space. The operators are path-ordered, gauge invariant products of link variables that transform in the relevant representation of the cubic group.

The paths comprising the operators must be closed in order to ensure gauge invariance. A single link transforms under the gauge group as

$$U_\mu(x) \longrightarrow V(x) U_\mu(x) V(x + \hat{\mu})^\dagger \tag{3.2.1}$$

where the V's are elements of $\mathcal{G}$. Denoting the unit vector in the direction of the i^{th} axis as $\hat{\mu}_i$ and the lattice link in the same direction originating at coordinate x as $U_{\mu_i}(x)$, then the trace of a product of n link variables around a closed path is

$$\mathcal{C} = \text{tr}\left[U_{\mu_1}(x)U_{\mu_2}(x+\hat{\mu}_1)\dots U_{\mu_n}(x-\hat{\mu}_n)\right]. \tag{3.2.2}$$

The path $\mathcal{C}$ transforms under the gauge group as

$$\begin{aligned}
\mathcal{C} \to &\,\text{tr}[V(x)U_{\mu_1}(x)V(x+\hat{\mu}_1)^\dagger V(x+\hat{\mu}_1)U_{\mu_2}(x+\hat{\mu}_1)V(x+\hat{\mu}_1+\hat{\mu}_2)\dots \\
&\times V(x-\hat{\mu}_n)U_{\mu_n}(x-\hat{\mu}_n)V(x)^\dagger] \\
=&\,\text{tr}\left[V(x)U_{\mu_1}(x)U_{\mu_2}(x+\hat{\mu}_1)\dots U_{\mu_n}(x-\hat{\mu}_n)V(x)^\dagger\right] \\
=&\,\text{tr}\left[U_{\mu_1}(x)U_{\mu_2}(x+\hat{\mu}_1)\dots U_{\mu_n}(x-\hat{\mu}_n)V(x)^\dagger V(x)\right] \\
=&\,\text{tr}\left[U_{\mu_1}(x)U_{\mu_2}(x+\hat{\mu}_1)\dots U_{\mu_n}(x-\hat{\mu}_n)\right]
\end{aligned} \tag{3.2.3}$$

where we have used the cyclic property of the trace in the penultimate line. Thus, the trace of a path-ordered product of link variables around a closed loop is gauge invariant.

If we define a path $\mathcal{C}$ that transforms in a given representation of the cubic group at a fixed time slice t and spatial location $\underline{x}$, then the operator, $\mathcal{O}(\underline{x},t)$, is given by

$$\mathcal{O}(\underline{x},t) = \text{tr}\left(\hat{\mathcal{P}}\prod_{\mathcal{C}} U_l\right) \tag{3.2.4}$$

where $\hat{\mathcal{P}}$ denotes the path ordering operator. This allows us to define the spatially averaged operator, $\Phi(t)$, as

$$\Phi(t) = \frac{1}{N_s^3}\sum_{\underline{x}} \mathcal{O}(\underline{x},t) \tag{3.2.5}$$

where N_s is the number of lattice sites in each direction on the (hypercubic) lattice.

Define the correlation function $C_T(t)$ as follows [64]:

$$C_T(t) \equiv \frac{1}{Z_T} \operatorname{tr}\left[\Phi^\dagger(t)\Phi(0)\right]_T = \frac{1}{Z_T} \sum_m \langle m|e^{-(T-t)H}\Phi^\dagger(0)e^{-tH}\Phi(0)|m\rangle \tag{3.2.6}$$

where Z_T is the normalisation factor:

$$Z_T = \operatorname{tr}\left[e^{-TH}\right] \tag{3.2.7}$$

and we are using the eigenstates of the Hamiltonian, H, as a complete set of orthonormal eigenstates. The operator $\Phi(0)$ creates, from the vacuum, a new state at time $t = 0$ and $\Phi^\dagger(t)$ annihilates the state at time t.

In addition, we are interested in measuring energies relative to the vacuum. In the case of the scalar glueball, the operator does not have a vanishing VEV so we simply redefine the operator creating such a state as

$$\overline{\Phi}(t) = \Phi(t) - \langle\Phi(t)\rangle. \tag{3.2.8}$$

Such operations are called vacuum-subtracted. Continuing from eq. (3.2.6), we insert a complete set of (orthonormal) glueball eigenstates into the correlation function. Without loss of generality, we may label the energies such that

$$E_0 \leqslant E_1 \leqslant E_2 \ldots \tag{3.2.9}$$

This gives

$$C_T(t) \;=\; \frac{1}{Z_T} \sum_{m,n} \langle m|e^{-(T-t)H}\Phi^\dagger(0)e^{-tH}\,|n\rangle\,\langle n|\,\Phi(0)|m\rangle$$

$$\begin{aligned}
\implies C_T(t) &= \frac{1}{Z_T}\sum_{m,n}\langle m|e^{-(T-t)E_m}\Phi^\dagger(0)e^{-tE_n}\,|n\rangle\,\langle n|\,\Phi(0)|m\rangle \\
\implies C_T(t) &= \frac{1}{Z_T}\sum_{m,n}|\langle n|\,\Phi(0)\,|m\rangle\,|^2 e^{-(T-t)E_m}e^{-tE_n}. \qquad (3.2.10)
\end{aligned}$$

We apply a similar process to the normalisation factor, Z_T:

$$\begin{aligned}
Z_T &= \sum_n \langle n|e^{-TH}|n\rangle \\
\implies Z_T &= \sum_n \langle n|n\rangle\, e^{-TE_n} \\
\implies Z_T &= \sum_n e^{-TE_n}. \qquad (3.2.11)
\end{aligned}$$

Now define

$$\Delta E_n \equiv E_n - E_0 \qquad (3.2.12)$$

(i.e. the difference between energy level n and the energy of the vacuum):

$$\begin{aligned}
C_T(t) &= \frac{\sum_{m,n}|\langle n|\,\Phi(0)\,|m\rangle\,|^2 e^{-(T-t)E_m}e^{-tE_n}}{e^{-TE_0}+e^{-TE_1}+e^{-TE_2}+\ldots} \\
\implies C_T(t) &= \frac{\sum_{m,n}|\langle n|\,\Phi(0)\,|m\rangle\,|^2 e^{-(T-t)\Delta E_m}e^{-t\Delta E_n}}{1+e^{-T\Delta E_1}+e^{-T\Delta E_2}+\ldots} \qquad (3.2.13)
\end{aligned}$$

We now determine

$$C(t) \equiv \lim_{T\to\infty} C_T(t). \qquad (3.2.14)$$

Note that $\Delta E_0 = 0$ by virtue of the operators being vacuum-subtracted; therefore, of the m terms, only $m = 0$ persists in this limit:

$$C(t) = \sum_n |\langle n|\,\Phi(0)\,|0\rangle\,|^2 e^{-t\Delta E_n}. \qquad (3.2.15)$$

For brevity, define $c_n \equiv \langle n|\Phi(0)|0\rangle$ and redefine $\Delta E_n \to E_n$. This shows that the correlation function is a sum of decaying exponentials:

$$C(t) = \sum_{n=1}^{\infty} |c_n|^2 e^{-tE_n}. \tag{3.2.16}$$

(The sum begins at $n = 1$ since c_0 is the VEV of the operator and all operators are vacuum-subtracted.) We also normalise the coefficients such that

$$\sum_{n=1}^{\infty} |c_n|^2 = 1. \tag{3.2.17}$$

As t becomes very large, the higher energies are suppressed ever more strongly and the correlator behaves like a single exponential:

$$\begin{aligned}
C(t) &= |c_1|^2 e^{-E_1 t} + |c_2|^2 e^{-E_2 t} + |c_3|^2 e^{-E_3 t} + \dots && (3.2.18)\\
\implies C(t) &= |c_1|^2 e^{-E_1 t}\left(1 + \frac{|c_2|^2}{|c_1|^2} e^{-(E_2 - E_1)t} + \frac{|c_3|^2}{|c_1|^2} e^{-(E_3 - E_1)t} + \dots\right) && (3.2.19)\\
\implies C(t) &\approx |c_1|^2 e^{-E_1 t} \quad \text{for } (E_2 - E_1)t \gg 1, && (3.2.20)
\end{aligned}$$

assuming that $c_1 \neq 0$. The inequality $(E_2 - E_1)t \gg 1$ implies that $(E_n - E_1)t \gg 1$ for all $n \geqslant 2$ since we have labelled the energies in order of non-decreasing magnitude as per eq. (3.2.9). Since we do not know the value of c_1, we take the ratio of $C(t)$ at different times to give

$$\begin{aligned}
\frac{e^{-E_1 t}}{e^{-E_1(t-t_0)}} &\approx \frac{C(t)}{C(t-t_0)}\\
\implies e^{-E_1 t_0} &\approx \frac{C(t)}{C(t-t_0)}\\
\implies E_1 &\approx -\frac{1}{t_0} \ln\left(\frac{C(t)}{C(t-t_0)}\right).
\end{aligned}$$

By virtue of $C(t)$ comprising zero-momentum operators, $E_1 = m_1$ hence

$$m_1 \approx -\frac{1}{t_0} \ln\left(\frac{C(t)}{C(t-t_0)}\right). \tag{3.2.21}$$

Since we can only approximate the ground state mass, we instead describe our measurement in eq. (3.2.21) as an *effective mass* (m_{eff}). That is a mass whose measurement picks up contributions from heavier states that have not been suppressed enough to be ignored. Since even the heaviest glueballs propagate across the earliest time slices, the effective mass of the glueball is always larger than its true mass. If we detect a plateau in the measurement of the effective mass, we make the assumption that this plateau extends to $t \to \infty$. At this point, we take the plateau to be the effective mass of the glueball.

3.3 Improved Operators for the Glueball Spectrum

Section 3.2 is rather idealised. We know that we can reduce the effects of contamination from more massive states by taking measurements at larger time values. However, while the lightest state will decay the most slowly, it will eventually become drowned out by statistical noise which is constant in time (i.e. the signal-to-noise ratio will decrease exponentially). Thus, determining the mass too early means that our value will have been affected by the more massive states, while determining the mass too late means that our measurement will not be able to rise above background fluctuations. (This demonstrates the counter-intuitive point that the more massive a glueball, the more difficult it is to determine its mass.)

Our solution to this conflict is to reduce the effects of more massive states at early times. In eq. (3.2.16), we required that the coefficient c_1 was non-zero. We now

focus our attention on making this coefficient larger in magnitude. Equation (3.2.17) will force the magnitude of the other coefficients to decrease. The advantage of doing this is that the effects of higher energy states will be diminished at early times due to their smaller coefficients and, conversely, the presence of the lightest glueball state will become more pronounced.

Going back to eq. (3.2.3) we see that $c_1 = \langle 1|\Phi(0)|0\rangle$. Since $\Phi(0)\,|0\rangle$ creates a state from the vacuum (at time $t = 0$), c_1 is the inner product of this state and the state $|1\rangle$ (the ground state of the glueball). Thus, increasing the magnitude of c_1 is equivalent to making $\Phi(0)\,|0\rangle$ have a larger overlap with the glueball ground state.

Two tried and tested methods to increase the overlap of the two states are known as "blocking" and "smearing" (see, for example, [65,66], respectively). One of the issues when we take the continuum limit is that, as the lattice spacing goes to zero, our glueball operators become ever smaller in terms of physical size. Since glueballs themselves have a physical size that is independent of the lattice spacing, as the lattice becomes finer our operators have a decreasing resemblance to what it is we are studying; the blocking method increases the physical size of the operators. Again, as we take progressively finer lattice spacings, our operators will become dominated by ultraviolet (i.e. short-distance) fluctuations. This will cause our operators to become sensitive to the physics occurring at the ultraviolet-cutoff; in general, the glueball state will not be sensitive to such scales. The smearing and blocking methods average links with their neighbours in order to iron out these ultraviolet fluctuations and reduce the dependence on the ultraviolet-cutoff.

- Blocking: The Blocking Algorithm increases the physical volume of the operators by an iterative procedure. At each step, the lattice link is doubled in length (forming a "super-link") and the corresponding "super-staples" are added to the

mix, the latter being weighted by some factor p_b. This process is depicted in fig. 3.1. A single lattice link after b blocking iterations is denoted by $\widetilde{U}^b_\mu(x)$ with $U^{b=0}_\mu(x) = U_\mu(x)$, the original lattice link (recall that Roman letters run from 1 to 3, inclusive). The tilde symbol is a reminder that, in general, a blocked link will not be a member of the gauge group. After each iteration, we must project the blocked link back to the gauge group: $\hat{\mathcal{G}}\{\widetilde{U}^b_i(x)\} = U^b_i(x) \in Sp(2N)$. The resymplectisation algorithms for this are described in section 2.7.

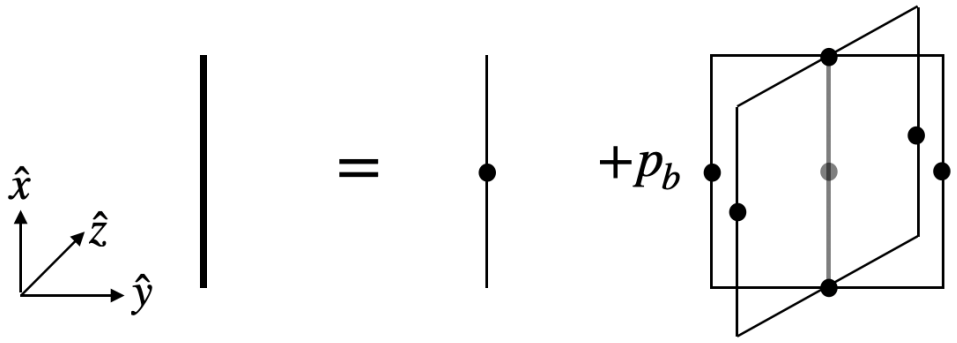

Figure 3.1: Left to right: a blocked link, a super-link and its super-staples. The Cartesian basis serves as a reminder that only the spatial links are used in the blocking procedure; the links themselves can lie in any of the three spatial planes.

One can define the initial state $U^0_i(x) = U_i(x)$ and iterate according to:

$$\begin{aligned}\widetilde{U}^{b+1}_i(x) = {} & U^b_i(x)U^b_i(x+2^b\hat{j}) \\ & + p_b \sum_{j\neq i} U^b_j(x)U^b_i(x+2^b\hat{j})U^b_i(x+2^b\hat{j}+2^b\hat{i})U^b_j(x+2^{b+1}\hat{i})^\dagger \\ & + p_b \sum_{j\neq i} U^b_j(x-2^b\hat{j})^\dagger U^b_i(x-2^b\hat{j})U^b_i(x-2^b\hat{j}+2^b\hat{i})U^b_j(x-2^b\hat{j}+2^{b+1}\hat{i}).\end{aligned} \tag{3.3.1}$$

On a hypercubic lattice with N_s sites in each dimension, the number of blocking

iterations is the greatest integer, n, such that $2^{n-1} \leqslant N_s$.

- Smearing: The Smearing algorithm is another iterative procedure this time designed to average out ultraviolet fluctuations. In this case we add to the original link its spatial staples weighted by a factor p_a (not the same factor as used in the blocking algorithm). This method was improved in [67] by adding the "diagonal-staples" of the corresponding link weighted by a different factor again, p_d. The diagonal staples are the paths with length of $5a$ that do not lie in a two-dimensional plane. These are demonstrated visually in fig. 3.2. If we include just the planar staples (the bold-blue one in fig. 3.2, this is known as APE smearing. We refer to the inclusion of the diagonal staples as "improved smearing".

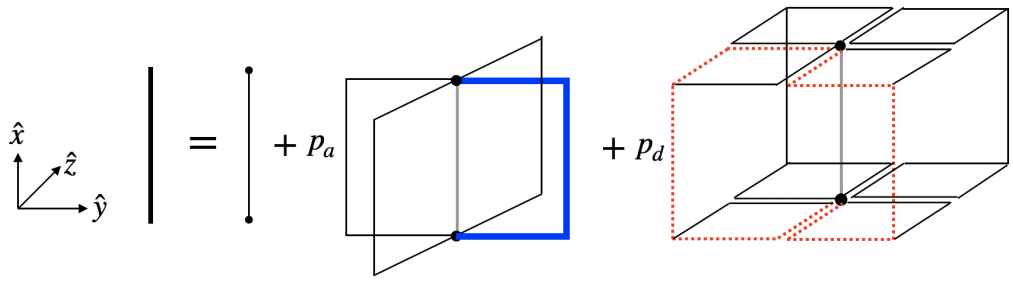

Figure 3.2: Left to right: a smeared link, the original link, the staples of the original link and the diagonal staples of the original link. In the second diagram from the right, a single staple is bold and highlighted in blue; on the far-right diagram, two different diagonal-staples are dotted and highlighted in red. The two super-staples that are highlighted demonstrate the possible shapes that they can take.

As with blocking, we define the initial state $U_i^0(x) = U_i(x)$ and must project the smeared link back to the gauge group after each iteration. The summation variables are positive in each term in eq. (3.3.2). The equation for an improved-

smeared link is given by [67]:

$$\begin{aligned}\widetilde{U}_i^{s+1}(x) = U_i^s(x) &+ p_a \sum_{j\neq i} U_j^s(x) U_i^s(x+\hat{j}) U_j^s(x+\hat{i})^\dagger \\ &+ p_a \sum_{j\neq i} U_j^s(x-\hat{j})^\dagger U_i^s(x-\hat{j}) U_j^s(x-\hat{j}+\hat{i}) \\ &+ p_d \sum_{j\neq i} \sum_{k\neq i,j} U_j^s(x) U_k^s(x+\hat{j}) U_i^s(x+\hat{j}+\hat{k}) \sum_{j'\neq i} \sum_{k'\neq i,j'} U_{j'}^s(x+\hat{i}+\hat{k}') U_{k'}^s(x+\hat{i})^\dagger \\ &+ p_d\{\text{rotations}\}.\end{aligned} \tag{3.3.2}$$

In eq. (3.3.2), the term whose coefficient is p_d is a single diagonal staple. The $p_d\{\text{rotations}\}$ term consists of the diagonal-staples obtained by rotating the explicit one through an angle of $\pi/2$ about the original link (in this case, the $\hat{i}$-axis). The smearing algorithm now consists of four planar-staples and sixteen nonplanar-staples.

The two aforementioned algorithms can be combined as demonstrated in [67]. We denote a smearing operation generalised to apply to blocked links as $\mathcal{S}$, by which we mean that the staples defined in eq. (3.3.2) are replaced with the superstaples described in eq. (3.3.1). From this, we define a link that has been blocked b times and smeared s times by

$$U_i^{b=1}(x) = U_i^s(x) U_i^s(x+\hat{i}), \tag{3.3.3}$$

$$U_i^{b=1,s}(x) = \mathcal{S}^s\{U_i^{b=1}(x)\}, \tag{3.3.4}$$

$$U_i^{b+1}(x) = U_i^{b,s}(x) U_i^{b,s}(x+2^b\hat{i}). \tag{3.3.5}$$

where $\mathcal{S}^s$ denotes the application of $\mathcal{S}$ a total of s times.

The combination of improved-smearing and blocking allows the benefits of op-

erators with a physical size as well as a finer resolution. The parameters p_a, p_b and p_d can be tuned in order to maximise the coefficient $|c_1|^2$.

In eq. (3.3.1), we see that the length of the blocked staple doubles with every blocking iteration. The parameter p_b determines the rate at which the blocked link increases in width. In order to keep these two rates of growth approximately the same, the blocking parameter p_b is chosen to be $\mathcal{O}(1)$. Extensive testing in [67] demonstrated that reasonable choices are $(p_a, p_d) = (0.30, 0.12)$ and $(p_a, p_d) = (0.40, 0.16)$ the latter of which is used in our glueball results.

In addition to blocking and smearing, we can improve the overlap with the glueball ground state by using multiple operators that transform in the same representation of the cubic group. The construction of such operators is described in section 3.4. Say we have a set of N_o operators each in the relevant representation of the cubic group: $\{\phi_i : i = 1, \ldots, N_o\}$[1]. We can construct an $N_o \times N_o$ correlation matrix in a similar way to eq. (3.2.6):

$$C_{ij}(t) = \langle \phi_i^\dagger(t)\phi_j(0)\rangle. \tag{3.3.6}$$

As explained in section 3.2, our best estimate for the glueball mass is our lowest measurement of the effective mass. Thus, we seek a linear combination of operators

$$\Phi(t) = \sum_{i=1}^{N_o} v_i\phi_i(t). \tag{3.3.7}$$

that minimises such a measurement. We can treat $\{v_i\}$ as the components of an N_o–dimensional vector.

This means that our original definitions of the correlation function and effective

[1]Once again the operators creating scalar states are vacuum subtracted as in eq. (3.2.8)

mass in eqs. (3.2.6) and (3.2.21), respectively, can be recast as

$$C(t) = \sum_{i=1}^{N_o} \sum_{j=1}^{N_o} v_i v_j C_{ij}(t) \tag{3.3.8}$$

and

$$m_{\text{eff}} = -\frac{1}{t} \ln \left(\frac{\sum_{ij} v_i v_j C_{ij}(t)}{\sum_{ij} v_i v_j C_{ij}(0)} \right). \tag{3.3.9}$$

From this, we deduce the generalised eigenvalue problem:

$$\begin{aligned} \sum_{i=1}^{N_o} \sum_{j=1}^{N_o} v_i v_j C_{ij}(t) &= e^{-m_{\text{eff}} t} \sum_{i=1}^{N_o} \sum_{j=1}^{N_o} v_i v_j C_{ij}(0) \\ \implies \sum_{j=1}^{N_o} v_j C_{ij}(t) &= e^{-m_{\text{eff}} t} \sum_{j=1}^{N_o} v_j C_{ij}(0). \end{aligned} \tag{3.3.10}$$

Denote the correlator in matrix form as $\mathbf{C}(t)$, the coefficients $\{v_i\}$ as a vector $\underline{v}$ and $\lambda(t) = e^{-m_{\text{eff}} t}$. We can rewrite the above as

$$\begin{aligned} \mathbf{C}(t)\underline{v} &= \lambda(t)\mathbf{C}(0)\underline{v} \\ \implies \mathbf{C}^{-1}(0)\mathbf{C}(t)\underline{v} &= \lambda(t)\underline{v} \end{aligned} \tag{3.3.11}$$

So we have reduced the determination of the glueball masses to the determination of the eigenvalues of an $N_o \times N_o$ matrix $\mathbf{C}^{-1}(0)\mathbf{C}(t)$. The largest of these eigenvalues corresponds to the lowest glueball mass. One method of determining eigenvalues is by diagonalising the corresponding matrix. Denote the (diagonal) components of same by $D_{ii}(t)$ with no sum on the repeated index i.

The periodicity of the lattice allows for the propagation of glueballs backwards

in time. We can take these into account by converting the exponential decay into a hyperbolic-cosine function giving:

$$\begin{aligned} & D_{ii}(t) \propto e^{-m_i t} + e^{-m_i(L-t)} \quad \text{(no sum on } i\text{)} \\ \Longrightarrow\ & D_{ii}(t) \propto e^{-am_i \bar{t}} + e^{-am_i(N_t-\bar{t})} \\ \Longrightarrow\ & D_{ii}(t) \propto e^{-am_i(\bar{t}-N_t/2)} + e^{am_i(\bar{t}-N_t/2)} \\ \Longrightarrow\ & D_{ii}(\bar{t}) = A\cosh\left(am_i\left(\bar{t}-\frac{N_t}{2}\right)\right). \end{aligned} \tag{3.3.12}$$

In the second line, we have changed the variable from t to the dimensionless (integer) quantity $\bar{t}$ which is the time-slice on the lattice as opposed to the value of Euclidean time ($t = a\bar{t}$) and A is a constant. Making use of the identity

$$\cosh x + \cosh y = 2\cosh\left(\frac{x+y}{2}\right)\cosh\left(\frac{x-y}{2}\right) \tag{3.3.13}$$

gives us the effective mass in lattice units

$$am_i(\bar{t}) = \operatorname{arcosh}\left(\frac{D_{ii}(\bar{t}+1)+D_{ii}(\bar{t}-1)}{2D_{ii}(\bar{t})}\right) \quad \text{(no sum on } i\text{)}. \tag{3.3.14}$$

Once this quantity reaches a plateau, we can say with confidence that the ground state is the dominant contribution to the sum of decaying exponentials. The effective masses are fitted to the curve in the t-interval in which $am_i(\bar{t})$ exhibits a plateau.

After fitting the glueball data to the curve, the covariance matrix corresponding to the fit parameters is determined. The diagonal components each correspond to the squared uncertainty in the fit parameter and, hence, the square-roots of these quantities are treated as the errors in the measurements.

In some cases, systematic errors in the mass plateaux are larger than its sta-

tistical errors. As explained in [14], this means that we cannot define a value of the reduced chi-squared and the corresponding entry in our table of results in section 3.8 is left blank.

To summarise the process for determining the glueball mass in a given representation of O_h with a given parity P:

1. We construct a set of glueball operators $\{\phi_i\}$ (described in section 3.4) each of which transforms in the relevant representation of the cubic group as well as having the relevant parity and charge conjugation.

2. We work to maximise the glueball signal by the methods of blocking and improved-smearing.

3. We construct a correlation matrix $C_{ij}(t) = \langle \phi_i^\dagger(t)\phi_j(0)\rangle$.

4. We diagonalise $C_{ij}(t)$ to give $D_{ii}(t)$ in order to determine the eigenvalues of the former.

5. We determine the corresponding mass (in lattice units) according to eq. (3.3.14) and look for the values of t for which the effective masses exhibit a plateau.

6. Finally, the function (3.3.14) is fitted to the effective mass measurements in the plateau interval with the errors being determined by the diagonal elements of the corresponding covariance matrix.

We anticipate that not all the computed eigenvalues will give reliable measurements for the corresponding glueball mass. The blocking and smearing processes serve to improve the signal of the ground state but, in practice, does not help for the signals of more massive (excited) states. We must either content ourselves with not computing the higher masses or find another way to improve the signals of the excited states.

3.4 Glueball Operators

The operators used to probe the glueball spectrum are gauge invariant products of link variables that transform under irreducible representations of O_h. They are constructed by taking the trace of a path-ordered product of lattice links (each of which is a separate element of $Sp(2N)$) forming a particular shape that transforms in a given representation of the octahedral group.

Let us allow for an example by going back to continuous spacetime. A continuum glueball with spin-s will have $2s+1$ possible spin states $(-s, -s+1, \ldots, s-1, s)$. Hence, the glueball will live in a $(2s+1)$-dimensional representation of the rotation group $SO(3)$. It follows naturally from this that a glueball on the lattice will live in an irreducible representation of the group O_h. There exist five such representations denoted by A_1, A_2, E, T_1 and T_2; these have dimensions 1, 1, 2, 3 and 3, respectively. This is the same notation as in [14].

In order to determine which states are produced in the continuum limit, we examine the behaviour of an $SO(3)$ representation restricted to the discrete ones of the octahedral group. These are known as subduced representations. An irreducible representation of $SO(3)$ (denoted by J) restricted to O_h, is denoted by $J \downarrow O$. These are shown in table 3.1 up to and including a continuum state of spin-6. This decomposition is used to identify continuous spin in lattice results. For example, if we wish to determine the mass of a continuum glueball of spin 2, we seek a mass that is degenerate in the representations E and T_2. Such degeneracies are observed in section 3.8.

We collate the work contained in [68–71] to show how operators that create glueball states are constructed. We know that operators are composed of closed loops

J	Octahedral decomposition
0	A_1
1	T_1
2	$E \oplus T_2$
3	$A_2 \oplus T_1 \oplus T_2$
4	$A_1 \oplus E \oplus T_1 \oplus T_2$
5	$E \oplus T_1 \oplus T_1 \oplus T_2$
6	$A_1 \oplus A_2 \oplus E \oplus T_1 \oplus T_2 \oplus T_2$

Table 3.1: Continuum glueball states of spin J and their corresponding decomposition in irreducible representations of the octahedral group [68] for integer spins 0 to 6, inclusive.

of lattice links. A single loop, $\mathcal{C}$, can be written as

$$\mathcal{C} = [f_1, f_2, ..., f_L] \tag{3.4.1}$$

where L is the length of the loop (i.e. the number of lattice links comprising the loop). We have, in essence, condensed the notation of eq. (3.2.2). Each f_i is one of the basis vectors $\{\vec{e}_i\}$ that span the three spatial dimensions. The restriction to a fixed time-slice creates operators with zero momentum. The fact that the loop is closed implies

$$\sum_{i=1}^{L} f_i = 0. \tag{3.4.2}$$

Similarly, the fact we take the trace of the product of link variables means that cyclic permutations of $\{f_i\}$ all correspond to the same contour just as the trace operator is invariant under cyclic permutations of the matrices within it.

Under the action of a group element, r, the loop transforms as

$$r\mathcal{C} = [rf_1, rf_2, ..., rf_L]. \tag{3.4.3}$$

A basis for the irreducible representations of O_h can be constructed from any closed loop. A single closed loop is transformed under the action of the group, O_h, and linear combinations of these transformations are combined so as to construct each of the five irreducible representations [72].

If we have a closed loop $\mathcal{P}$, and wish to construct a basis for the representation $\mathcal{R}$, we use the 24×24 matrix contained in Table 1 of [71] to obtain the correct linear combination. In general, the more operators, the better the glueball signal but this will be subject to diminishing returns as computation time increases.

3.5 String Tension

The string tension can be determined in a similar way to the mass of the glueballs. To do this, we must understand the mechanism behind confinement. If two colour charges are separated by a very large distance, r, they have an interaction potential that is approximately linear in r with the string tension, σ, being the constant of proportionality. At large distances, the confining potential of eq. (3.0.1) is dominated by the linear term. The latter is due to the formation of thin flux tubes between the sources. These flux tubes have an effective dynamics described by string theory. The two charges form the ends of a single open string for which the string tension is the energy per unit length. Note that this is a function of temperature.

The system exhibits a phase transition between the confined and deconfined phases. At this stage, we need only concern ourselves with the order parameter for confinement known as the Polyakov loop (also called the Wilson line). On the lattice,

the Polyakov loop at spatial coordinate $\underline{x}$ is given by

$$P(\underline{x}) = \mathrm{tr}\left[\prod_{t=0}^{N_t-1} U_4(\underline{x}, t)\right] \tag{3.5.1}$$

with the average Polyakov loop equal to

$$\langle P \rangle = \frac{1}{N_s^3} \sum_{\text{spatial coords.}} P(\underline{x}). \tag{3.5.2}$$

$U_4(\underline{x}, t)$ is the lattice link at spacetime coordinate $(\underline{x}, t)$ in the temporal direction. The length of the loop is equal to aN_t.

We can define a correlation function of Polyakov loops to probe the structure of two static quarks carrying opposite charges. If a quark and antiquark are positioned at $\underline{0}$ and $\underline{x}$, respectively, the VEV of two Polyakov loops is related to the free energy of a single quark, F, via [73]

$$\langle P \rangle \sim e^{-F/T}, \tag{3.5.3}$$

where T is the temperature. If this VEV evaluates to zero, the free energy of a single quark diverges and we require infinite energy to create a free quark; this is symbolic of confinement. When the correlator is positive, the system deconfines and a free quark has finite energy.

In order to determine the string tension, σ, we can evaluate the torelon mass. A torelon is a flux tube that wraps around the lattice and whose mass is related to the total energy of the whole string and, hence, the string tension. The flux tube can wrap around in the temporal or any of the three spatial directions. This gives us four measurements in total for the torelon mass which, on an isotropic lattice, we expect to be statistically compatible. Torelon masses can be determined from correlators of

Polyakov loops.

We use the same description of torelons and flux tubes as in [14]. The torelon is described as a one-dimensional object. Classically, the string tension, σ, is defined as its energy, m_T, per unit length, L:

$$\sigma = \frac{m}{L} \quad \text{(classically)}. \tag{3.5.4}$$

In practice, the finite length of the string introduces corrections to the torelon mass and we expand in inverse powers of σL:

$$m_T = \sigma L \left(1 + \sum_{k=1}^{\infty} \frac{d_k}{(\sigma L^2)^k}\right). \tag{3.5.5}$$

This is in agreement with the classical equation, (3.5.4), as $L \to \infty$. Symmetries and universality allow us to determine some of these coefficients explicitly. Expanding the above to second order returns

$$m_T = \sigma L \left(1 + \frac{d_1}{\sigma L^2} + \frac{d_2}{(\sigma L^2)^2}\right) \tag{3.5.6}$$

$$m_T = \sigma L + \frac{d_1}{L} + \frac{d_2}{\sigma L^3}. \tag{3.5.7}$$

The first order expansion was also performed in [74] where the term d_1 was shown to be $-\pi/3$ in 4 dimensions. The second term can also be evaluated as $d_2 = -\pi^2/18$.

The next-to-leading order formula can also be produced by the Nambu-Goto formula for the mass of a torelon:

$$m_T = \sigma L \sqrt{1 - \frac{2\pi}{3\sigma L^2}} \tag{3.5.8}$$

Expanding to $\mathcal{O}(1/\sigma L^3)$, returns

$$m_T = \sigma L - \frac{\pi}{3L} - \frac{\pi^2}{18\sigma L^3}. \tag{3.5.9}$$

These are elements of effective string-theory that we do not discuss further here, as they go beyond the scope of the calculation.

In each equation relating the torelon mass to string tension, the torelon itself can be associated with either the temporal or spatial direction. This gives us two measurements for the string tension: σ_s (which, itself, is the average of the three spatial directions) and σ_t, respectively. Following standard procedures, the two results can be combined to give a weighted average for the error ($\Delta\sqrt{\sigma}$) and a weighted average for the string tension ($\sqrt{\sigma}$) as in [5]:

$$\left(\frac{1}{\Delta\sqrt{\sigma}}\right)^2 = \left(\frac{1}{\Delta\sqrt{\sigma_s}}\right)^2 + \left(\frac{1}{\Delta\sqrt{\sigma_t}}\right)^2, \tag{3.5.10}$$

$$\frac{\sqrt{\sigma}}{(\Delta\sqrt{\sigma})^2} = \frac{\sqrt{\sigma_s}}{(\Delta\sqrt{\sigma_s})^2} + \frac{\sqrt{\sigma_t}}{(\Delta\sqrt{\sigma_t})^2}. \tag{3.5.11}$$

As well as providing a test for confinement, the measurement of $\sqrt{\sigma}$ also sets the scale of masses. As in the case of glueball masses, the torelon masses are initially computed in units of inverse lattice spacing (am is a dimensionless quantity). The corresponding dimensionless quantity we obtain for string tension is in units of inverse-squared lattice spacing ($a^2\sigma$ is a dimensionless quantity). Therefore, the ratio $m/\sqrt{\sigma}$ is also dimensionless.

3.6 Thermodynamic, Continuum and Large-N Limits

The lattice is a discretisation of spacetime that has been used to make the computation of observables amenable to super-computers. The original motive, however, is to measure the observables in our continuum universe and these have to be determined by extrapolating our discrete results to the continuum limit. In addition, the finite extent of the lattice will affect our results. We account for these by extrapolating to the infinite volume or "thermodynamic" limit. As well as this, we wish to compute our results in the limit of $N_c \to \infty$. Unlike the thermodynamic- and continuum-extrapolations, this is not simply to wash out lattice artefacts from our calculation. The aim is to explore the physics that emerges in this limit as explained at the beginning of this chapter.

3.6.1 Thermodynamic limit

The finite extent of the lattice has an effect on our measurement of observables. Although boundary effects are mitigated by making the lattice toroidal in all directions to maintain (discrete) translational symmetry, the finite extent of the lattice still leaves its mark. The finite size effects are quantified by [74]:

$$m(L) = m_\infty \left[1 + \frac{b \exp\left(-\frac{\sqrt{3}}{2} m_\infty L \right)}{m_\infty L} \right] . \tag{3.6.1}$$

In the above, $m(L)$ is the glueball mass at finite volume $V = L^3$, m_∞ is the same mass in the thermodynamic limit and b is a constant that should only depend on the glueball state R^P. We can either compute the mass in infinite volume for a given finite volume using eq. (3.6.1) or we can work such that the finite size effects can be ignored. If we

take L to be sufficiently large, the corrections due to the finite volume will be smaller than the statistical errors from the Monte-Carlo evaluation of the masses themselves. We find that this occurs at the point where $L\sqrt{\sigma} \gtrsim 3$ [5]. Finer lattices correspond to larger values of inverse-coupling so lattice volumes must increase with β in order to maintain the absence of finite size effects.

3.6.2 Continuum limit

The masses we compute for glueballs from section 3.3 are in lattice units:

$$am \to \frac{amc}{\hbar} \quad \text{(reinserting the factors of } \hbar \text{ and } c\text{)}. \tag{3.6.2}$$

These are the units that come directly out of the computation but are of little use in computing the masses in the continuum limit. We need to remove the factor of a from our measurements of m otherwise we will obtain zero when sending $a \to 0$. The most direct way to carry out the extrapolation is to express the masses in units of the square root of the string tension, $\sqrt{\sigma}$, which can be interpreted as a mass scale as stated in section 3.5. In addition, the string tension can be computed in much the same way as the glueball masses and the torelons typically have a low mass allowing for a simple determination of the string tension. The corrections to the continuum action are of the order a^2:

$$S_{\text{continuum}} = S_{\text{Wilson}} + \mathcal{O}(a^2). \tag{3.6.3}$$

One can show that the corrections to the continuum masses are of the same order. Hence, we extrapolate the glueball masses to the continuum limit with the ansatz

$$\frac{m(0)}{\sqrt{\sigma}} = \frac{m(a)}{\sqrt{\sigma}} + k_1 a^2 \sigma \tag{3.6.4}$$

where k_1 is a constant that depends on the glueball state R^P to be determined numerically. The factor of σ is necessary to match the dimensions of the two sides of the equation.

The expression in eq. (3.6.4) assumes that terms of order a^4 are negligible compared to those of order a^2. The lattice action can be improved by adding terms that cancel the $\mathcal{O}(a^2)$ ones resulting in the corrections being $\mathcal{O}(a^4)$ or higher. This effects a faster convergence to the continuum limit but throughout this thesis, we content ourselves with the Wilson action stated in eq. (3.1.1).

3.6.3 Large-N limit

Large-N extrapolations have been carried out for $SU(N)$ theories in, for example, [75–77]. The extrapolation of $N \to \infty$, however, is slightly different for $Sp(2N)$ than it is for $SU(N)$. The three groups $SU(N)$, $SO(N)$ and $Sp(2N)$ were all examined by Lovelace in [60] and the extrapolation to large-N for $Sp(2N)$ was found to be $\mathcal{O}(1/N)$ rather than $\mathcal{O}(1/N^2)$ as it is for $SU(N)$.

Thus, the corrections to the glueball masses for finite N are given by

$$\frac{m(\infty)}{\sqrt{\sigma}} = \frac{m(N)}{\sqrt{\sigma}} + \frac{k_2}{N^2} \quad \text{for } SU(N), \tag{3.6.5}$$

$$\frac{m(\infty)}{\sqrt{\sigma}} = \frac{m(2N)}{\sqrt{\sigma}} + \frac{k_2'}{2N} \quad \text{for } Sp(2N). \tag{3.6.6}$$

where k_2 and k_2' are constants that depend on the glueball state R^P (and the gauge group) to be determined numerically just as k_1 in eq. (3.6.4).

3.7 Casimir Scaling

The hypothesis of Casimir scaling is tested in this thesis. Introduced in [61], we can define the ratio η as

$$\eta(0^{++}) \equiv \frac{m_{0^{++}}^2}{\sigma}\frac{C_2(F)}{C_2(A)}. \tag{3.7.1}$$

In the above, $m_{0^{++}}$ is the mass of the scalar glueball with positive parity and positive charge-conjugation; σ is the string tension; $C_2(F)$ and $C_2(A)$ are the quadratic Casimirs in the fundamental and adjoint representations of the gauge group, respectively. The conjecture is that the constant η depends solely on the number of spacetime dimensions. Since Casimir scaling applies to any gauge group, we have reintroduced the label for charge conjugation since such states will exist in gauge theories other than $Sp(2N)$. The ratios of the Casimir operators are

$$\frac{C_2(F)}{C_2(A)} = \begin{cases} \frac{N_c^2-1}{2N_c^2} & \text{for } SU(N_c) \\ \frac{N_c-1}{2N_c-4} & \text{for } SO(N_c) \\ \frac{N_c+1}{2N_c+4} & \text{for } Sp(N_c). \end{cases} \tag{3.7.2}$$

While we have typically written the symplectic groups in the form $Sp(2N)$, we have written it here in terms of the explicit number of charges, N_c, for the sake of consistency with the other two groups. Note that, in all cases,

$$\frac{C_2(F)}{C_2(A)} \to \frac{1}{2} \text{ as } N_c \to \infty. \tag{3.7.3}$$

This corroborates our understanding that the three aforementioned groups all produce the same physics in the large-N_c limit.

$Sp(2)$		
L/a	β	$a\sqrt{\sigma}$
10	2.2986	0.3583(73)
12	2.3726	0.2713(57)
16	2.4265	0.2379(21)
20	2.5115	0.1765(18)
24	2.6	0.13096(99)
26	2.62	0.1260(22)
32	2.7	0.09685(93)

Table 3.2: Square-root of string tension in units of inverse lattice spacing ($a\sqrt{\sigma}$) for $Sp(2)$ [14]. The string tension is computed using the spatial torelon mass and the Nambu-Goto formula for the string tension in eq. (3.5.8).

$Sp(4)$		
L/a	β	$a\sqrt{\sigma}$
16	7.62	0.2478(44)
16	7.7	0.2273(26)
18	7.85	0.1878(14)
20	8.0	0.1577(21)
26	8.2	0.1295(10)
32	8.3	0.1124(28)

Table 3.3: Square-root of string tension in units of inverse lattice spacing ($a\sqrt{\sigma}$) for $Sp(4)$ [14]. The string tension is computed using the spatial torelon mass and the Nambu-Goto formula for the string tension in eq. (3.5.8).

3.8 Results

Here we collate the glueball results for $Sp(2N)$ gauge theories. We include the glueball masses at different values of lattice spacing as well as the extrapolations to the continuum limit. We include the aforementioned for finite N as well as the large-N extrapolations of the continuum results. In addition, we compare our results for $Sp(2N)$ to existing results in $SU(N)$ where possible. Finally, we examine the hypothesis of Casimir Scaling.

As discussed earlier, the observable $\sqrt{\sigma}$ will be used to set the scale for all values of the lattice spacing, thus providing one way to compare the lattice spacing at different beta values. These results are contained in tables 3.2 to 3.5.

We collate all the lattice glueball masses of $Sp(2N)$ for $N = 1, 2, 3$ and 4 in tables 3.6 to 3.17. Interspersed within the tables of data, we plot the lattice results along with their continuum extrapolations for each channel as computed by eq. (3.6.4). The

$Sp(6)$		
L/a	β	$a\sqrt{\sigma}$
12	15.6	0.2542(16)
12	15.65	0.2565(21)
12	15.7	0.2433(15)
14	15.85	0.2209(14)
16	16.1	0.1871(16)
20	16.3	0.1681(29)
20	16.5	0.1518(11)
28	16.7	0.1351(11)
24	16.8	0.1267(13)
28	17.1	0.1088(24)

Table 3.4: Square-root of string tension in units of inverse lattice spacing ($a\sqrt{\sigma}$) for $Sp(6)$ [14]. The string tension is computed using the spatial torelon mass and the Nambu-Goto formula for the string tension in eq. (3.5.8). (The values of $a\sqrt{\sigma}$ for $\beta = 16.7$ and $\beta = 16.8$ were stated the wrong way round in [14] and are corrected in this table.)

$Sp(8)$		
L/a	β	$a\sqrt{\sigma}$
14	26.5	0.2527(17)
14	26.7	0.2343(32)
14	26.8	0.2224(16)
16	27.0	0.2089(15)
16	27.2	0.1909(15)
16	27.3	0.1840(15)
18	27.6	0.1652(15)
20	27.9	0.1518(18)
22	28.3	0.1367(18)

Table 3.5: Square-root of string tension in units of inverse lattice spacing ($a\sqrt{\sigma}$) for $Sp(8)$ [14]. The string tension is computed using the spatial torelon mass and the Nambu-Goto formula for the string tension in eq. (3.5.8).

R^P \ $(L/a,\beta)$	$(10, 2.2986)$		$(12, 2.3726)$		$(16, 2.4265)$	
	$am(R^P)$	χ^2/d.o.f.	$am(R^P)$	χ^2/d.o.f.	$am(R^P)$	χ^2/d.o.f.
A_1^+	1.150(70)	–	0.995(19)	0.77	0.883(32)	2.1
A_1^{+*}	1.99(13)	0.41	1.52(12)	–	0.700(80)	–
A_1^-	2.11(23)	1.02	1.53(30)	–	1.430(80)	–
A_1^{-*}	2.33(20)	–	2.45(45)	–	1.83(24)	–
A_2^+	2.05(60)	–	2.25(17)	1.82	1.82(17)	–
A_2^-	–	–	–	–	1.99(20)	–
E^+	2.00(50)	–	1.24(25)	–	1.229(98)	1.99
E^-	2.10(40)	–	2.07(14)	0.64	1.59(14)	–
T_1^+	–	–	1.80(30)	–	1.70(30)	–
T_1^-	–	–	2.00(20)	–	1.50(15)	–
T_2^+	2.00(30)	–	1.50(20)	–	1.32(12)	1.42
T_2^-	2.30(30)	–	2.14(15)	0.28	1.670(60)	–
String Tension	$a^2\sigma_s$	χ^2/d.o.f.	$a^2\sigma_s$	χ^2/d.o.f.	$a^2\sigma_s$	χ^2/d.o.f.
	0.1284(52)	–	0.0736(31)	–	0.0566(10)	–

Table 3.6: $Sp(2)$ glueball masses and string tensions. The measurements are expressed in the form "$m(\delta m)$" where m is the measured mass of the glueball in units of inverse lattice-spacing and δm is the statistical error in the measurement.

values of $a^2\sigma$ for $\beta = 16.7$ and $\beta = 16.8$ in $Sp(6)$ were tabulated the wrong way round in [14]. They appear in the correct order in these tables. In some instances the reduced chi-squared value is not reported. This is because the corresponding measurement could be extracted only from a small number of data points (two or three) and the number of data points is insufficient to associate this quantity with a useful measure of goodness of fit. The errors are computed by the method outlined at the end of section 3.3.

We also collate the data for Casimir scaling. As mentioned in section 3.7, there exists the hypothesis that the quantity

$$\eta(0^{++}) \equiv \frac{m_{0^{++}}^2}{\sigma}\frac{C_2(F)}{C_2(A)} \tag{3.8.1}$$

R^P \ $(L/a, \beta)$	$(20, 2.5115)$		$(24, 2.6)$	
	$am(R^P)$	χ^2/d.o.f.	$am(R^P)$	χ^2/d.o.f.
A_1^+	0.683(14)	3.36	0.467(24)	2.16
A_1^{+*}	0.500(40)	–	0.97(11)	–
A_1^-	1.030(60)	–	0.810(22)	2.74
A_1^{-*}	1.30(20)	–	0.96(10)	–
A_2^+	1.370(90)	–	0.900(90)	–
A_2^-	1.50(20)	–	1.21(12)	–
E^+	0.950(60)	–	0.702(33)	2.58
E^-	1.220(60)	–	0.890(60)	–
T_1^+	1.37(20)	–	1.050(80)	–
T_1^-	1.50(15)	–	1.180(80)	–
T_2^+	0.980(13)	2.78	0.690(50)	–
T_2^-	1.170(80)	–	0.900(50)	–
String Tension	$a^2\sigma_s$	χ^2/d.o.f.	$a^2\sigma_s$	χ^2/d.o.f.
	0.03116(63)	–	0.01715(26)	–

Table 3.7: $Sp(2)$ glueball masses and string tensions. The measurements are expressed in the form "$m(\delta m)$" where m is the measured mass of the glueball in units of inverse lattice-spacing and δm is the statistical error in the measurement.

$(L/a, \beta)$ / R^P	$(26, 2.62)$		$(32, 2.7)$	
	$am(R^P)$	χ^2/d.o.f.	$am(R^P)$	χ^2/d.o.f.
A_1^+	0.487(32)	2.82	0.356(10)	0.71
A_1^{+*}	0.680(50)	–	1.390(90)	–
A_1^-	0.750(50)	–	0.600(14)	3.25
A_1^{-*}	0.940(90)	–	0.750(30)	–
A_2^+	0.896(28)	2.81	0.680(50)	–
A_2^-	1.080(90)	–	0.980(40)	–
E^+	0.667(13)	2.71	0.507(28)	2.91
E^-	0.780(90)	–	0.680(50)	–
T_1^+	1.000(70)	–	0.820(40)	–
T_1^-	1.140(40)	–	0.900(50)	–
T_2^+	0.660(40)	–	0.490(30)	–
T_2^-	0.830(50)	–	0.687(65)	–
String Tension	$a^2\sigma_s$	χ^2/d.o.f.	$a^2\sigma_s$	χ^2/d.o.f.
	0.01587(56)	–	0.00938(18)	–

Table 3.8: $Sp(2)$ glueball masses and string tensions. The measurements are expressed in the form "$m(\delta m)$" where m is the measured mass of the glueball in units of inverse lattice-spacing and δm is the statistical error in the measurement.

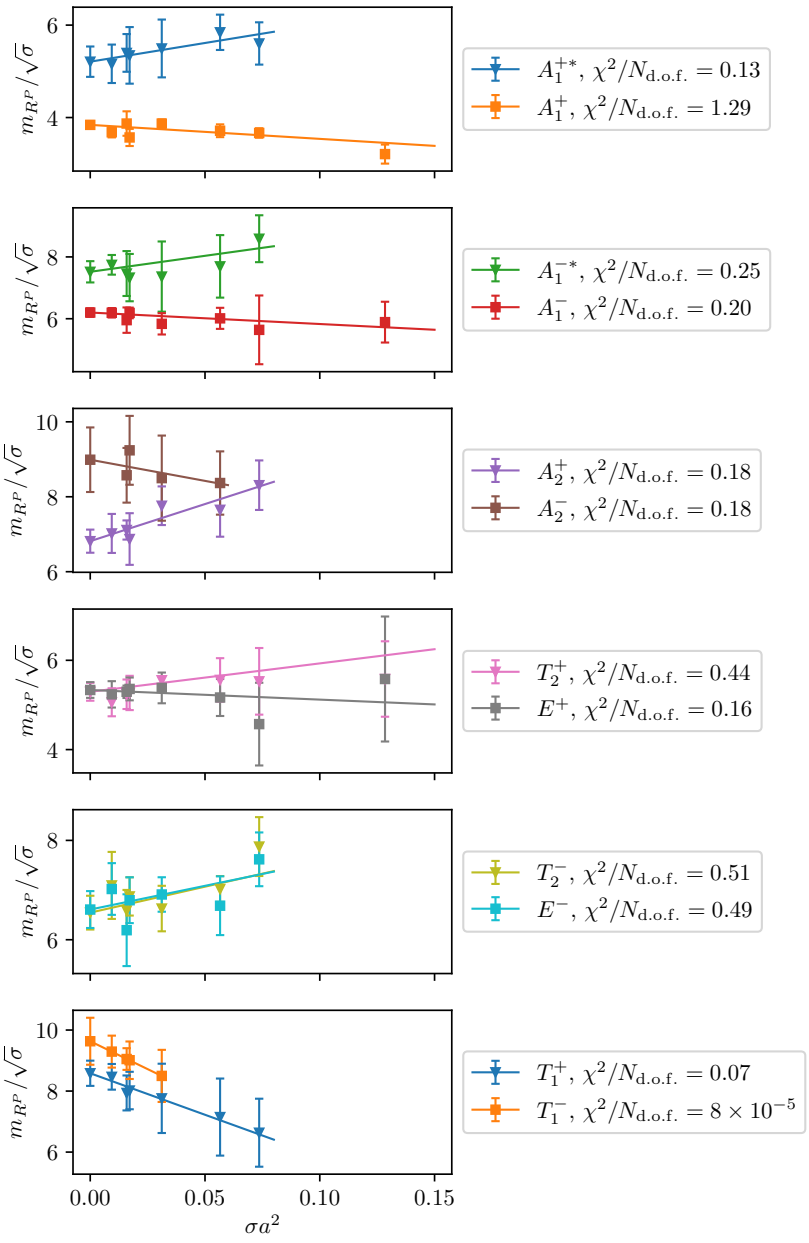

Figure 3.3: Lattice glueball masses and their continuum limit extrapolations for the gauge group $Sp(2N)$ at $N = 1$. The values plotted at $a^2\sigma$=0 are the continuum limits. Note the emergence of degeneracies between the T_2 and E states of matching parity.

R^P \ $(L/a, \beta)$	$(16, 7.62)$		$(16, 7.7)$		$(18, 7.85)$	
	$am(R^P)$	χ^2/d.o.f.	$am(R^P)$	χ^2/d.o.f.	$am(R^P)$	χ^2/d.o.f.
A_1^+	0.680(80)	–	0.729(32)	1.62	0.634(22)	0.56
A_1^{+*}	–	–	1.15(16)	–	0.94(17)	–
A_1^-	1.21(20)	–	1.190(50)	–	0.980(60)	–
A_1^{-*}	1.57(32)	–	1.64(26)	–	1.39(12)	–
A_2^+	1.80(31)	–	1.36(30)	–	1.500(50)	–
A_2^-	–	–	1.85(30)	–	1.40(30)	–
E^+	0.96(24)	–	1.160(28)	1.86	0.910(50)	–
E^-	1.30(35)	–	1.24(20)	1.58	1.16(13)	–
T_1^+	–	–	1.30(30)	–	1.22(30)	–
T_1^-	1.60(40)	–	2.07(17)	0.56	1.58(17)	–
T_2^+	–	–	1.170(50)	–	1.014(49)	1.87
T_2^-	–	–	1.00(25)	–	1.22(14)	–
String Tension	$a^2\sigma_s$	χ^2/d.o.f.	$a^2\sigma_s$	χ^2/d.o.f.	$a^2\sigma_s$	χ^2/d.o.f.
	0.0614(22)	–	0.0517(12)	–	0.03526(51)	–

Table 3.9: $Sp(4)$ glueball masses and string tensions. The measurements are expressed in the form "$m(\delta m)$" where m is the measured mass of the glueball in units of inverse lattice-spacing and δm is the statistical error in the measurement.

R^P \ $(L/a,\beta)$	$(20, 8.0)$		$(26, 8.2)$		$(32, 8.3)$	
	$am(R^P)$	χ^2/d.o.f.	$am(R^P)$	χ^2/d.o.f.	$am(R^P)$	χ^2/d.o.f.
A_1^+	0.587(37)	1.42	0.445(21)	2.31	0.402(12)	1.57
A_1^{+*}	0.86(12)	–	0.710(80)	–	–	–
A_1^-	0.880(40)	–	0.700(40)	–	0.600(40)	–
A_1^{-*}	1.230(80)	–	0.970(90)	–	0.860(30)	–
A_2^+	1.03(20)	–	1.000(50)	–	0.880(70)	–
A_2^-	1.38(20)	–	1.02(14)	–	0.85(20)	–
E^+	0.810(50)	–	0.607(68)	2.31	0.590(20)	–
E^-	1.060(60)	–	0.820(30)	–	0.770(30)	–
T_1^+	1.05(20)	–	1.000(50)	–	0.790(30)	–
T_1^-	1.10(20)	–	1.160(70)	–	0.82(12)	–
T_2^+	0.760(40)	–	0.610(50)	–	0.570(50)	–
T_2^-	1.070(30)	–	0.820(60)	–	0.740(60)	–
String Tension	$a^2\sigma_s$	χ^2/d.o.f.	$a^2\sigma_s$	χ^2/d.o.f.	$a^2\sigma_s$	χ^2/d.o.f.
	0.02487(66)	–	0.01676(26)	–	0.01263(62)	–

Table 3.10: $Sp(4)$ glueball masses and string tensions. The measurements are expressed in the form "$m(\delta m)$" where m is the measured mass of the glueball in units of inverse lattice-spacing and δm is the statistical error in the measurement.

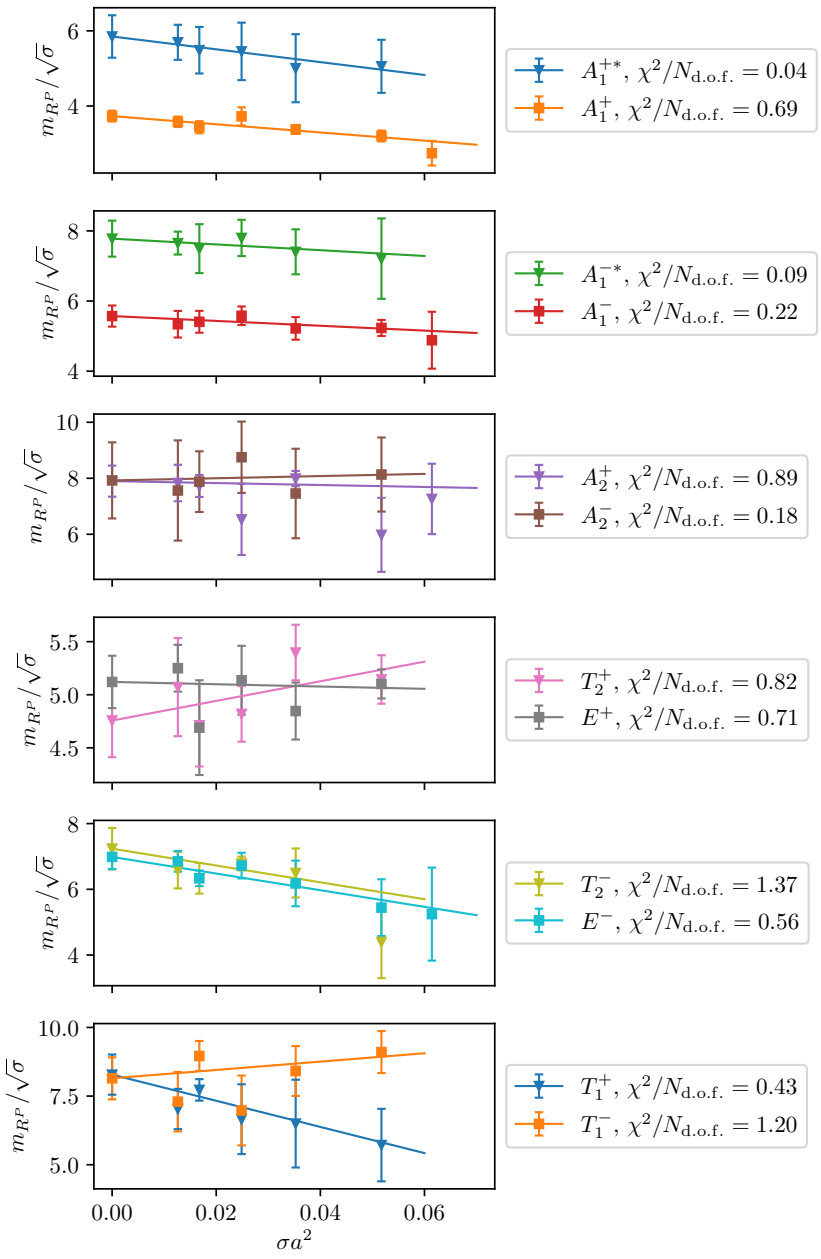

Figure 3.4: Lattice glueball masses and their continuum limit extrapolations for the gauge group $Sp(2N)$ at $N = 2$. The values plotted at $a^2\sigma$=0 are the continuum limits. Note the emergence of degeneracies between the T_2 and E states of matching parity.

R^P \ $(L/a, \beta)$	$(12, 15.6)$		$(12, 15.65)$		$(12, 15.7)$	
	$am(R^P)$	χ^2/d.o.f.	$am(R^P)$	χ^2/d.o.f.	$am(R^P)$	χ^2/d.o.f.
A_1^+	0.765(27)	0.18	0.777(26)	0.007	0.750(24)	0.56
A_1^{+*}	1.43(16)	0.99	1.29(12)	–	1.167(96)	1.28
A_1^-	1.29(13)	0.79	1.29(17)	1.92	1.27(17)	–
A_1^{-*}	1.93(28)	–	1.76(21)	–	1.667(80)	0.68
A_2^+	1.80(15)	–	1.92(11)	0.51	1.64(54)	1.94
A_2^-	1.80(30)	–	2.08(20)	–	2.00(30)	–
E^+	1.202(83)	2.37	1.257(31)	1.65	1.203(82)	1.38
E^-	1.46(15)	–	1.41(30)	–	1.33(18)	–
T_1^+	1.70(30)	–	2.00(18)	–	1.07(40)	–
T_1^-	1.37(35)	–	1.90(40)	–	2.25(35)	–
T_2^+	1.06(15)	–	1.23(12)	2.05	1.213(87)	2.94
T_2^-	1.50(13)	–	1.70(14)	–	1.40(20)	–
String Tension	$a^2\sigma_s$	χ^2/d.o.f.	$a^2\sigma_s$	χ^2/d.o.f.	$a^2\sigma_s$	χ^2/d.o.f.
	0.06464(79)	–	0.0663(11)	–	0.05918(72)	–

Table 3.11: $Sp(6)$ glueball masses and string tensions. The measurements are expressed in the form "$m(\delta m)$" where m is the measured mass of the glueball in units of inverse lattice-spacing and δm is the statistical error in the measurement.

R^P \ $(L/a, \beta)$	$(14, 15.85)$		$(16, 16.1)$		$(20, 16.3)$	
	$am(R^P)$	χ^2/d.o.f.	$am(R^P)$	χ^2/d.o.f.	$am(R^P)$	χ^2/d.o.f.
A_1^+	0.720(20)	–	0.581(28)	0.25	0.536(20)	2.09
A_1^{+*}	1.17(12)	–	0.95(12)	–	0.910(80)	–
A_1^-	1.07(12)	–	0.971(41)	0.49	0.846(36)	0.33
A_1^{-*}	1.24(15)	–	1.16(17)	–	1.031(53)	1.78
A_2^+	1.54(20)	–	1.488(38)	3.97	1.23(14)	–
A_2^-	1.60(30)	–	1.48(25)	–	1.50(12)	–
E^+	1.141(71)	3.88	0.954(35)	0.98	0.830(50)	–
E^-	1.26(12)	–	1.247(24)	1.94	1.090(70)	–
T_1^+	1.52(16)	–	1.50(10)	–	1.380(90)	–
T_1^-	1.70(40)	–	1.59(10)	–	1.20(16)	–
T_2^+	1.075(55)	0.49	0.854(85)	1.14	0.780(60)	–
T_2^-	1.37(14)	–	1.200(50)	–	1.080(81)	–
String Tension	$a^2\sigma_s$	χ^2/d.o.f.	$a^2\sigma_s$	χ^2/d.o.f.	$a^2\sigma_s$	χ^2/d.o.f.
	0.04879(60)	–	0.03501(59)	–	0.02825(99)	–

Table 3.12: $Sp(6)$ glueball masses and string tensions. The measurements are expressed in the form "$m(\delta m)$" where m is the measured mass of the glueball in units of inverse lattice-spacing and δm is the statistical error in the measurement.

$(L/a, \beta)$ / R^P	$(20, 16.5)$		$(28, 16.7)$	
	$am(R^P)$	χ^2/d.o.f.	$am(R^P)$	χ^2/d.o.f.
A_1^+	0.499(15)	0.11	0.432(10)	–
A_1^{+*}	0.810(60)	–	0.690(90)	–
A_1^-	0.808(21)	2.62	0.610(50)	–
A_1^{-*}	0.82(17)	–	0.72(16)	–
A_2^+	1.050(50)	–	0.92(12)	–
A_2^-	1.28(10)	–	1.12(10)	–
E^+	0.710(30)	–	0.650(30)	–
E^-	0.974(37)	0.33	0.830(50)	–
T_1^+	1.12(12)	–	0.920(80)	–
T_1^-	1.10(20)	–	1.21(10)	–
T_2^+	0.700(40)	–	0.636(20)	2.92
T_2^-	0.950(60)	–	0.772(60)	–
String Tension	$a^2\sigma_s$	χ^2/d.o.f.	$a^2\sigma_s$	χ^2/d.o.f.
	0.02303(33)	–	0.01824(30)	–

Table 3.13: $Sp(6)$ glueball masses and string tensions. The measurements are expressed in the form "$m(\delta m)$" where m is the measured mass of the glueball in units of inverse lattice-spacing and δm is the statistical error in the measurement.

$(L/a, \beta)$ / R^P	$(24, 16.8)$		$(28, 17.1)$	
	$am(R^P)$	χ^2/d.o.f.	$am(R^P)$	χ^2/d.o.f.
A_1^+	0.441(15)	–	0.360(14)	1.02
A_1^{+*}	0.730(70)	–	0.610(40)	–
A_1^-	0.66(12)	–	0.550(30)	–
A_1^{-*}	1.49(10)	–	0.970(90)	–
A_2^+	0.76(28)	–	0.764(77)	2.14
A_2^-	0.90(17)	–	0.99(13)	–
E^+	0.663(2)	1.93	0.560(18)	1.17
E^-	0.787(79)	3.98	0.690(50)	–
T_1^+	0.80(30)	–	0.73(14)	–
T_1^-	1.16(10)	–	0.85(15)	–
T_2^+	0.680(30)	–	0.558(19)	2.01
T_2^-	0.840(70)	–	0.730(40)	–
String Tension	$a^2\sigma_s$	χ^2/d.o.f.	$a^2\sigma_s$	χ^2/d.o.f.
	0.01606(33)	–	0.01183(52)	–

Table 3.14: $Sp(6)$ glueball masses and string tensions. The measurements are expressed in the form "$m(\delta m)$" where m is the measured mass of the glueball in units of inverse lattice-spacing and δm is the statistical error in the measurement.

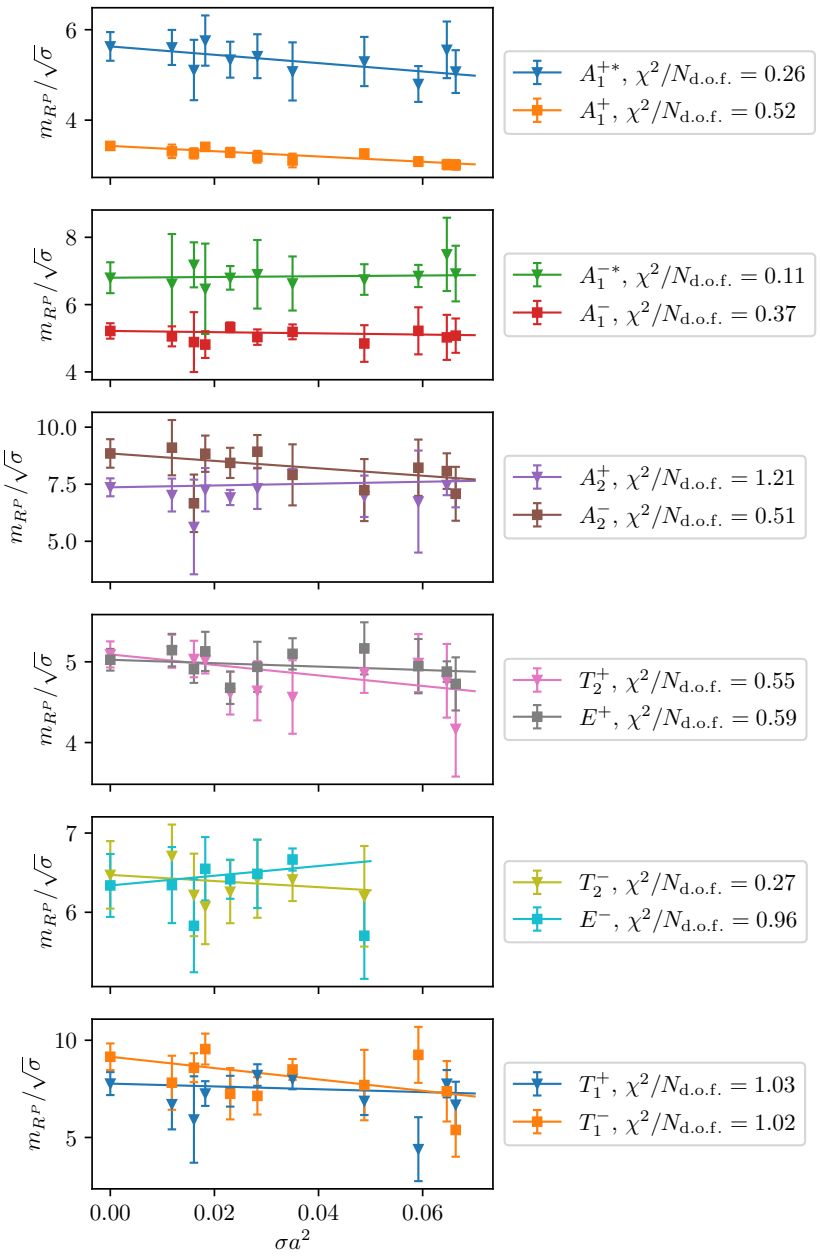

Figure 3.5: Lattice glueball masses and their continuum limit extrapolations for the gauge group $Sp(2N)$ at $N = 3$. The values plotted at $a^2\sigma$=0 are the continuum limits. Note the emergence of degeneracies between the T_2 and E states of matching parity.

R^P \ $(L/a, \beta)$	$(14, 26.5)$		$(14, 26.7)$		$(14, 26.8)$	
	$am(R^P)$	χ^2/d.o.f.	$am(R^P)$	χ^2/d.o.f.	$am(R^P)$	χ^2/d.o.f.
A_1^+	0.705(33)	2.88	0.734(12)	0.60	0.705(22)	0.26
A_1^{+*}	1.22(12)	–	1.262(88)	1.08	1.104(66)	2.13
A_1^-	1.230(80)	–	1.198(28)	1.06	1.140(60)	–
A_1^{-*}	1.73(26)	–	1.66(15)	–	1.564(48)	1.51
A_2^+	1.890(50)	–	1.21(25)	1.97	1.720(60)	–
A_2^-	2.03(12)	2.56	1.99(30)	–	2.06(15)	3.09
E^+	1.15(14)	–	1.156(69)	1.3	1.210(59)	12.53
E^-	1.620(40)	–	1.40(10)	–	1.26(13)	1.07
T_1^+	1.40(30)	–	1.50(15)	–	1.690(70)	–
T_1^-	1.50(30)	–	1.95(15)	–	1.94(10)	–
T_2^+	1.15(15)	–	1.081(67)	0.23	1.048(53)	1.38
T_2^-	1.60(10)	–	1.46(15)	–	1.370(40)	–
String Tension	$a^2\sigma_s$	χ^2/d.o.f.	$a^2\sigma_s$	χ^2/d.o.f.	$a^2\sigma_s$	χ^2/d.o.f.
	0.06386(85)	–	0.0549(15)	–	0.04947(72)	–

Table 3.15: $Sp(8)$ glueball masses and string tensions. The measurements are expressed in the form "$m(\delta m)$" where m is the measured mass of the glueball in units of inverse lattice-spacing and δm is the statistical error in the measurement.

$(L/a, \beta)$ / R^P	$(16, 27.0)$		$(16, 27.2)$		$(16, 27.3)$	
	$am(R^P)$	χ^2/d.o.f.	$am(R^P)$	χ^2/d.o.f.	$am(R^P)$	χ^2/d.o.f.
A_1^+	0.615(30)	0.008	0.610(20)	–	0.565(20)	1.96
A_1^{+*}	0.94(11)	–	0.91(10)	–	0.860(60)	–
A_1^-	1.055(59)	0.53	1.025(51)	2.16	0.890(90)	–
A_1^{-*}	0.900(90)	–	1.32(17)	–	1.32(16)	–
A_2^+	1.500(50)	–	1.480(70)	–	1.410(80)	–
A_2^-	1.980(90)	–	1.67(15)	–	1.690(70)	–
E^+	1.010(40)	–	0.957(77)	1.94	0.870(50)	–
E^-	1.310(60)	–	1.220(50)	–	1.168(36)	2.59
T_1^+	1.590(90)	–	1.41(16)	1.36	1.480(90)	–
T_1^-	1.750(80)	–	1.60(10)	–	1.45(15)	–
T_2^+	1.028(15)	2.08	0.946(41)	0.98	0.863(49)	0.67
T_2^-	1.310(40)	–	1.200(60)	–	1.160(60)	–
String Tension	$a^2\sigma_s$	χ^2/d.o.f.	$a^2\sigma_s$	χ^2/d.o.f.	$a^2\sigma_s$	χ^2/d.o.f.
	0.04362(61)	–	0.03644(56)	–	0.03384(56)	–

Table 3.16: $Sp(8)$ glueball masses and string tensions. The measurements are expressed in the form "$m(\delta m)$" where m is the measured mass of the glueball in units of inverse lattice-spacing and δm is the statistical error in the measurement.

R^P \ $(L/a, \beta)$	$(18, 27.6)$		$(20, 27.9)$		$(22, 28.3)$	
	$am(R^P)$	χ^2/d.o.f.	$am(R^P)$	χ^2/d.o.f.	$am(R^P)$	χ^2/d.o.f.
A_1^+	0.530(20)	–	0.486(18)	–	0.440(10)	–
A_1^{+*}	0.760(50)	–	1.27(15)	–	0.910(50)	–
A_1^-	0.890(30)	–	0.769(33)	1.79	0.680(70)	–
A_1^{-*}	1.30(12)	–	1.11(14)	–	1.050(90)	–
A_2^+	1.230(90)	–	1.164(84)	1.3	0.940(80)	–
A_2^-	1.45(10)	–	1.23(12)	–	1.14(11)	–
E^+	0.839(27)	0.41	0.690(60)	–	0.634(35)	1.78
E^-	1.030(60)	–	0.983(57)	0.94	0.850(60)	–
T_1^+	1.290(90)	–	1.230(50)	–	1.020(80)	–
T_1^-	1.48(15)	–	1.33(10)	–	1.220(90)	–
T_2^+	0.815(26)	1.84	0.700(50)	–	0.641(22)	0.64
T_2^-	1.100(90)	–	0.972(63)	1.97	0.849(38)	2.91
String Tension	$a^2\sigma_s$	χ^2/d.o.f.	$a^2\sigma_s$	χ^2/d.o.f.	$a^2\sigma_s$	χ^2/d.o.f.
	0.02728(48)	–	0.02303(54)	–	0.01869(50)	–

Table 3.17: $Sp(8)$ glueball masses and string tensions. The measurements are expressed in the form "$m(\delta m)$" where m is the measured mass of the glueball in units of inverse lattice-spacing and δm is the statistical error in the measurement.

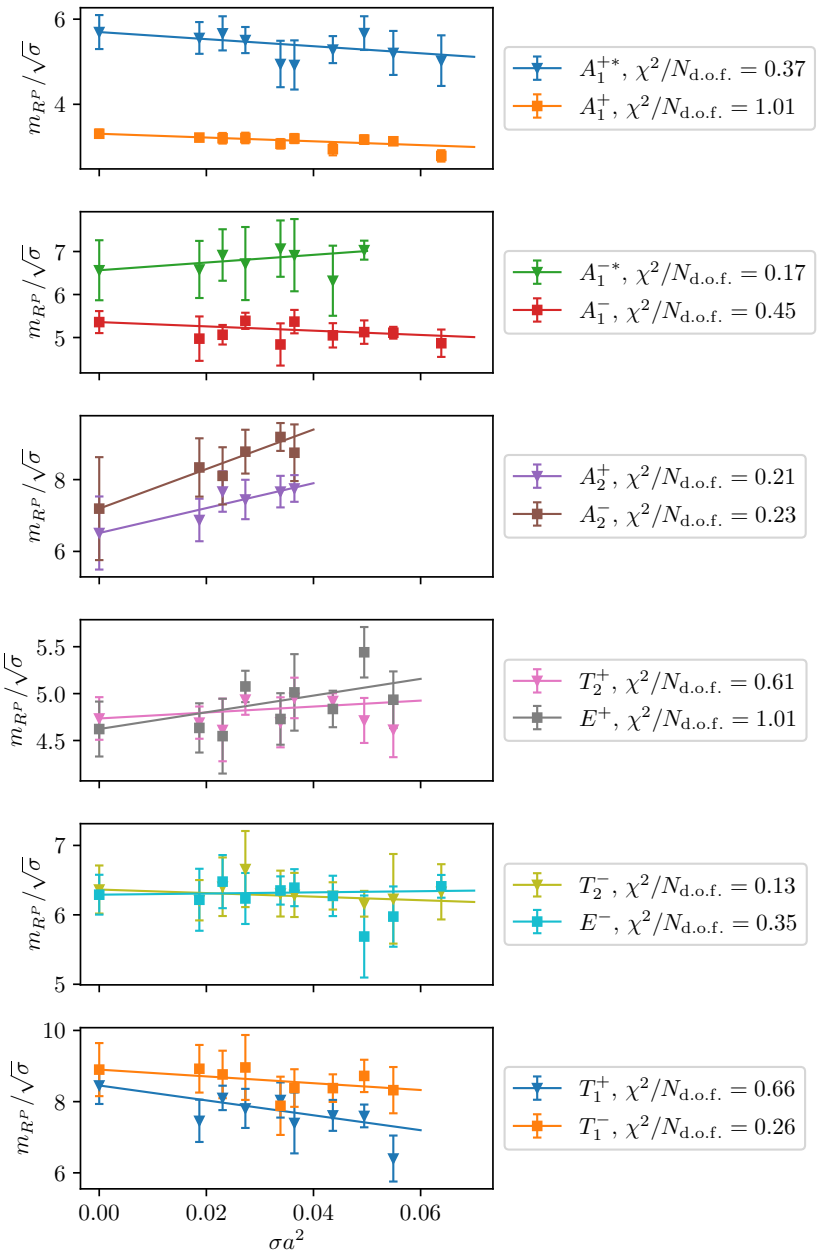

Figure 3.6: Lattice glueball masses and their continuum limit extrapolations for the gauge group $Sp(2N)$ at $N = 4$. The values plotted at $a^2\sigma$=0 are the continuum limits. Note the emergence of degeneracies between the T_2 and E states of matching parity.

$m(R^P)/\sqrt{\sigma}$						
R^P \ Group	$Sp(2)$	$Sp(4)$	$Sp(6)$	$Sp(8)$	$Sp(\infty)$	$SU(\infty)$
A_1^+	3.841(84)	3.577(49)	3.430(75)	3.308(98)	3.241(88)	3.307(53)
A_1^{+*}	5.22(33)	6.049(40)	5.63(32)	5.58(44)	6.29(33)	6.07(17)
A_1^-	6.20(14)	5.69(16)	5.22(23)	5.36(26)	5.00(22)	–
A_1^{-*}	7.37(72)	7.809(79)	6.59(49)	7.76(85)	7.31(45)	–
A_2^+	6.81(31)	7.91(16)	7.36(39)	6.5(1.0)	8.22(46)	–
A_2^-	8.99(86)	9.30(38)	8.60(67)	7.2(1.4)	8.69(83)	–
E^+	5.33(18)	5.05(13)	5.03(13)	4.62(29)	4.79(19)	4.80(14)
E^-	6.61(37)	6.65(12)	6.34(40)	6.29(29)	6.44(33)	–
T_1^+	8.58(41)	8.67(28)	7.77(59)	8.45(52)	8.33(51)	–
T_1^-	9.63(77)	9.24(33)	9.15(69)	8.90(75)	8.76(72)	–
T_2^+	5.29(20)	5.050(88)	5.09(16)	4.73(23)	4.80(20)	–
T_2^-	6.55(34)	6.879(88)	6.47(43)	6.36(35)	6.71(35)	–

Table 3.18: Continuum $Sp(2N)$ glueball masses in units of the square root of string tension and their large-N extrapolations. The $SU(\infty)$ results are obtained from [67]. Measurements are expressed in the form "$m(\delta m)$" where m is the glueball mass in units of the square-root of the string tension and δm is the statistical error in the measurement.

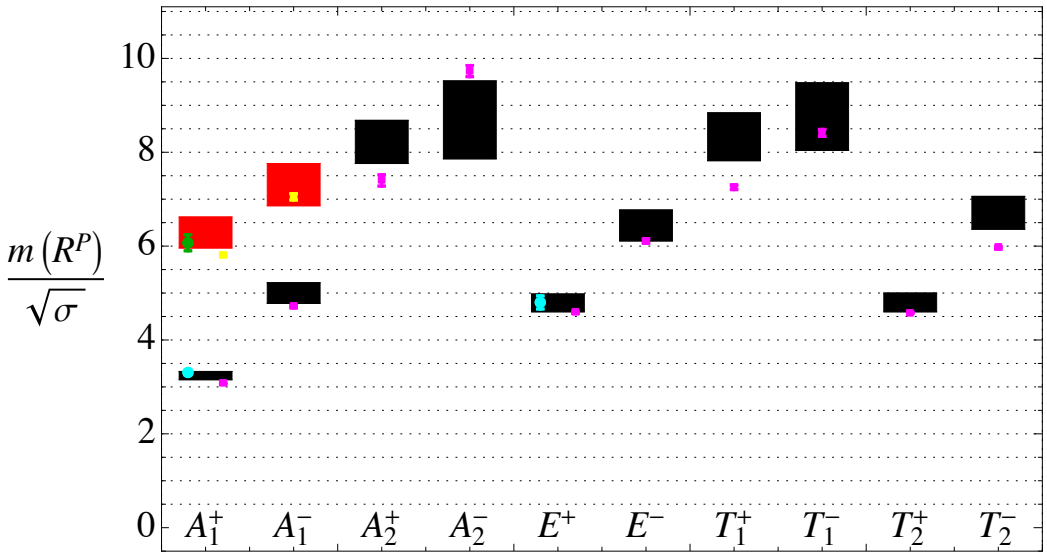

Figure 3.7: Glueball masses in the large-N limit expressed in units of $\sqrt{\sigma}$. Dots denote $SU(N)$ masses in the large-N limit from [67] and squares denote $SU(N)$ masses in the same limit from [78]. The vertical lines correspond to the statistical error of the measurement. The cyan dots and magenta squares denote ground states; green dots and yellow squares denote first excitations. Boxes denote $Sp(2N)$ masses in the large-N limit with their vertical thickness corresponding to the statistical error in the measurement. The black boxes denote ground states and the red boxes denote first excitations. A discussion of these results is contained in section 3.9.

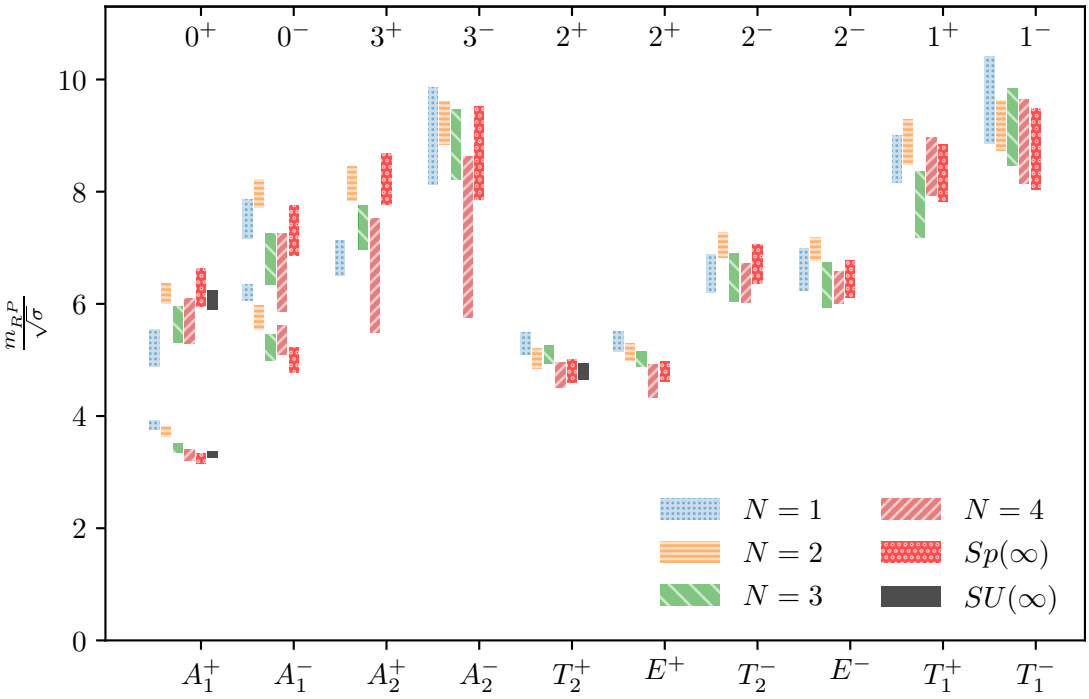

Figure 3.8: Continuum glueball masses in units of $\sqrt{\sigma}$ for $Sp(2N)$ at $N = 1$, 2, 3, 4 and ∞ as shown in [14]. The $SU(\infty)$ data is taken from [67]. The bottom x-axis states the representation of the octahedral group and the top x-axis is the corresponding spin and parity in the continuum.

N_c	$SU(N_c)$			$Sp(N_c)$		
	$\frac{m^2_{0^{++}}}{\sigma}$	$\frac{C_2(F)}{C_2(A)}$	$\eta(0^{++})$	$\frac{m^2_{0^{++}}}{\sigma}$	$\frac{C_2(F)}{C_2(A)}$	$\eta(0^{++})$
2	14.3(5)	3/8	5.36(20)	14.75(65)	3/8	5.53(24)
3	12.6(5)	4/9	5.60(22)	–	–	–
4	11.3(4)	15/32	5.29(19)	12.79(35)	5/12	5.33(15)
6	10.56(7)	35/72	5.135(35)	11.76(51)	7/16	5.15(22)
8	12.6(6)	63/128	6.20(31)	10.94(65)	9/20	4.92(29)
∞	10.94(35)	1/2	5.47(18)	10.50(57)	1/2	5.25(29)

Table 3.19: Ratio of the squared mass of the scalar glueball and string tension for $SU(N_c)$; the ratio of the quadratic Casimir operators and the corresponding value of their product, denoted by $\eta(0^{++})$ as in eq. (3.7.1). The $SU(N_c)$ masses are computed from the values of Table 14 in [67] and the $Sp(N_c)$ masses from table 3.18. The ratio of the fundamental- and adjoint-Casimirs are computed from eq. (3.7.2).

is constant for a given number of spacetime dimensions. In table 3.19 the data for $SU(N_c)$ and $Sp(N_c)$ are displayed.

3.9 Discussion

One of the first tests of the results in this chapter is comparing the data for $Sp(2)$ carried out in this thesis with results already in the literature for $SU(2)$. Since the two groups are the same, the numerical results should be compatible. It was to allow for comparison that we used the same values for β and L for the group $Sp(2)$ as were used in [67]. New results for the $SU(N)$ glueball spectrum both for finite N and for $N \to \infty$ were published in [78] after the computations were completed for the spectrum in $Sp(2N)$ and we tabulate these new results in this section. The results for large N have been added to fig. 3.7 which was originally presented before the publication of [78]. When compared with $Sp(2N)$ results, $SU(N)$ glueball masses quoted in this section

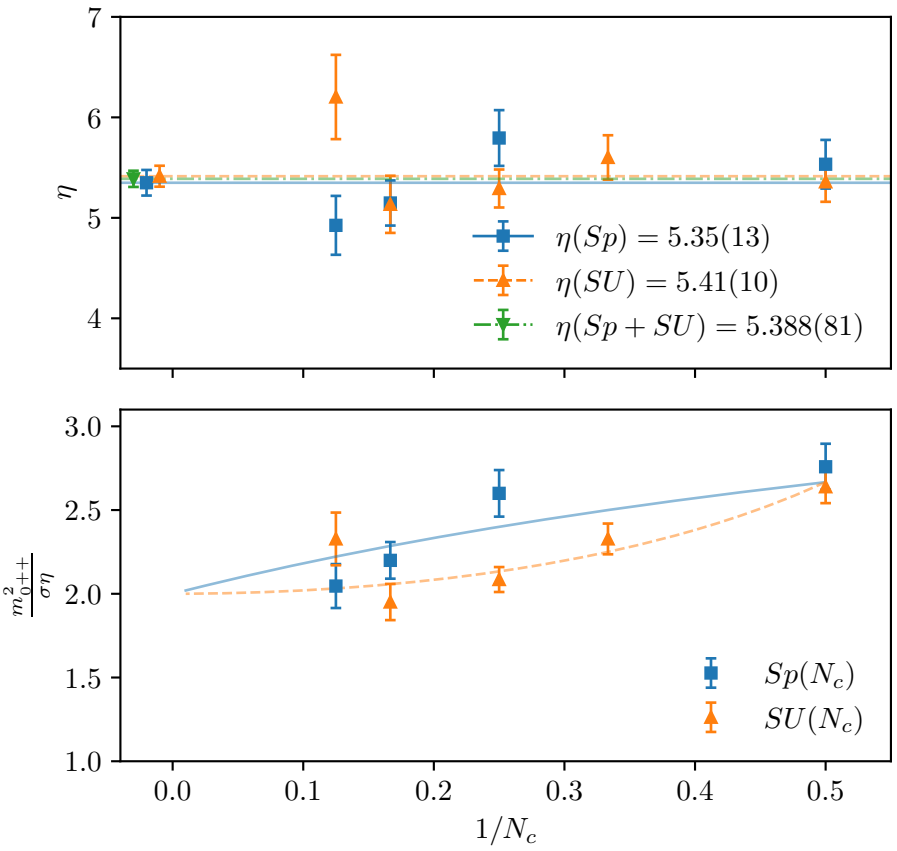

Figure 3.9: Top panel: The values of η plotted for both $SU(N_c)$ and $Sp(N_c)$ as defined in eq. (3.7.1). The fitted values of η from each set of data as well as the two in combination are stated in the plot.
Bottom panel: The quantity $m_{0^{++}}^2/\sigma$ divided by the conjectured universality constant η. The curves plotted are the quadratic Casimir in the adjoint representation divided by the quadratic Casimir in the fundamental representation for $SU(N_c)$ and $Sp(N_c)$. If the hypothesis of Casimir scaling is correct, we expect the data to fit the curve as, indeed, it does.

have positive charge conjugation since the negative states do not exist in the $Sp(2N)$ theories.

We first compare the results for the string tensions in each group. Our results for $Sp(2)$ are less precise than those for $SU(2)$ in [67] despite the latter being computed more than 15 years ago. Our results are, however, sufficiently precise for the purposes of our calculations.

L/a	β	$a\sqrt{\sigma}$	
		$Sp(2)$	$SU(2)$
10	2.2986	0.3583(73)	0.3667(18)
12	2.3726	0.2713(57)	0.2879(10)
16	2.4265	0.2379(21)	0.2388(9)
20	2.5115	0.1765(18)	0.1768(8)

Table 3.20: Square-root of string tension in units of inverse lattice spacing ($a\sqrt{\sigma}$) for $Sp(2)$ [14] compared with string tensions measured for $SU(2)$ in [67].

We also compare the glueball masses between the two groups. The results for the A_1^+ and E^+ glueball masses in the continuum limit are compatible but there is a a difference of more than one standard-deviation for the state A_1^{+*}. We ascribe this discrepancy to statistical fluctuations.

Group / R^P	$SU(2)$	$Sp(2)$
A_1^+	3.78(7)	3.841(84)
A_1^{+*}	6.46(14)	5.22(33)
E^+	5.45(11)	5.33(18)

Table 3.21: $SU(2)$ and $Sp(2)$ glueball masses in the continuum limit. The $SU(2)$ results are taken from [67] and the $Sp(2)$ results are given in full in table 3.18. All $SU(2)$ measurements have positive charge conjugation.

When computing the glueball spectrum at specific β and N values, the glueball masses for the E and T_2 channels of matching parity should be degenerate for reasons

explained in section 3.4. As we see in fig. 3.8, a mass degeneracy does indeed emerge within the pairs (E^+, T_2^+) and (E^-, T_2^-) for finite N as well as in the large-N limit.

There is one more feature of the results that can be examined. In [79], the hypothesis that the following ratio holds for all Yang-Mills theories in $3+1$ dimensions:

$$R \equiv \frac{m(E^+)}{m(A_1^+)} = \sqrt{2}. \tag{3.9.1}$$

This is explored in detail in [80]. The veracity of this claim would point to some form of universality within Yang-Mills theories. The relevant results are shown in table 3.22.

Group	$\frac{m(A_1^{++})}{\sqrt{\sigma}}$	$\frac{m(E^{++})}{\sqrt{\sigma}}$	R	R^2
$Sp(2)$	3.841(84)	5.31(13)	1.383(46)	1.91(13)
$Sp(4)$	3.729(89)	5.09(12)	1.366(45)	1.87(12)
$Sp(6)$	3.430(75)	5.05(10)	1.473(43)	2.17(13)
$Sp(8)$	3.308(98)	4.69(18)	1.417(69)	2.01(20)
$Sp(\infty)$	3.241(88)	4.80(14)	1.480(58)	2.19(17)
$SU(\infty)$[67]	3.307(53)	4.80(14)	1.451(48)	2.11(14)
$SU(\infty)$[78]	3.072(14)	4.582(14)	1.492(08)	2.225(24)

Table 3.22: Continuum glueball masses for the A_1^{++} and E^{++} channels. Also included is the ratio R as defined in eq. (3.9.1). Results are given for $Sp(2N)$ for $N = 1, 2, 3, 4$ and ∞. Also included is the same ratio for $SU(\infty)$ cited from [67] and from [78].

We see from table 3.22 that the values for R are in good agreement with the value $\sqrt{2}$. As well as the ratio R, the results are consistent with Casimir scaling described in section 3.7 (also examined in [80]).

The general agreement between $Sp(N_c)$ and $SU(N_c)$ groups for $N_c = 2$ and $N_c = \infty$ gives us confidence that our results are valid and also provides more numerical evidence for large-N universality. We compare our results for $Sp(N_c)$ with results for $SU(N_c)$ for $N_c = 2$ in table 3.23 and $N_c = \infty$ in table 3.24. Only the A_1^{+*}, A_2^+ and T_2^- channels differ by more than one sigma but, again, we would anticipate statistical

fluctuations of this type to arise.

Group / R^P	$Sp(2)$	$SU(2)$[67]	$SU(2)$[78]
A_1^+	3.841(84)	3.78(7)	3.781(23)
A_1^{+*}	5.22(33)	6.46(14)	6.126(38)
A_1^-	6.20(14)	–	6.017(61)
A_1^{-*}	7.37(72)	–	8.00(15)
A_2^+	6.81(31)	–	7.77(18)
A_2^-	8.99(86)	–	9.50(18)
E^+	5.33(18)	5.45(11)	5.343(30)
E^-	6.61(37)	–	7.037(67)
T_1^+	8.58(41)	–	8.14(10)
T_1^-	9.63(77)	–	9.06(13)
T_2^+	5.29(20)	–	5.353(23)
T_2^-	6.55(34)	–	6.997(65)

Table 3.23: Comparison of our continuum glueball masses for $Sp(2)$ with $SU(2)$ results both from [67] and [78] where results are available.

One obvious but important remark is that the work carried out in this chapter on string tension confirms that $Sp(2N)$ Yang-Mills theories confine. The same results were published in [14] and were the first instance of the phenomenon being confirmed for the symplectic groups, generally.

The additional evidence for the hypothesis of Casimir scaling as well as the consistency of the ratio R in eq. (3.9.1) seems to point towards some form of universality within Yang-Mills theories in a given number of dimensions. Since such theories cannot yet be solved analytically, a universal value or feature will be a useful landmark for their study.

Group / R^P	$Sp(\infty)$	$SU(\infty)$[67]	$SU(\infty)$[78]
A_1^+	3.241(88)	3.307(58)	3.072(14)
A_1^{+*}	6.29(33)	6.07(17)	5.805(31)
A_1^-	5.00(22)	–	4.711(25)
A_1^{-*}	7.31(45)	–	7.050(68)
A_2^+	8.22(46)	–	7.40(12)
A_2^-	8.69(83)	–	9.73(12)
E^+	4.79(19)	4.80(14)	4.582(14)
E^-	6.44(33)	–	6.108(44)
T_1^+	8.33(51)	–	7.250(47)
T_1^-	8.76(72)	–	8.412(76)
T_2^+	4.80(20)	–	4.578(11)
T_2^-	6.71(35)	–	5.965(28)

Table 3.24: Comparison of our continuum glueball masses for $Sp(\infty)$ with $SU(\infty)$ results both from [67] and [78].

Chapter 4

Quenched Mesons

We demonstrated in Chapter 3 that pure $Sp(2N)$ Yang-Mills can yield a rich spectrum of particles. Using $Sp(2N)$ to explain Higgs compositeness requires the addition of fermions. In Minkowski spacetime, the dynamics of fermions are governed by the Dirac equation. When we shift to Euclidean time on the lattice, the Dirac matrices change with it. The Clifford algebra obeyed by the Dirac matrices is

$$\{\gamma_M^\mu, \gamma_M^\nu\} = 2\eta^{\mu\nu}\mathbb{1}_4 \quad \text{in Minkowski spacetime,} \tag{4.0.1}$$

where $\eta^{\mu\nu}$ is the Minkowski metric and $\{A, B\} = AB + BA$ is the anticommutator of A and B. In Euclidean spacetime, the metric is simply the 4×4 identity matrix.

$$\{\gamma_E^\mu, \gamma_E^\nu\} = 2\delta^{\mu\nu}\mathbb{1}_4 \quad \text{in Euclidean spacetime.} \tag{4.0.2}$$

A simple way to make the Dirac matrices obey this new relationship is to make the transformations

$$\gamma_E^k = i\gamma_M^k \quad \text{for } k = 1, 2, 3 \tag{4.0.3}$$

$$\gamma_E^4 = \gamma_M^0 \tag{4.0.4}$$

The Dirac matrices in Euclidean spacetime are, therefore,

$$\gamma_E^1 = \begin{bmatrix} 0 & 0 & 0 & -i \\ 0 & 0 & -i & 0 \\ 0 & i & 0 & 0 \\ i & 0 & 0 & 0 \end{bmatrix} \quad \gamma_E^2 = \begin{bmatrix} 0 & 0 & 0 & -1 \\ 0 & 0 & 1 & 0 \\ 0 & 1 & 0 & 0 \\ -1 & 0 & 0 & 0 \end{bmatrix}$$

$$\gamma_E^3 = \begin{bmatrix} 0 & 0 & -i & 0 \\ 0 & 0 & 0 & i \\ i & 0 & 0 & 0 \\ 0 & -i & 0 & 0 \end{bmatrix} \quad \gamma_E^4 = \begin{bmatrix} 0 & 0 & 1 & 0 \\ 0 & 0 & 0 & 1 \\ 1 & 0 & 0 & 0 \\ 0 & 1 & 0 & 0 \end{bmatrix}. \tag{4.0.5}$$

The fifth gamma matrix, in Minkowski spacetime, is defined as

$$\gamma_M^5 = i\gamma_M^0\gamma_M^1\gamma_M^2\gamma_M^3. \tag{4.0.6}$$

When we shift to Euclidean spacetime

$$\gamma_E^5 = \gamma_E^1\gamma_E^2\gamma_E^3\gamma_E^4 \tag{4.0.7}$$

$$\gamma_E^5 = \begin{bmatrix} 1 & 0 & 0 & 0 \\ 0 & 1 & 0 & 0 \\ 0 & 0 & -1 & 0 \\ 0 & 0 & 0 & -1 \end{bmatrix}. \tag{4.0.8}$$

Hereafter, all Dirac matrices are in Euclidean spacetime and the subscript $_E$ will be left implicit.

The Dirac equation must be modified for its implementation on the lattice. The Euclidean-Dirac action for fermions in the continuum takes the form

$$S_{\text{cont}}\left[\psi, \overline{\psi}, A\right] = \int \mathrm{d}^4x\, \overline{\psi}(x)(\gamma_\mu(\partial_\mu + iA_\mu) + m)\psi(x) \tag{4.0.9}$$

and its discrete equivalent is [64]

$$S\left[\psi, \overline{\psi}, U\right] = a^4 \sum_{x\in\Lambda^4} \overline{\psi}(x) \left(\sum_{\mu=1}^{4} \gamma_\mu \frac{U_\mu(x)\psi(x+\hat{\mu}) - U_\mu^\dagger(x-\hat{\mu})\psi(x-\hat{\mu})}{2a} + m\psi(x) \right), \tag{4.0.10}$$

where $\overline{\psi}(x) \equiv \psi^\dagger(x)\gamma_4$ having shifted to Euclidean space.

The implementation of fermions on the lattice is not straight forward. If we take the naïve discretisation of the Dirac equation, we confront the problem of "fermion doubling": for each fermion in the continuum, there exist 2^d fermions on the lattice where d is the number of spacetime dimensions. The additional $2^d - 1$ fermions are known as "doublers". In addition, the Nielsen-Ninomiya Theorem (NNT) (first described in [81]) states that the following four conditions cannot be simultaneously fulfilled:

1. The lattice action is local;

2. The lattice action produces the correct classical continuum limit;

3. The lattice contains no doublers;

4. The lattice action obeys chiral symmetry.

Different methods exist for placing fermions on the lattice each of which sacrifices one or more of the conditions contained in the NNT. The method we use in this thesis is that of Wilson fermions which break chiral symmetry. The term in eq. (4.0.11) is added to the fermion part of the action which gives mass to the doublers; this extra mass diverges in the continuum limit causing the spurious fermions to decouple from the dynamics of the theory.

$$S_{\text{doublers}} = -\frac{a^3}{2}\sum_{x\in\Lambda^4}\sum_{\mu=1}^{4}\left(\overline{\psi}(x)U_\mu(x)\psi(x+\hat{\mu}) - 2\overline{\psi}(x)\psi(x) + \overline{\psi}(x)U_\mu^\dagger(x-\hat{\mu})\psi(x-\hat{\mu})\right) \tag{4.0.11}$$

As stated at the beginning of Chapter 1, the models for composite Higgs require two fundamental flavours of fermions. The results for the meson spectrum in this chapter are carried out in the quenched approximation which apply to a generic number of flavours. This provides a first necessary step towards the study of the phenomenologically interesting model.

In section 4.1 we describe the computation of meson correlators and how to extract observable quantities from them. Such observables are meson masses and their decay constants. The methodology involves finding a plateau in the effective mass and fitting a curve to the data points in this region. This is very similar to the extraction of glueball masses detailed in section 3.2. In section 4.2, we describe the renormalisation of decay constants from lattice data as well as the elimination of tadpole diagrams. The extrapolation of lattice data to the continuum- and chiral-limits is described in section 4.3 as well as the method of scale setting via the gradient flow method. The

Label	Interpolating Operator $\mathcal{O}_S$	J^P	QCD meson
PS	$\overline{\psi^i}\gamma^5\psi^j$	0^-	π
S	$\overline{\psi^i}\psi^j = \overline{\psi^i}\mathbb{1}\psi^j$	0^+	a_0
V	$\overline{\psi^i}\gamma^\mu\psi^j$	1^-	ρ
AV	$\overline{\psi^i}\gamma^5\gamma^\mu\psi^j$	1^+	a_1
T	$\overline{\psi^i}\gamma^0\gamma^\mu\psi^j$	1^-	ρ
AT	$\overline{\psi^i}\gamma^5\gamma^0\gamma^\mu\psi^j$	1^+	b_1

Table 4.1: The operators used to construct meson states. A fermion of flavour i is described by the Dirac spinor ψ^i and its corresponding adjoint spinor is $\overline{\psi^i} \equiv \psi^{i\dagger}\gamma^4$. The meson produced by the corresponding operator in QCD is included for concreteness.

handling of statistical errors in the lattice data is outlined in section 4.4. Our lattice results are plotted and tabulated in section 4.5 with concluding remarks in section 4.6.

4.1 Meson Masses and Decay-Constants

The method of measuring the mass spectrum of mesons is similar, operationally, to measuring the glueball mass spectrum described in Chapter 3. The difference is that the operators involve combinations of fermion spinors and Dirac gamma matrices as opposed to path-ordered products of link variables. As with glueballs, the operators create a meson with specific spin (J) and parity (P). If ψ^i is a Dirac spinor of flavour i and $\overline{\psi^i} \equiv \psi^{i\dagger}\gamma_4$ is the corresponding adjoint spinor (in Euclidean spacetime) then the interpolating operators $\mathcal{O}_S$ can be constructed as in table 4.1.

The fermion calculations in this thesis are carried out in the *quenched approximation*. The spin-statistics theorem tells us that the wave function for identical fermions is antisymmetric under the exchange of two fermions. This is reflected in the path-integral formulation of QFT by treating the fermion fields as Grassmann (anticommuting) numbers. These manifest themselves in the path-integral as a matrix determinant

via a generalisation of the Matthews-Salam formula:

$$\int \prod_{i=1}^{N} \mathrm{d}\overline{\eta}_i \, \mathrm{d}\eta_i \, \exp\left(\sum_{j,k=1}^{N} \overline{\eta}_j M_{jk} \eta_k \right) = \det(M), \tag{4.1.1}$$

where $\{\eta_i\}$ are Grassmann numbers.

Following the method of [64], the (Euclidean) path integral to be evaluated on the lattice is

$$Z = \int \mathcal{D}U \, e^{-S_G[U]} \mathcal{D}\overline{\psi} \mathcal{D}\psi \, e^{-S_F[\psi, \overline{\psi}, U]} \tag{4.1.2}$$

where S_G is the pure gauge part of the action and S_F is the fermionic part of the action as well as the interactions between the fermions and the gauge field.

The fermionic part of the action – eq. (4.0.10) – can be written in terms of a Dirac operator, D:

$$S_F[\psi, \overline{\psi}, U] = a^4 \sum_{f=1}^{N_f} \sum_{x,y \in \Lambda} \overline{\psi^f}(x) D(x-y) \psi^f(y) \tag{4.1.3}$$

and, hence, the fermionic section of the partition function is reduced to the computation of the matrix determinant $\det(D)^{N_f}$ where N_f is the number of fermion flavours. The summation over all flavours occurs within the exponent of e^{-S} and thus raises the determinant to the power N_f.

In a gauge theory with N_c charges, $|\Lambda|$ lattice sites and fermions each with $2s+1$ possible spin states, the matrix whose determinant is to be computed has $2N_c(2s+1)|\Lambda|$ rows and columns where the additional factor of two comes from the antiparticle of the fermion. To say that the problem has been "reduced" to the computation of a matrix determinant is to gloss over one of the greatest difficulties in lattice theory. Although the computation of a determinant is easy to understand, the tremendous

size of the matrix makes it a very expensive task computationally. In the quenched approximation, this very large matrix has its determinant set equal to 1. Physically, this amounts to neglecting fermion loops and having hadrons composed solely of valence quarks as opposed to valence and sea quarks. In the early days of lattice theory, the quenched approximation was more or less a necessity but increased computational power has allowed us to carry out such computations with dynamical fermions. In this thesis, however, we restrict our attention to quenched fermions since they are less computationally expensive and are sufficient for an initial exploration of the meson spectrum.

The general form for the computation of the meson correlators is

$$\langle \mathcal{O}(x)\overline{\mathcal{O}}(y)\rangle = \frac{1}{Z}\int \mathcal{D}U\, e^{-S_G[U]}\mathcal{D}\overline{\psi}\mathcal{D}\psi\, e^{-S_F[\psi,\overline{\psi},U]}\mathcal{O}(x)\overline{\mathcal{O}}(y) \tag{4.1.4}$$

where Z is the partition function in eq. (4.1.2) and $\mathcal{O}$ is the relevant operator from table 4.1. Both Z and the explicit integral in eq. (4.1.4) can have their respective fermionic parts rewritten as functions of the operator $D(x-y)$ in eq. (4.1.3):

$$Z = \int \mathcal{D}U\, e^{-S_G[U]}\det(D)^{N_f} \tag{4.1.5}$$

$$\langle \mathcal{O}(x)\overline{\mathcal{O}}(y)\rangle = \frac{1}{Z}\int \mathcal{D}U\, e^{-S_G[U]}F(D), \tag{4.1.6}$$

where $F(D)$ is a function of the Dirac operator D. In the quenched approximation, the determinant $\det(D)$ is set to 1 and the correlator reduces to

$$\langle \mathcal{O}(x)\overline{\mathcal{O}}(y)\rangle = \frac{\int \mathcal{D}U\, e^{-S_G[U]}F(D)}{\int \mathcal{D}U\, e^{-S_G[U]}}. \tag{4.1.7}$$

Thus, calculations in the quenched approximation are carried out over pure gauge

configurations and the number of flavours, N_f, is irrelevant.

The computation of eq. (4.1.7) on the lattice amounts to taking a trace of the product of the inverse of the Dirac operator, D, and the matrices of the relevant channel. We write a generic operator as $\mathcal{O}(x) = \overline{\psi^i}(x)\Gamma\psi^j(x)$ where i and j are flavour indices and Γ is a combination of the identity and gamma matrices that creates a meson with the relevant quantum numbers. Following the method of [64], the complex conjugate is

$$\begin{aligned}
\overline{\mathcal{O}}(x) &= \left(\overline{\psi^i}(x)\Gamma\psi^j(x)\right)^\dagger \\
\implies \overline{\mathcal{O}}(x) &= \left(\psi^{i\dagger}(x)\gamma_4\Gamma\psi^j(x)\right)^\dagger \\
\implies \overline{\mathcal{O}}(x) &= -\psi^{j\dagger}(x)\Gamma^\dagger\gamma_4\psi^i(x) \quad \text{(since the } \psi \text{ terms anticommute)} \\
\implies \overline{\mathcal{O}}(x) &= -\overline{\psi^j}(x)\gamma_4\Gamma^\dagger\gamma_4\psi^i(x) \quad \text{(since } \gamma_4^2 = \mathbb{1}\text{).}
\end{aligned} \tag{4.1.8}$$

Because the Γ term in eq. (4.1.8) is comprised of some combination of the five gamma matrices, all of which mutually anticommute and are hermitean, the hermitean conjugate of Γ will be equal to $\pm\Gamma$. The γ_4 matrices on either side of can be passed through the components of Γ which, again, cannot do more than change the sign since every component of Γ will either commute or anticommute with γ_4:

$$\gamma_4\Gamma^\dagger\gamma_4 = \pm\Gamma. \tag{4.1.9}$$

So the operator $\overline{\mathcal{O}}(x)$ can be written as

$$\overline{\mathcal{O}}(x) = \pm\overline{\psi^j}(x)\Gamma\psi^i(x). \tag{4.1.10}$$

Because we take ratios of the correlators to determine the effective mass of the meson as in eq. (4.1.22), the overall sign is irrelevant and we may drop it.

We can now write the full correlation function for an isotriplet meson (for which $i \neq j$) as

$$\begin{aligned}
\langle \overline{\mathcal{O}}(x)\mathcal{O}(y)\rangle &= \langle \overline{\psi^j}(x)\Gamma\psi^i(x)\overline{\psi^i}(y)\Gamma\psi^j(y)\rangle \\
\implies \langle \overline{\mathcal{O}}(x)\mathcal{O}(y)\rangle &= \langle \overline{\psi^j}_\alpha(x)\Gamma_{\alpha\beta}\psi^i_\beta(x)\overline{\psi^i}_\gamma(y)\Gamma_{\gamma\delta}\psi^j_\delta(y)\rangle \\
\implies \langle \overline{\mathcal{O}}(x)\mathcal{O}(y)\rangle &= \Gamma_{\alpha\beta}\Gamma_{\gamma\delta}\langle \overline{\psi^j}_\alpha(x)\psi^i_\beta(x)\overline{\psi^i}_\gamma(y)\psi^j_\delta(y)\rangle \\
\implies \langle \overline{\mathcal{O}}(x)\mathcal{O}(y)\rangle &= -\Gamma_{\alpha\beta}\Gamma_{\gamma\delta}\langle \psi^i_\beta(x)\overline{\psi^i}_\gamma(y)\psi^j_\delta(y)\overline{\psi^j}_\alpha(x)\rangle. \qquad (4.1.11)
\end{aligned}$$

Conservation of fermion flavour means that we can factorise the two flavours in eq. (4.1.11):

$$\begin{aligned}
\langle \overline{\mathcal{O}}(x)\mathcal{O}(y)\rangle &= -\Gamma_{\alpha\beta}\Gamma_{\gamma\delta}\langle \psi^i_\beta(x)\overline{\psi^i}_\gamma(y)\rangle\langle \psi^j_\delta(y)\overline{\psi^j}_\alpha(x)\rangle \\
\implies \langle \overline{\mathcal{O}}(x)\mathcal{O}(y)\rangle &= -\Gamma_{\alpha\beta}\Gamma_{\gamma\delta}D^{-1}_{i,\,\beta\gamma}(x-y)D^{-1}_{j,\,\delta\alpha}(y-x) \\
\implies \langle \overline{\mathcal{O}}(x)\mathcal{O}(y)\rangle &= -\Gamma_{\alpha\beta}D^{-1}_{i,\,\beta\gamma}(x-y)\Gamma_{\gamma\delta}D^{-1}_{j,\,\delta\alpha}(y-x) \\
\implies \langle \overline{\mathcal{O}}(x)\mathcal{O}(y)\rangle &= -\operatorname{tr}\left[\Gamma D_i^{-1}(x-y)\Gamma D_j^{-1}(y-x)\right], \qquad (4.1.12)
\end{aligned}$$

where D_i^{-1} is the inverse of the Dirac operator for flavour i. Equation (4.1.12) shows how the isotriplet correlator is computed from lattice configurations. Note that the formula only contains Dirac operators between two distinct spacetime coordinates (x and y). The isosinglet term ($i = j$) contains Dirac operators that start and end at the same coordinate. Such terms are computationally very expensive and we defer its examination to later studies.

We now explain how observables are computed from the correlator. The corre-

lator of two interpolating operators, $\mathcal{O}_M$ and $\mathcal{O}_{M'}$, at a given time t is defined as

$$C_{MM'}(t) = \sum_{\underline{x}} \langle 0|\mathcal{O}_M(\underline{x},t)\mathcal{O}^\dagger_{M'}(\underline{0},0)|0\rangle \,. \tag{4.1.13}$$

As $t \to \infty$, the decay of the correlator with $M = M'$ is governed by

$$C_M(t) \to \frac{|\,\langle 0|\mathcal{O}_M|M\rangle\,|^2}{m_M L^3}\left[e^{-m_M t} + e^{-m_M(T-t)}\right] \quad \text{as } t \to \infty \tag{4.1.14}$$

where $|M\rangle$ is the meson state, m_M is the meson mass and $L = aN_s$ is the physical extent of the lattice. We follow the same conventions as in [5,13] to compute the meson masses and, where appropriate, the decay-constants, f_M.

The matrix elements are parameterised in a similar way as in the pion current in section 1.2.2:

$$\langle 0|\overline{\psi^i}\gamma^5\gamma^\mu\psi^j|PS\rangle = f_{PS}p^\mu, \tag{4.1.15}$$

$$\langle 0|\overline{\psi^i}\gamma^\mu\psi^j|V\rangle = f_V m_V \epsilon^\mu, \tag{4.1.16}$$

$$\langle 0|\overline{\psi^i}\gamma^5\gamma^\mu\psi^j|AV\rangle = f_{AV} m_{AV} \epsilon^\mu. \tag{4.1.17}$$

The flavour indices, i and j, correspond to the fermion flavours comprising the meson. The term ϵ^μ is the polarisation vector which obeys $\epsilon^\mu p_\mu = 0$ and $\epsilon^\mu \epsilon_\mu = 1$. Substituting the second and third of the above equations into eq. (4.1.14) gives us, respectively,

$$C_V(t) \to \frac{f_V^2 m_V}{L^3}\left[e^{-m_V t} + e^{-m_V(T-t)}\right], \tag{4.1.18}$$

$$C_{AV}(t) \to \frac{f_{AV}^2 m_{AV}}{L^3}\left[e^{-m_{AV} t} + e^{-m_{AV}(T-t)}\right]. \tag{4.1.19}$$

In order to compute f_{PS}, we have to consider one additional correlation function:

$$C_{AV,PS}(t) = \sum_{\underline{x}} \langle 0| \left(\overline{\psi}^i \gamma^5 \gamma^\mu \psi^j(\underline{x}, t) \right) \left(\overline{\psi}^i \gamma^5 \psi^j(\underline{0}, 0) \right) |0\rangle \,, \tag{4.1.20}$$

$$C_{AV,PS}(t) \to \frac{f_{PS} \langle 0|\mathcal{O}_{PS}|PS\rangle^*}{L^3} \left[e^{-m_{PS} t} - e^{-m_{PS}(T-t)} \right] . \tag{4.1.21}$$

The mass and decay-constant of the pseudoscalar meson can be determined by simultaneous curve-fitting to eqs. (4.1.14) and (4.1.21) with $M = PS$. The masses and decay-constants for both the vector and axial-vector mesons are computed by fitting the correlator to eqs. (4.1.18) and (4.1.19), respectively. The masses of each of the remaining three channels (scalar, tensor and axial-tensor) are computed from eq. (4.1.14) with $\mathcal{O}_M$ substituted from table 4.1. The curve-fitting is not carried out for all available times, t, since eqs. (4.1.14) and (4.1.18) to (4.1.20) only hold at large Euclidean times. The effective mass as a function of Euclidean time from the relevant correlator $C(t)$ is

$$am_{\text{eff}}(t) = \operatorname{arccosh} \left[\frac{C(t-1) + C(t+1)}{2C(t)} \right] . \tag{4.1.22}$$

The qualitative approach is to look for the t-interval, $[t_1, t_2]$, for which $am_{\text{eff}}(t)$ exhibits a plateau. At this stage, we can say with confidence that the correlator closely resembles its large-time formula. Nonetheless, simply looking for a plateau by eye is prone to errors and cannot be reliably reproduced by third parties. In Appendix C we describe an algorithm for the determination of the time interval $[t_1, t_2]$. The method allows for a great deal of the work to be done automatically and in a reproducible manner, as well as being a rich topic for a student of machine learning. Some of the curve-fitting intervals (particularly for the heavy states such as the axial-vector and axial-tensor) do have to be selected manually.

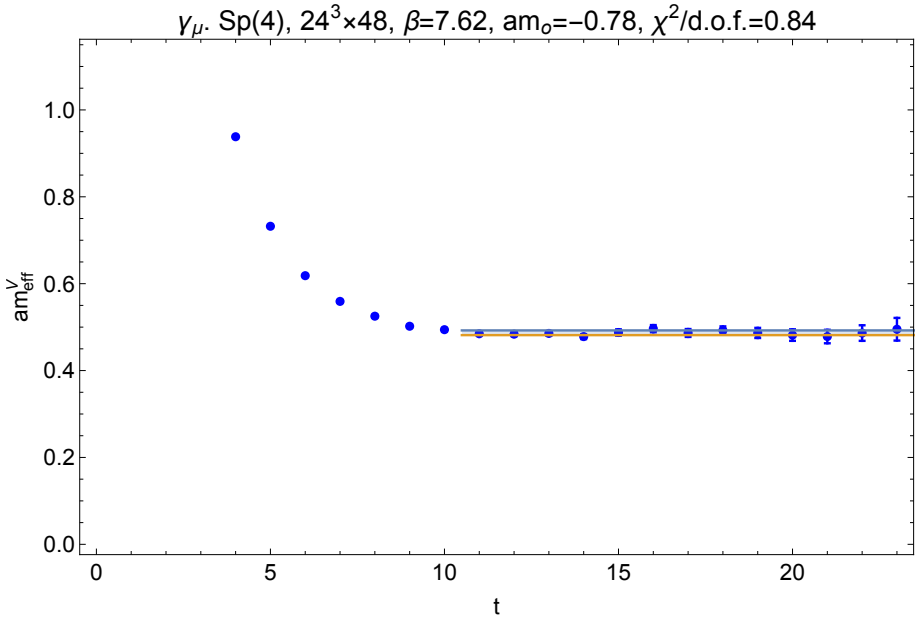

Figure 4.1: An example of a meson mass plateau. The effective mass of the meson is plotted against Euclidean time. The state is the vector meson comprised of fermions in the fundamental representation of $Sp(4)$ at $\beta = 7.62$. The mass fit range is the horizontal length of the blue and orange lines with the vertical width corresponding to the statistical error in the measurement. The reduced chi-squared and bare mass are stated in the plot header.

An example of an effective mass plateau is shown in fig. 4.1. Such a plot was examined for each bare mass in each channel at each beta value in tables 4.5 to 4.16.

4.2 Renormalising Meson Observables

As mentioned earlier, throughout the meson calculations, we have used the quenched approximation. This is generally adopted to speed up numerical calculations by avoiding the computation of a large-matrix determinant. It has the effect of ignoring loops generated by virtual fermion-antifermion pairs. In spite of this, the observables will still acquire corrections due to gluon loops and will, thus, still require renormalisation.

R	$C_2(R)$
Fundamental	$(N_c+1)/4$
Antisymmetric	$N_c/2$
Adjoint	$N_c/2+1$
Symmetric	$N_c/2+1$

Table 4.2: The quadratic Casimir operators, $C_2(R)$, for different representations, R, of $Sp(N_c)$.

Δ_{Σ_1}	Δ_{γ_μ}	$\Delta_{\gamma_5\gamma_\mu}$
-12.82	-7.75	-3.0

Table 4.3: The Δ terms used in the renormalisation factors [82].

As demonstrated in [82], the renormalised decay-constants, f_M^{ren}, are related to their corresponding bare quantities, f_M^{bare}, by a multiplicative factor.

$$f_{PS}^{\text{ren}} = Z_A f_{PS}^{\text{bare}}, \tag{4.2.1}$$

$$f_{V}^{\text{ren}} = Z_V f_{V}^{\text{bare}}, \tag{4.2.2}$$

$$f_{AV}^{\text{ren}} = Z_A f_{AV}^{\text{bare}}. \tag{4.2.3}$$

The quantities Z_A and Z_V are given by [82]

$$Z_V = 1 + C_2(R)\left(\Delta_{\Sigma_1} + \Delta_{\gamma_\mu}\right)\frac{N_c}{8\pi^2\beta\langle P\rangle}, \tag{4.2.4}$$

$$Z_A = 1 + C_2(R)\left(\Delta_{\Sigma_1} + \Delta_{\gamma_5\gamma_\mu}\right)\frac{N_c}{8\pi^2\beta\langle P\rangle}. \tag{4.2.5}$$

The three Δ terms are pure numbers shown in table 4.3. The term N_c is that of $Sp(N_c)$; $C_2(R)$ is the quadratic Casimir operator for the representation R of $Sp(N_c)$ as stated in table 4.2; β is the inverse coupling and $\langle P\rangle$ is the average value of the plaquette operator as defined in table 1.

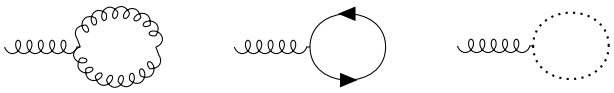

Figure 4.2: Tadpole diagrams in continuum Yang-Mills theory. Left to right: gluon-tadpole, fermion-tadpole, ghost-tadpole. The fermion diagram is not present in the quenched approximation but is included for completeness. The ghost diagram is not included in the lattice theory since there is no need for gauge fixing.

The purpose of the average plaquette value is to remove the effects of tadpole diagrams which vanish in the continuum. Tadpole diagrams (shown in fig. 4.2) have an effect on lattice calculations and these can be compensated for by the inclusion of the average plaquette. A naïve expansion parameter for the lattice is g, the coupling constant; however, as demonstrated in [83], we can compensate for the tadpole diagrams by replacing

$$\widetilde{g}^2 = \frac{g^2}{\langle P \rangle} \tag{4.2.6}$$

which is equivalent to

$$\widetilde{\beta} = \beta \langle P \rangle. \tag{4.2.7}$$

4.3 Chiral limit

Lattice computations of fermions often use unphysically large quark masses. The reason for this is that fermion observables become progressively more expensive to compute as the bare mass decreases. This has become known as the "Berlin Wall" after its formal discussion at the 2001 Lattice Conference in the same city. We can, however, extrapolate observable quantities to the chiral limit just as we extrapolated to the continuum limit in the computation of the glueball spectrum in section 3.6.2. The

method used in this thesis is chiral perturbation theory (χPT) for Wilson fermions, the same as in [13, 29]. By definition, the pseudoscalar meson is massless in the chiral limit in the same way that the pions of QCD become massless in the limit where chiral symmetry is not explicitly broken in the QCD Lagrangian as shown in section 1.2.

The next-to-leading order (NLO) expansions for masses and decay-constants in a given channel, M, in the chiral limit are given by

$$\hat{m}_{\mathrm{M}}^{2,\mathrm{NLO}} = \hat{m}_{\mathrm{M}}^{2,\chi}(1 + L_{m,\mathrm{M}}^{0}\hat{m}_{PS}^{2}) + W_{m,\mathrm{M}}^{0}\hat{a} \tag{4.3.1}$$

$$\hat{f}_{\mathrm{M}}^{2,\mathrm{NLO}} = \hat{f}_{\mathrm{M}}^{2,\chi}(1 + L_{f,\mathrm{M}}^{0}\hat{m}_{PS}^{2}) + W_{f,\mathrm{M}}^{0}\hat{a}. \tag{4.3.2}$$

The term $\hat{m}_{PS}^{2}$ is the squared mass of the pseudoscalar. The two formulae have the same form for both masses and decay-constants. All quantities are measured in units of gradient-flow as denoted by the caret ($\hat{}$) symbol. The L and W terms are parameters to be determined by curve-fitting. The $\hat{a}$ term is the inverse of the gradient-flow scale: $\hat{a} = a/w_o$.

The gradient flow scale, w_0, is used for comparing the scale of lattices at different values of β. It was introduced in [84] and is an improvement on the Wilson flow techniques originally proposed by Martin Lüscher in [85]. The method was applied to these same calculations in [13].

We introduce a new variable, $\mathbb{t}$, known as flow-time and a new field $B_\mu(\mathbb{t}, x)$. $B_\mu(\mathbb{t}, x)$ is defined in terms of the differential equation:

$$\frac{dB_\mu(\mathbb{t}, x)}{d\mathbb{t}} = D_\nu F_{\mu\nu}(\mathbb{t}, x), \quad B_\mu(\mathbb{t} = 0, x) = A_\mu(x). \tag{4.3.3}$$

The term $A_\mu(x)$ is the continuum gauge field and the covariant derivative, D_μ, is defined as $D_\mu\phi = \partial_\mu\phi + [B_\mu, \phi]$ with $F_{\mu\nu} = [D_\mu, D_\nu]$.

Shifting to the lattice, the gradient flow definitions in eq. (4.3.3) become

$$\frac{dV_\mu(\mathbb{t},x)}{d\mathbb{t}} = -g_o^2 \left(\partial_{x,\mu} S^{\text{flow}}[V_\mu]\right) V(\mathbb{t},x) \tag{4.3.4}$$

with $V_\mu(\mathbb{t}=0,x) = U_\mu(x)$ and $S^{\text{flow}}[V_\mu]$ is the Wilson action.

We define the average value of the continuum action density as a function of $\mathbb{t}$, as

$$\langle E(\mathbb{t})\rangle = \frac{1}{4} F^a_{\mu\nu}(\mathbb{t}) F^a_{\mu\nu}(\mathbb{t}) \tag{4.3.5}$$

and the related quantity

$$\mathcal{W}(\mathbb{t}) = \mathbb{t}\frac{d}{d\mathbb{t}}\left(\mathbb{t}^2\langle E(\mathbb{t})\rangle\right). \tag{4.3.6}$$

We choose a reference value $\mathcal{W}_0$ for all β's in a given $Sp(2N)$ group and define the gradient flow scale w_0 as

$$\mathcal{W}(\mathbb{t} = w_0^2) = \mathcal{W}_0. \tag{4.3.7}$$

In our calculations, we choose $\mathcal{W}_0$ to be fixed at 0.35, the same as in [13]. The quantity w_0/a is dimensionless as are the quantities am. Therefore, a dimensionless measurement that is independent of lattice spacing is $w_0 m$. Using units of gradient flow allows us to compare measurements obtained at different lattice spacings (β values). This method can also be used in the computation of the glueball spectrum. The values for w_0 used in our calculations are shown in table 4.4.

4.4 Handling of Statistical Errors

The correlators corresponding to a given meson state are computed for all lattice configurations. Each lattice configuration yields a correlator, $C(t)$ where t goes from 0 to $N_t/2$ since we take the average of $C(t)$ and $C(T-t)$ to account for propagation of

$\mathcal{W}_0(\mathbb{t} = w_0^2) = 0.35$		
Group	β	w_0/a
$Sp(4)$[13]	7.62	1.448(3)
	7.7	1.6070(19)
	7.85	1.944(3)
	8.0	2.3149(12)
	8.2	2.8812(21)
$Sp(6)$	15.6	1.2360(21)
	16.1	1.7012(30)
	16.5	2.1505(30)
	16.7	2.3566(44)
	17.1	2.9025(43)

Table 4.4: Gradient flow scales used in the chiral extrapolations. The values of w_0/a for $Sp(4)$ are those of table 2 in [13]. The values of w_0/a for $Sp(6)$ were computed especially for this thesis.

states backwards in time. We then bootstrap the correlators. In this work, we take 200 bootstrap samples (with replacement) at each t value with the average and standard deviation across the 200 samples being the value and error of $\overline{C}(t)$, respectively, at that value of t. The correlator at time t for bootstrap sample $\mathcal{S}$ is denoted by $C(t;\mathcal{S})$. From these bootstrapped correlators and their corresponding errors, we can compute the effective mass and its corresponding error at a given value of t.

The mass of the meson is computed by searching for a plateau in the plot of effective mass against Euclidean time. The time interval where this occurs can in many cases be reliably determined using the plateau seeking algorithm described in Appendix C. Once a fit range $[t_i,t_f]$ has been selected, we compute the covariance matrix, Cov_{ij}, via

$$\mathrm{Cov}_{ij} = \mathrm{E}\left[C(i;\mathcal{S}) - \overline{C}(i)\right] \times \mathrm{E}\left[C(j;\mathcal{S}) - \overline{C}(j)\right] \tag{4.4.1}$$

where $\mathrm{E}[x]$ denotes the quantity x averaged over all bootstrap samples. We need only compute the components of the covariance matrix for $t_i \leqslant i, j \leqslant t_f$.

If $f(\{a_n\}, t)$ is the curve fitting function with parameters $\{a_n\}$ at Euclidean time t, its optimal parameters are determined by minimising the value of χ^2:

$$\chi^2 = \sum_{i=t_1}^{t_2} \sum_{j=t_1}^{t_2} (\overline{C}(i) - f(\{a_n\}, i))(\mathrm{Cov}^{-1})_{ij}(\overline{C}(j) - f(\{a_n\}, j)). \tag{4.4.2}$$

This minimum value is the corresponding χ^2 of the curve-fitting procedure. We bootstrap the fit parameters by repeating the χ^2 minimisation as in eq. (4.4.2) but with the average correlator $\overline{C}(t)$ replaced with that of a single bootstrap sample $C(t; \mathcal{S})$. We use the same covariance matrix, the justification being that bootstrapping the bootstrap samples recovers the same result after a large number of iterations.

Because we carried out 200 bootstrap iterations, we now have 200 measurements for each of the parameters $\{a_n\}$. By the central limit theorem, these will follow a normal distribution. We can, thus, fit a histogram of the 200 measurements of each parameter to a normal distribution with the mean and width corresponding to the value and error, respectively, in each parameter.

4.5 Results

In this section we collate the results for the $Sp(4)$ and $Sp(6)$ meson spectra both in the quenched approximation. The results for $Sp(4)$ in the fundamental and antisymmetric representations use the same beta values and corresponding bare masses as [13] to allow for comparison. All other results are original to this thesis. As stated in section 4.1, we restrict our attention to isotriplet mesons (i.e. those whose total isospin is $I = 1$). The investigation of the more computationally expensive isosinglet states ($I = 0$) is

deferred to later studies. For each gauge group, the results are tabulated for fermions in the fundamental, antisymmetric and symmetric/adjoint representations (recall that the symmetric and adjoint representations are identical for $Sp(2N)$ groups). If no reliable signal was detected for a specific set of parameters, the entry in the table is marked with a "–" symbol. Errors are computed by the method laid out in section 4.4.

Data for $Sp(4)$ are contained in tables 4.5 and 4.6 for the fundamental representation; tables 4.7 and 4.8 for the antisymmetric representation; tables 4.9 and 4.10 for the symmetric representation. The $Sp(4)$ chiral extrapolations are shown in figs. 4.3 and 4.4 for decay constants and masses, respectively. Data for $Sp(6)$ are contained in tables 4.11 and 4.12 for the fundamental representation; tables 4.13 and 4.14 for the antisymmetric representation; tables 4.15 and 4.16 for the symmetric representation. The $Sp(6)$ chiral extrapolations are shown in figs. 4.9 and 4.10 for decay constants and masses, respectively. We compare our data for the chiral limit of $Sp(4)$ in the fundamental and antisymmetric representations with those of [13] in figs. 4.15 and 4.16. In some of the chiral extrapolations, no clear signal was detected as the pseudoscalar mass approached zero and we cannot make a reliable extrapolation to the chiral limit. In such cases, the data points are shown but the chiral extrapolation (otherwise shown by a grey band) is omitted. This low signal-to-noise ratio is most common among the heaviest meson states (axial-vector, scalar and axial-tensor).

$Sp(4)$ fundamental fermions								
Volume	β	am_0	Pseudoscalar		Vector		Axial-vector	
			I_{fit}	χ^2/d.o.f.	I_{fit}	χ^2/d.o.f.	I_{fit}	χ^2/d.o.f.
$24^3 \times 48$	7.62	-0.7	[15, 22]	0.42	[18, 21]	0.12	[10, 13]	0.35
$24^3 \times 48$	7.62	-0.73	[16, 23]	0.82	[18, 23]	0.17	[8, 13]	1.16
$24^3 \times 48$	7.62	-0.75	[12, 23]	0.97	[17, 21]	0.23	[7, 13]	1.09
$24^3 \times 48$	7.62	-0.77	[12, 22]	1.35	[12, 22]	1.49	[8, 11]	1.58
$24^3 \times 48$	7.62	-0.78	[15, 21]	1.41	[11, 23]	0.84	–	–
$24^3 \times 48$	7.62	-0.79	[11, 23]	1.21	[12, 23]	0.89	[8, 10]	2.15
$48^3 \times 60$	7.7	-0.73	[14, 29]	0.73	[18, 29]	0.48	[11, 14]	0.44
$48^3 \times 60$	7.7	-0.75	[13, 28]	0.75	[16, 21]	0.79	[10, 15]	1.45
$48^3 \times 60$	7.7	-0.76	[13, 29]	1.02	[17, 21]	0.85	[9, 12]	0.16
$48^3 \times 60$	7.85	-0.6	[20, 28]	0.67	[20, 28]	1.57	[14, 25]	1.39
$48^3 \times 60$	7.85	-0.65	[25, 28]	0.09	[18, 29]	0.54	[12, 15]	0.19
$48^3 \times 60$	7.85	-0.68	[17, 27]	1.27	[18, 29]	0.77	[12, 17]	0.58
$48^3 \times 60$	7.85	-0.7	[24, 29]	1.80	[25, 28]	0.49	[12, 16]	3.73
$48^3 \times 60$	7.85	-0.71	[24, 28]	0.24	[17, 29]	0.83	[10, 14]	2.81
$48^3 \times 60$	7.85	-0.72	[16, 25]	0.93	[14, 29]	1.48	[11, 13]	4.41
$48^3 \times 60$	7.85	-0.73	[13, 28]	1.32	[15, 21]	1.13	[10, 13]	1.81
$48^3 \times 60$	8.0	-0.6	[21, 29]	1.60	[24, 27]	0.18	[13, 26]	0.74
$48^3 \times 60$	8.0	-0.625	[24, 29]	1.47	[25, 28]	0.06	[14, 17]	1.38
$48^3 \times 60$	8.0	-0.64	[26, 29]	0.41	[26, 29]	0.86	[16, 20]	0.75
$48^3 \times 60$	8.0	-0.65	[21, 28]	2.32	[17, 29]	1.13	–	–
$48^3 \times 60$	8.0	-0.66	[19, 29]	1.34	[19, 28]	1.63	[12, 17]	0.75
$48^3 \times 60$	8.0	-0.67	[19, 29]	1.29	[19, 28]	1.52	[12, 16]	0.60
$48^3 \times 60$	8.0	-0.68	[25, 29]	0.15	[24, 27]	0.05	–	–
$48^3 \times 60$	8.0	-0.69	[17, 29]	1.07	[15, 20]	0.55	[10, 12]	1.44
$48^3 \times 60$	8.2	-0.62	[24, 27]	0.12	[22, 29]	0.75	[15, 19]	1.64
$48^3 \times 60$	8.2	-0.64	[21, 29]	0.91	[21, 29]	0.79	[17, 20]	0.21
$48^3 \times 60$	8.2	-0.646	[22, 27]	1.16	[22, 27]	0.12	[14, 17]	0.06

Table 4.5: $Sp(4)$ meson fit ranges and reduced chi-squares in the fundamental representation. The '–' symbol denotes a case in which no reliable signal was detected.

$Sp(4)$ fundamental fermions								
Volume	β	am_0	Scalar		Tensor		Axial-tensor	
			I_{fit}	χ^2/d.o.f.	I_{fit}	χ^2/d.o.f.	I_{fit}	χ^2/d.o.f.
$24^3 \times 48$	7.62	-0.7	[8, 15]	1.46	[16, 21]	1.17	[10, 13]	2.34
$24^3 \times 48$	7.62	-0.73	[8, 11]	0.05	[15, 23]	0.31	[8, 13]	1.06
$24^3 \times 48$	7.62	-0.75	[7, 12]	0.20	[16, 21]	0.12	[9, 12]	1.74
$24^3 \times 48$	7.62	-0.77	[8, 11]	0.46	[12, 21]	0.90	[7, 10]	1.69
$24^3 \times 48$	7.62	-0.78	[7, 11]	0.18	[13, 22]	0.99	–	–
$24^3 \times 48$	7.62	-0.79	[6, 8]	3.65	[9, 23]	1.34	[7, 10]	0.86
$48^3 \times 60$	7.7	-0.73	[13, 16]	1.89	[17, 29]	1.55	[11, 14]	2.16
$48^3 \times 60$	7.7	-0.75	[8, 14]	0.16	[13, 28]	0.59	[8, 11]	0.73
$48^3 \times 60$	7.7	-0.76	[10, 14]	0.28	[13, 29]	1.09	[9, 13]	0.70
$48^3 \times 60$	7.85	-0.6	[21, 25]	0.02	[17, 28]	1.23	[19, 25]	0.90
$48^3 \times 60$	7.85	-0.65	[13, 24]	1.06	[23, 29]	0.11	[14, 17]	0.05
$48^3 \times 60$	7.85	-0.68	[13, 18]	2.07	[16, 29]	1.32	[13, 17]	1.44
$48^3 \times 60$	7.85	-0.7	[14, 18]	0.46	[19, 29]	1.11	[10, 17]	1.52
$48^3 \times 60$	7.85	-0.71	[10, 13]	2.86	[23, 29]	1.05	[11, 16]	1.87
$48^3 \times 60$	7.85	-0.72	[9, 13]	2.98	[17, 27]	1.61	[12, 15]	2.35
$48^3 \times 60$	7.85	-0.73	–	–	[14, 23]	0.47	[10, 13]	0.14
$48^3 \times 60$	8.0	-0.6	[13, 25]	0.74	[22, 29]	0.74	[19, 24]	0.41
$48^3 \times 60$	8.0	-0.625	[14, 26]	1.35	[23, 27]	0.40	[20, 24]	1.01
$48^3 \times 60$	8.0	-0.64	[19, 24]	0.12	[23, 27]	2.42	[17, 20]	0.23
$48^3 \times 60$	8.0	-0.65	[14, 16]	2.90	[17, 29]	1.34	[18, 21]	0.16
$48^3 \times 60$	8.0	-0.66	[12, 19]	2.53	[16, 29]	1.08	[12, 20]	1.27
$48^3 \times 60$	8.0	-0.67	[15, 18]	0.05	[19, 29]	0.36	[15, 18]	0.80
$48^3 \times 60$	8.0	-0.68	[12, 16]	1.92	[15, 29]	1.15	[11, 13]	2.33
$48^3 \times 60$	8.0	-0.69	[8, 10]	1.72	[20, 29]	1.03	[10, 12]	5.12
$48^3 \times 60$	8.2	-0.62	[15, 21]	1.87	[26, 29]	0.32	[16, 19]	1.81
$48^3 \times 60$	8.2	-0.64	[17, 21]	0.20	[23, 27]	0.54	[19, 22]	0.09
$48^3 \times 60$	8.2	-0.646	[10, 13]	2.13	[17, 27]	1.54	[12, 16]	0.16

Table 4.6: $Sp(4)$ meson fit ranges and reduced chi-squares in the fundamental representation. The '–' symbol denotes a case in which no reliable signal was detected.

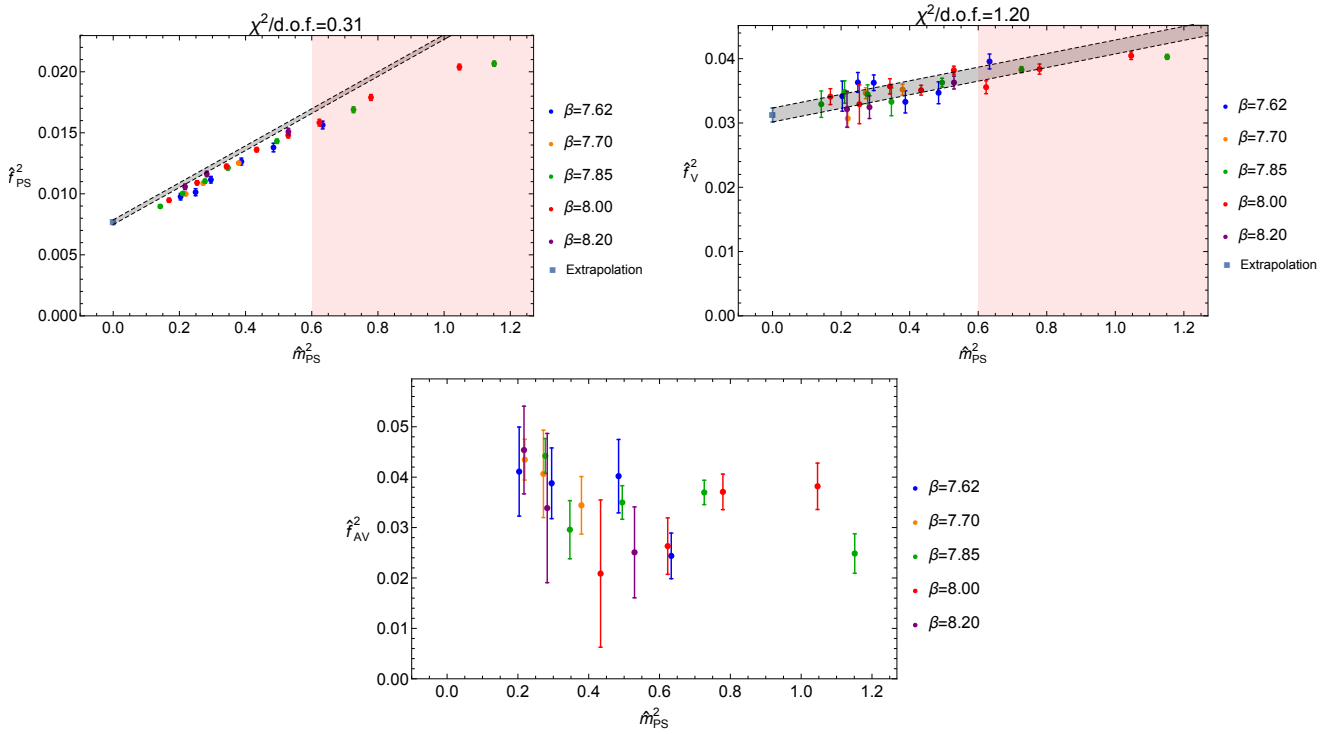

Figure 4.3: Decay constants squared for PS, V and AV channels, comprised of fermions in the fundamental representation of $Sp(4)$. The reduced chi-squared value is printed at the top of each plot. Data points in the pink shaded region are not included in the curve-fitting procedure. The grey band represents the continuum and massless extrapolation with the blue square being the observable in the chiral limit and the vertical width corresponding to the statistical error. In instances where a reliable extrapolation cannot be made, no grey band is shown. All quantities are expressed in units of gradient flow scale, w_0.

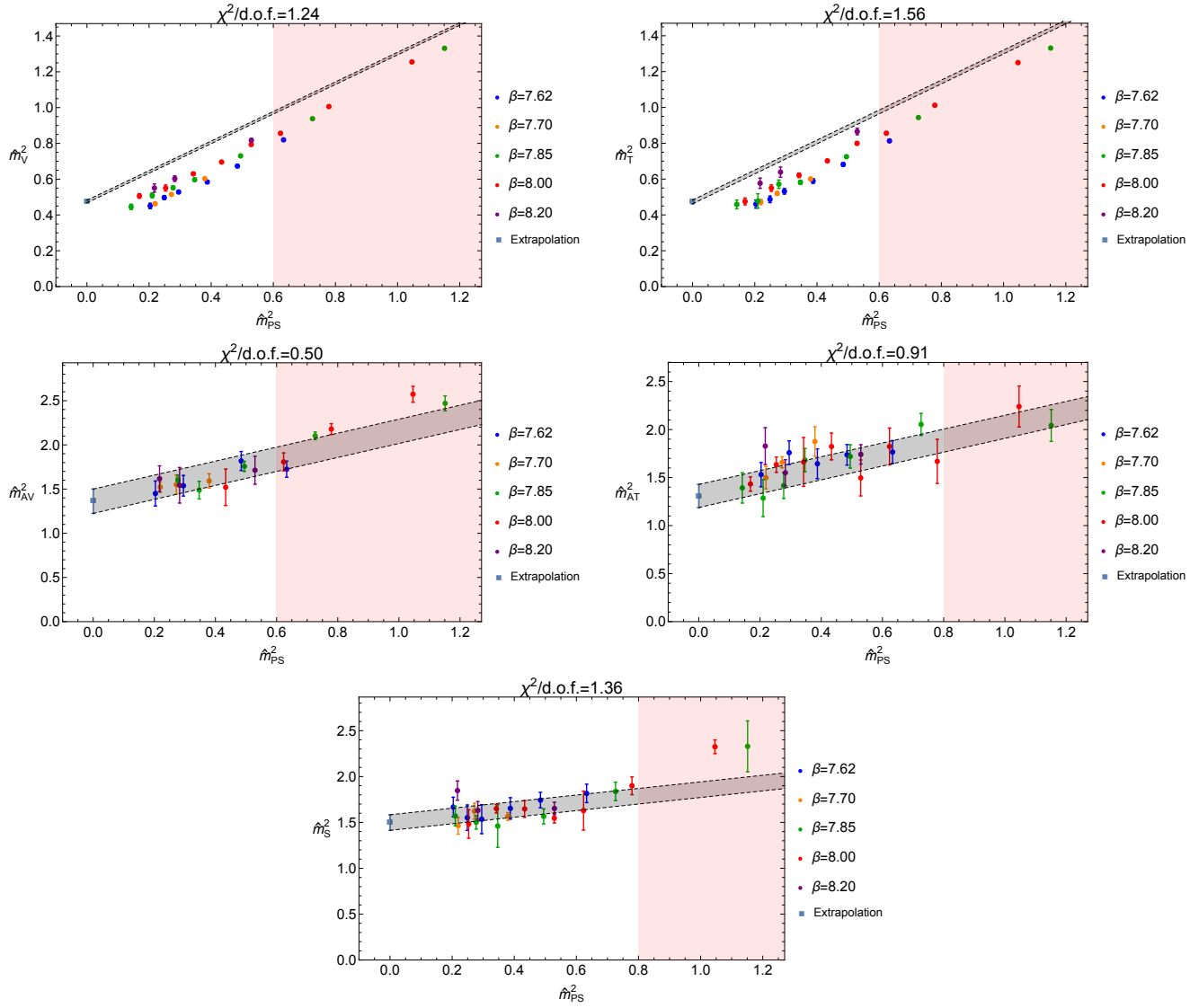

Figure 4.4: Masses squared for V, T, AV, AT and S channels, comprised of fermions in the fundamental representation of $Sp(4)$. The reduced chi-squared value is printed at the top of each plot. Data points in the pink shaded region are not included in the curve-fitting procedure. The grey band represents the continuum and massless extrapolation with the blue square being the observable in the chiral limit and the vertical width corresponding to the statistical error. In instances where a reliable extrapolation cannot be made, no grey band is shown. All quantities are expressed in units of gradient flow scale, w_0.

$Sp(4)$ antisymmetric fermions								
Volume	β	am_0	Pseudoscalar		Vector		Axial-vector	
			I_{fit}	χ^2/d.o.f.	I_{fit}	χ^2/d.o.f.	I_{fit}	χ^2/d.o.f.
$24^3 \times 48$	7.62	-1.05	[11, 23]	0.93	[19, 22]	0.10	–	–
$24^3 \times 48$	7.62	-1.08	[18, 22]	1.61	[10, 23]	1.09	–	–
$24^3 \times 48$	7.62	-1.1	[18, 22]	1.00	[13, 18]	0.06	[6, 9]	3.65
$24^3 \times 48$	7.62	-1.12	[11, 23]	0.89	[9, 22]	1.05	–	–
$24^3 \times 48$	7.62	-1.13	[18, 23]	2.14	[10, 15]	0.92	–	–
$24^3 \times 48$	7.62	-1.14	[18, 22]	1.93	[12, 15]	3.05	–	–
$48^3 \times 60$	7.7	-1.05	[19, 29]	0.70	[19, 29]	1.24	[8, 11]	0.99
$48^3 \times 60$	7.7	-1.08	[26, 29]	1.83	[16, 27]	1.54	[8, 11]	0.67
$48^3 \times 60$	7.7	-1.09	[16, 28]	1.34	[16, 27]	0.32	–	–
$48^3 \times 60$	7.7	-1.1	[14, 29]	1.22	[15, 29]	1.34	[7, 11]	1.63
$48^3 \times 60$	7.7	-1.11	[11, 29]	1.04	[14, 23]	1.65	–	–
$48^3 \times 60$	7.7	-1.12	[11, 29]	1.13	[14, 22]	1.68	[7, 10]	0.38
$48^3 \times 60$	7.85	-1.03	[13, 29]	1.04	[19, 29]	1.58	[9, 11]	4.79
$48^3 \times 60$	7.85	-1.04	[15, 29]	1.28	[14, 29]	1.09	[9, 14]	0.91
$48^3 \times 60$	7.85	-1.05	[17, 29]	1.26	[11, 29]	0.99	[9, 13]	1.71
$48^3 \times 60$	7.85	-1.06	[12, 29]	1.29	[19, 23]	0.07	–	–
$48^3 \times 60$	8.0	-0.95	[22, 28]	1.42	[26, 29]	0.54	[10, 19]	0.63
$48^3 \times 60$	8.0	-0.983	[19, 29]	1.26	[20, 29]	0.32	[11, 15]	0.70
$48^3 \times 60$	8.0	-0.99	[16, 27]	1.33	[24, 27]	0.14	[10, 13]	1.20
$48^3 \times 60$	8.0	-1.01	[22, 29]	1.36	[15, 28]	0.92	[10, 12]	0.96
$48^3 \times 60$	8.0	-1.015	[20, 29]	0.74	[13, 24]	0.68	–	–
$48^3 \times 60$	8.2	-0.95	[19, 26]	1.36	[22, 27]	0.22	[12, 14]	1.32
$48^3 \times 60$	8.2	-0.961	[16, 29]	1.05	[15, 27]	1.49	[11, 13]	2.46

Table 4.7: $Sp(4)$ meson fit ranges and reduced chi-squares in the antisymmetric representation. The '–' symbol denotes a case in which no reliable signal was detected.

$Sp(4)$ antisymmetric fermions								
Volume	β	am_0	Scalar		Tensor		Axial-tensor	
			I_{fit}	χ^2/d.o.f.	I_{fit}	χ^2/d.o.f.	I_{fit}	χ^2/d.o.f.
$24^3 \times 48$	7.62	-1.05	[7, 10]	1.66	[11, 23]	0.97	[6, 8]	2.10
$24^3 \times 48$	7.62	-1.08	[7, 10]	0.56	[9, 23]	0.93	–	–
$24^3 \times 48$	7.62	-1.1	[8, 12]	2.91	[8, 22]	0.96	–	–
$24^3 \times 48$	7.62	-1.12	–	–	[15, 20]	1.28	–	–
$24^3 \times 48$	7.62	-1.13	–	–	[10, 20]	1.58	–	–
$24^3 \times 48$	7.62	-1.14	[7, 9]	4.63	[8, 13]	0.21	–	–
$48^3 \times 60$	7.7	-1.05	[12, 15]	0.18	[21, 29]	1.63	[8, 11]	1.73
$48^3 \times 60$	7.7	-1.08	[8, 13]	1.11	[13, 29]	0.91	[8, 11]	1.07
$48^3 \times 60$	7.7	-1.09	[9, 13]	1.39	[24, 27]	0.06	[8, 10]	0.19
$48^3 \times 60$	7.7	-1.1	[8, 10]	2.76	[20, 23]	0.01	[7, 10]	1.91
$48^3 \times 60$	7.7	-1.11	[6, 9]	1.97	[12, 19]	0.57	[7, 9]	0.63
$48^3 \times 60$	7.7	-1.12	–	–	[11, 14]	0.04	[6, 8]	3.07
$48^3 \times 60$	7.85	-1.03	[12, 15]	0.25	[11, 29]	1.24	–	–
$48^3 \times 60$	7.85	-1.04	[8, 12]	2.41	[25, 29]	0.65	[10, 12]	0.53
$48^3 \times 60$	7.85	-1.05	[10, 13]	0.25	[13, 25]	0.87	[7, 10]	2.72
$48^3 \times 60$	7.85	-1.06	[7, 9]	0.14	[12, 18]	0.21	–	–
$48^3 \times 60$	8.0	-0.95	[19, 22]	0.18	[17, 27]	1.37	[13, 16]	0.09
$48^3 \times 60$	8.0	-0.983	[11, 18]	1.20	[21, 27]	0.78	[11, 14]	0.44
$48^3 \times 60$	8.0	-0.99	[11, 17]	0.78	[14, 29]	1.45	[11, 14]	1.53
$48^3 \times 60$	8.0	-1.01	[11, 14]	0.07	[16, 22]	0.07	[9, 12]	0.63
$48^3 \times 60$	8.0	-1.015	[9, 13]	0.95	[16, 21]	0.22	[8, 10]	3.67
$48^3 \times 60$	8.2	-0.95	[18, 21]	0.00	[25, 28]	0.05	[11, 15]	0.79
$48^3 \times 60$	8.2	-0.961	[14, 20]	0.38	[16, 20]	0.29	[10, 13]	0.71

Table 4.8: $Sp(4)$ meson fit ranges and reduced chi-squares in the antisymmetric representation. The '–' symbol denotes a case in which no reliable signal was detected.

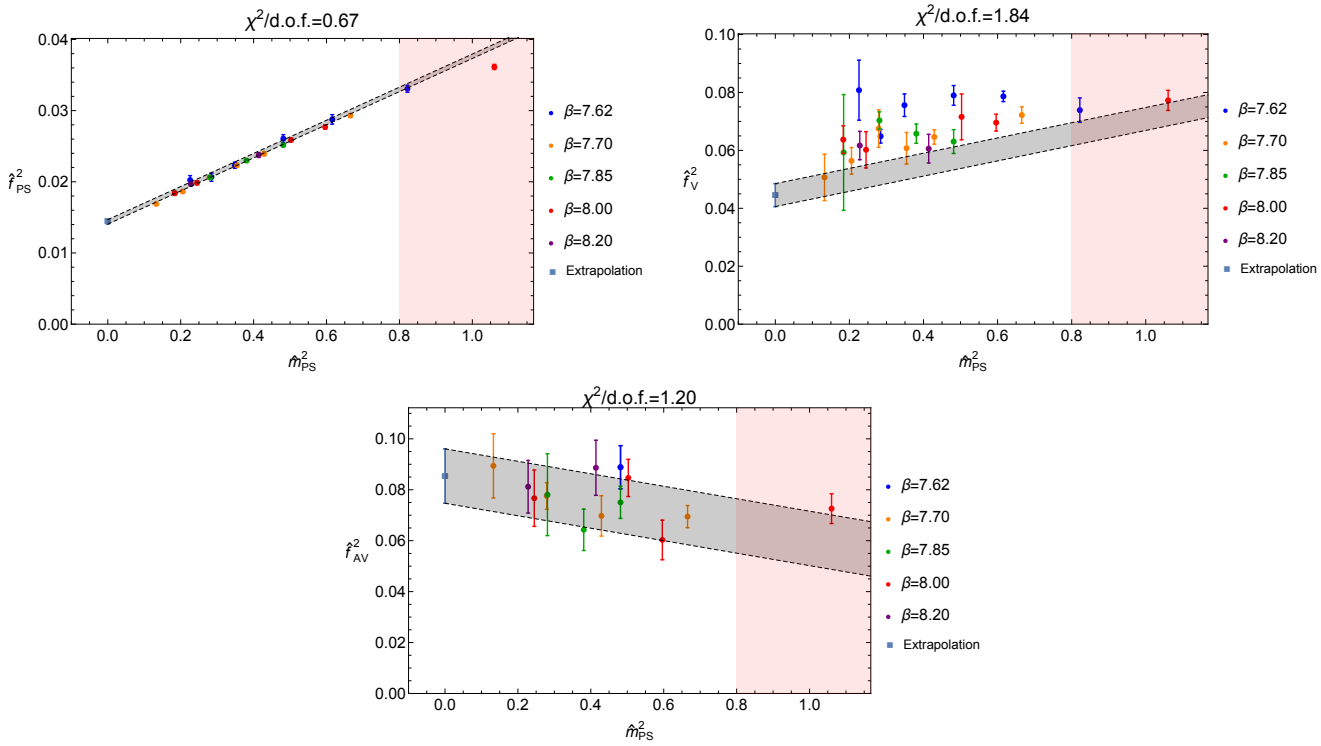

Figure 4.5: Decay constants squared for PS, V and AV channels, comprised of fermions in the antisymmetric representation of $Sp(4)$. The reduced chi-squared value is printed at the top of each plot. Data points in the pink shaded region are not included in the curve-fitting procedure. The grey band represents the continuum and massless extrapolation with the blue square being the observable in the chiral limit and the vertical width corresponding to the statistical error. In instances where a reliable extrapolation cannot be made, no grey band is shown. All quantities are expressed in units of gradient flow scale, w_0.

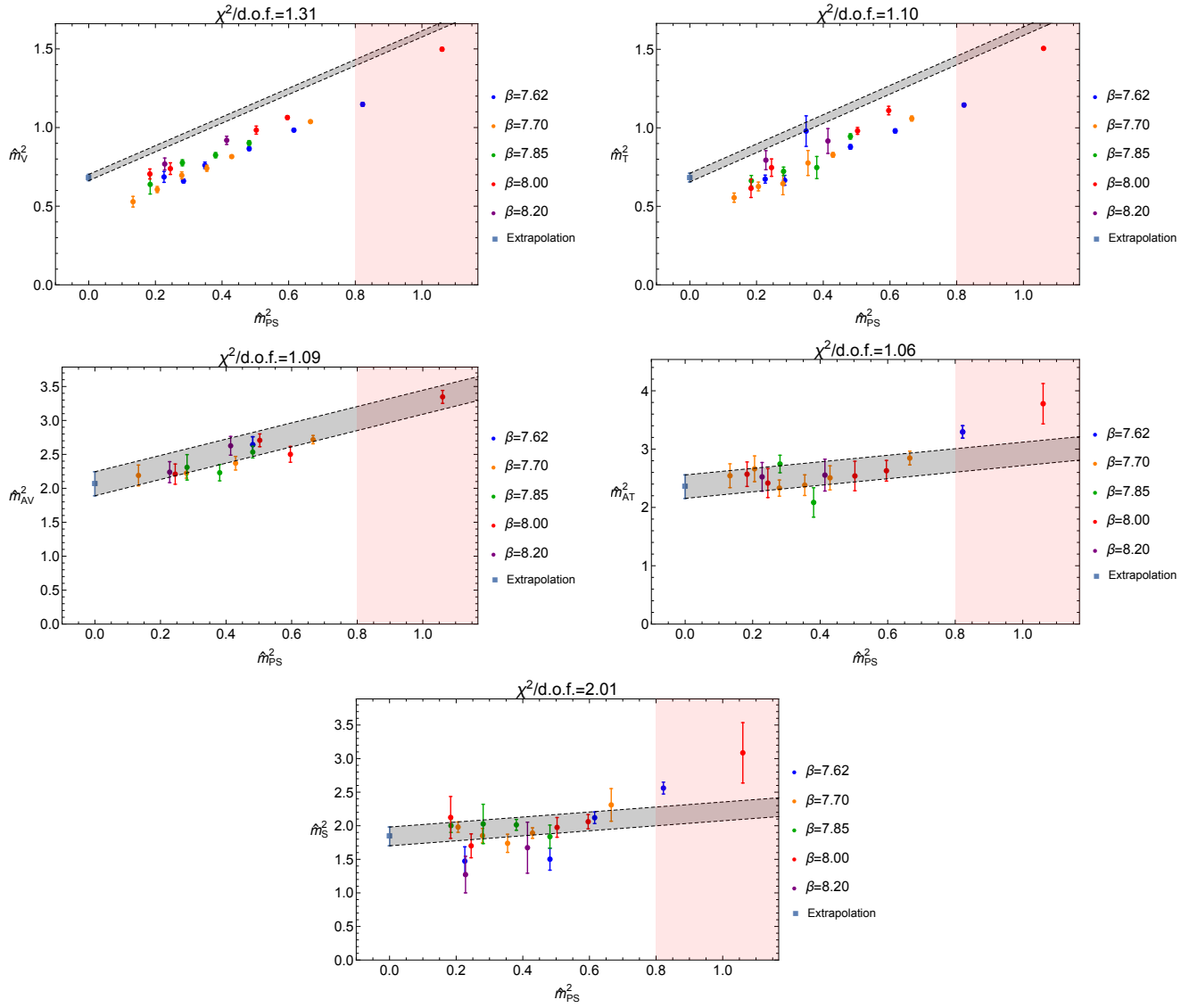

Figure 4.6: Masses squared for V, T, AV, AT and S channels, comprised of fermions in the antisymmetric representation of $Sp(4)$. The reduced chi-squared value is printed at the top of each plot. Data points in the pink shaded region are not included in the curve-fitting procedure. The grey band represents the continuum and massless extrapolation with the blue square being the observable in the chiral limit and the vertical width corresponding to the statistical error. In instances where a reliable extrapolation cannot be made, no grey band is shown. All quantities are expressed in units of gradient flow scale, w_0.

$Sp(4)$ symmetric fermions								
Volume	β	am_0	Pseudoscalar		Vector		Axial-vector	
			I_{fit}	χ^2/d.o.f.	I_{fit}	χ^2/d.o.f.	I_{fit}	χ^2/d.o.f.
$24^3 \times 48$	7.62	-1.47	[11, 23]	0.94	[11, 23]	0.39	–	–
$24^3 \times 48$	7.62	-1.48	[10, 21]	1.29	[17, 22]	0.34	–	–
$24^3 \times 48$	7.62	-1.485	[18, 23]	0.91	[13, 21]	0.47	–	–
$24^3 \times 48$	7.62	-1.49	[20, 23]	1.06	[17, 22]	0.03	–	–
$24^3 \times 48$	7.62	-1.505	[10, 23]	1.27	[11, 17]	1.78	–	–
$24^3 \times 48$	7.62	-1.51	[14, 23]	1.27	[9, 18]	0.66	–	–
$48^3 \times 60$	7.7	-1.43	[18, 29]	1.28	[11, 28]	1.43	–	–
$48^3 \times 60$	7.7	-1.44	[12, 28]	1.00	[25, 28]	0.39	–	–
$48^3 \times 60$	7.7	-1.45	[21, 29]	1.11	[11, 28]	1.29	–	–
$48^3 \times 60$	7.7	-1.46	[15, 29]	0.85	[15, 25]	0.22	–	–
$48^3 \times 60$	7.7	-1.47	[13, 29]	1.03	[17, 21]	0.00	–	–
$48^3 \times 60$	7.85	-1.36	[15, 29]	1.10	[14, 29]	0.87	[10, 13]	0.84
$48^3 \times 60$	7.85	-1.37	[18, 29]	1.38	[15, 27]	1.52	[8, 11]	3.66
$48^3 \times 60$	7.85	-1.38	[24, 28]	0.54	[18, 29]	1.27	[9, 12]	0.04
$48^3 \times 60$	7.85	-1.39	[14, 29]	1.34	[16, 27]	0.82	[7, 9]	0.02
$48^3 \times 60$	7.85	-1.4	[15, 28]	1.37	[16, 29]	0.57	[9, 11]	0.20
$48^3 \times 60$	7.85	-1.41	[24, 28]	0.98	[25, 28]	0.00	[8, 11]	1.41
$48^3 \times 60$	7.85	-1.42	[12, 27]	1.30	[12, 26]	0.74	–	–
$48^3 \times 60$	8.0	-1.31	[16, 29]	1.22	[25, 29]	0.49	[9, 15]	0.26
$48^3 \times 60$	8.0	-1.32	[24, 27]	1.77	[14, 29]	1.43	[13, 16]	0.43
$48^3 \times 60$	8.0	-1.33	[16, 29]	1.04	[20, 27]	0.12	[12, 17]	0.79
$48^3 \times 60$	8.0	-1.34	[26, 29]	0.46	[18, 29]	1.32	[8, 14]	0.21
$48^3 \times 60$	8.0	-1.35	[15, 25]	1.37	[24, 27]	0.00	[9, 13]	1.84
$48^3 \times 60$	8.0	-1.36	[25, 29]	1.25	[17, 29]	1.53	[9, 12]	3.37
$48^3 \times 60$	8.0	-1.37	[17, 29]	1.39	[21, 27]	1.09	[9, 13]	1.78
$48^3 \times 60$	8.2	-1.26	[24, 27]	1.60	[20, 29]	1.12	[14, 17]	0.22
$48^3 \times 60$	8.2	-1.27	[21, 29]	1.48	[18, 29]	0.85	[10, 18]	0.86
$48^3 \times 60$	8.2	-1.28	[21, 28]	1.05	[16, 27]	0.91	[13, 17]	0.03
$48^3 \times 60$	8.2	-1.29	[22, 27]	1.33	[26, 29]	2.84	[14, 17]	0.25
$48^3 \times 60$	8.2	-1.30	[20, 29]	1.31	[18, 28]	1.62	[10, 13]	4.46
$48^3 \times 60$	8.2	-1.31	[18, 29]	0.85	[26, 29]	1.02	[11, 14]	0.04
$48^3 \times 60$	8.2	-1.32	[17, 29]	1.15	[15, 25]	0.46	[9, 14]	0.39

Table 4.9: $Sp(4)$ meson fit ranges and reduced chi-squares in the symmetric representation. The '–' symbol denotes a case in which no reliable signal was detected.

$Sp(4)$ symmetric fermions								
Volume	β	am_0	Scalar		Tensor		Axial-tensor	
			I_{fit}	χ^2/d.o.f.	I_{fit}	χ^2/d.o.f.	I_{fit}	χ^2/d.o.f.
$24^3 \times 48$	7.62	-1.47	–	–	[9, 20]	1.74	–	–
$24^3 \times 48$	7.62	-1.48	–	–	[8, 19]	1.02	–	–
$24^3 \times 48$	7.62	-1.485	–	–	[12, 20]	0.49	–	–
$24^3 \times 48$	7.62	-1.49	[5, 7]	0.04	[14, 17]	0.03	–	–
$24^3 \times 48$	7.62	-1.505	–	–	[7, 14]	1.41	–	–
$24^3 \times 48$	7.62	-1.51	–	–	[9, 14]	1.01	–	–
$48^3 \times 60$	7.7	-1.43	–	–	[22, 25]	0.23	–	–
$48^3 \times 60$	7.7	-1.44	–	–	[14, 28]	1.45	–	–
$48^3 \times 60$	7.7	-1.45	–	–	[10, 25]	0.89	–	–
$48^3 \times 60$	7.7	-1.46	[6, 8]	0.04	[10, 22]	1.01	–	–
$48^3 \times 60$	7.7	-1.47	[6, 8]	1.98	[14, 18]	1.39	–	–
$48^3 \times 60$	7.85	-1.36	[10, 14]	1.41	[21, 27]	0.94	[7, 10]	2.06
$48^3 \times 60$	7.85	-1.37	[11, 14]	1.11	[23, 29]	0.60	[7, 10]	0.50
$48^3 \times 60$	7.85	-1.38	[8, 15]	0.23	[13, 27]	1.25	–	–
$48^3 \times 60$	7.85	-1.39	[8, 13]	1.33	[11, 27]	1.28	–	–
$48^3 \times 60$	7.85	-1.4	[8, 11]	0.58	[16, 26]	0.51	–	–
$48^3 \times 60$	7.85	-1.41	[9, 12]	1.96	[14, 19]	0.79	–	–
$48^3 \times 60$	7.85	-1.42	[7, 10]	0.28	[12, 22]	1.38	[7, 9]	1.82
$48^3 \times 60$	8.0	-1.31	[17, 20]	0.44	[14, 29]	0.98	–	–
$48^3 \times 60$	8.0	-1.32	[11, 18]	0.59	[14, 28]	0.98	[11, 14]	0.65
$48^3 \times 60$	8.0	-1.33	[12, 18]	1.60	[23, 28]	1.14	[10, 13]	0.15
$48^3 \times 60$	8.0	-1.34	[14, 17]	0.13	[11, 29]	1.25	[8, 12]	2.93
$48^3 \times 60$	8.0	-1.35	[15, 18]	0.20	[11, 28]	1.41	[7, 11]	0.14
$48^3 \times 60$	8.0	-1.36	[9, 13]	0.20	[11, 28]	0.89	[7, 9]	0.30
$48^3 \times 60$	8.0	-1.37	[9, 13]	3.36	[17, 20]	0.09	[7, 10]	0.31
$48^3 \times 60$	8.2	-1.26	[13, 25]	1.38	[17, 29]	1.49	[10, 17]	1.66
$48^3 \times 60$	8.2	-1.27	[12, 21]	1.25	[17, 29]	0.53	[10, 13]	1.04
$48^3 \times 60$	8.2	-1.28	[17, 20]	0.04	[14, 28]	0.88	[11, 14]	0.07
$48^3 \times 60$	8.2	-1.29	[11, 19]	1.65	[15, 29]	1.24	[10, 14]	2.35
$48^3 \times 60$	8.2	-1.30	[11, 22]	1.01	[14, 28]	1.47	[10, 13]	0.94
$48^3 \times 60$	8.2	-1.31	[14, 18]	0.49	[19, 22]	0.24	[9, 12]	2.71
$48^3 \times 60$	8.2	-1.32	[8, 10]	1.23	[15, 18]	0.04	[7, 9]	0.07

Table 4.10: $Sp(4)$ meson fit ranges and reduced chi-squares in the symmetric representation. The '–' symbol denotes a case in which no reliable signal was detected.

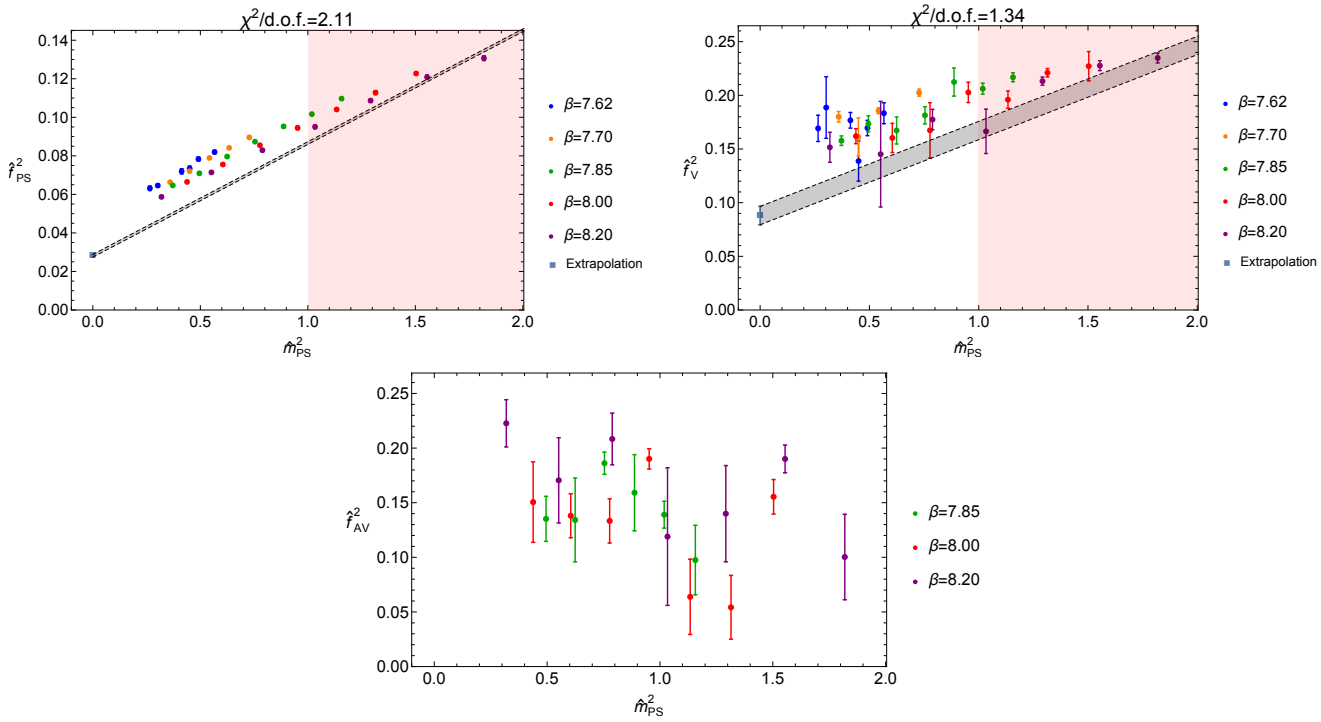

Figure 4.7: Decay constants squared for PS, V and AV channels, comprised of fermions in the symmetric representation of $Sp(4)$. The reduced chi-squared value is printed at the top of each plot. Data points in the pink shaded region are not included in the curve-fitting procedure. The grey band represents the continuum and massless extrapolation with the blue square being the observable in the chiral limit and the vertical width corresponding to the statistical error. In instances where a reliable extrapolation cannot be made, no grey band is shown. All quantities are expressed in units of gradient flow scale, w_0.

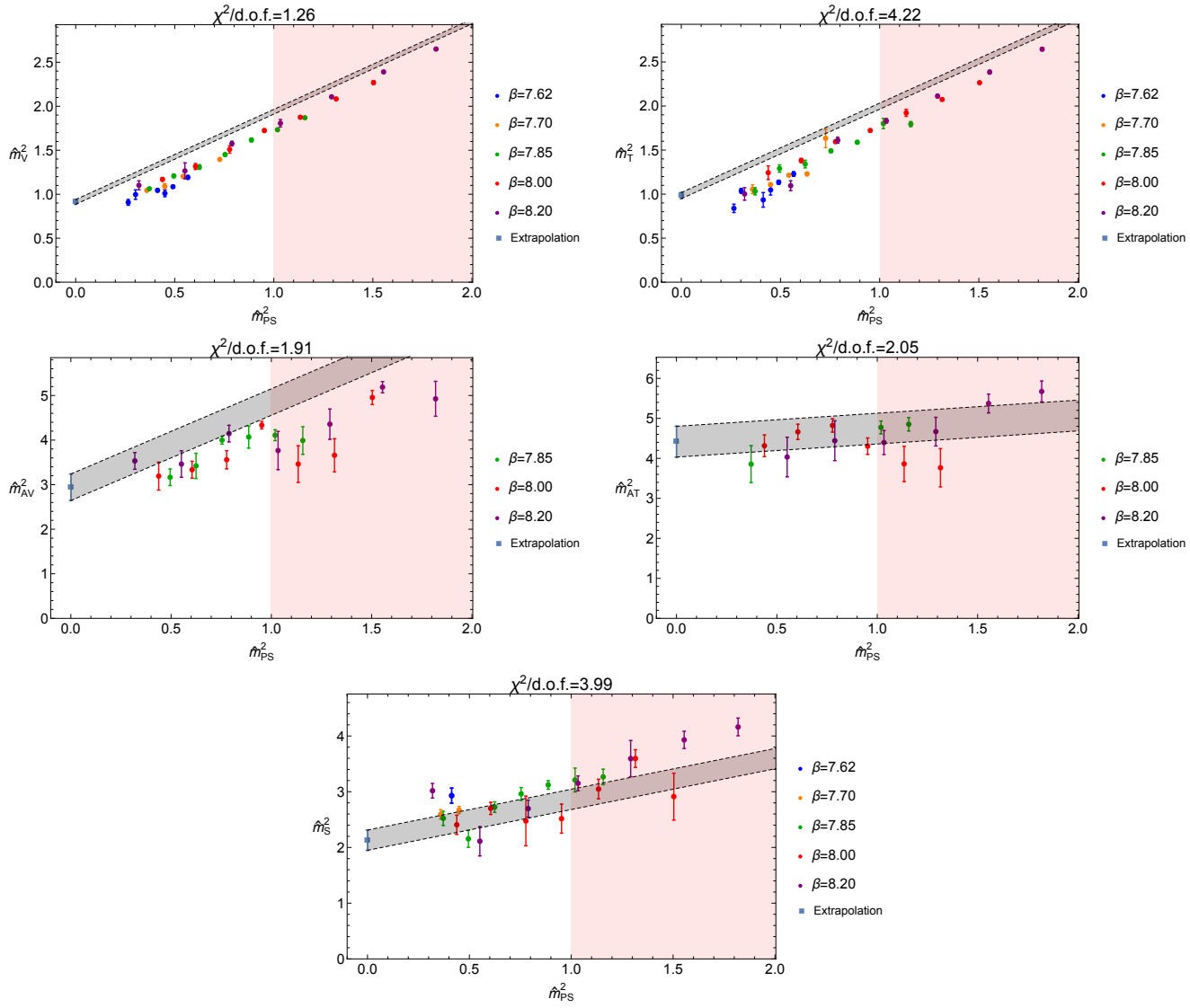

Figure 4.8: Masses squared for V, T, AV, AT and S channels, comprised of fermions in the symmetric representation of $Sp(4)$. The reduced chi-squared value is printed at the top of each plot. Data points in the pink shaded region are not included in the curve-fitting procedure. The grey band represents the continuum and massless extrapolation with the blue square being the observable in the chiral limit and the vertical width corresponding to the statistical error. In instances where a reliable extrapolation cannot be made, no grey band is shown. All quantities are expressed in units of gradient flow scale, w_0.

$Sp(6)$ fundamental fermions								
Volume	β	am_0	Pseudoscalar		Vector		Axial-vector	
			I_{fit}	χ^2/d.o.f.	I_{fit}	χ^2/d.o.f.	I_{fit}	χ^2/d.o.f.
$12^3 \times 24$	15.6	-0.80	[9, 11]	1.20	[9, 11]	0.54	–	–
$12^3 \times 24$	15.6	-0.81	[8, 11]	0.85	[9, 11]	2.61	–	–
$12^3 \times 24$	15.6	-0.82	[9, 11]	0.65	[8, 10]	1.74	–	–
$12^3 \times 24$	15.6	-0.83	[9, 11]	1.58	[9, 11]	3.83	–	–
$12^3 \times 24$	15.6	-0.84	[8, 11]	0.10	–	–	–	–
$16^3 \times 32$	16.1	-0.72	[13, 15]	2.75	[12, 15]	4.95	[10, 14]	1.48
$16^3 \times 32$	16.1	-0.73	[12, 15]	0.36	[11, 14]	2.68	–	–
$16^3 \times 32$	16.1	-0.74	[12, 15]	1.47	[12, 15]	1.17	–	–
$16^3 \times 32$	16.1	-0.75	[10, 14]	0.71	[10, 15]	0.45	–	–
$16^3 \times 32$	16.1	-0.76	[10, 15]	1.51	[12, 15]	0.09	[7, 10]	2.52
$20^3 \times 40$	16.5	-0.67	[16, 19]	1.81	[15, 18]	0.48	[12, 16]	1.37
$20^3 \times 40$	16.5	-0.68	[15, 17]	6.53	[15, 19]	2.30	[13, 16]	2.72
$20^3 \times 40$	16.5	-0.69	[14, 16]	4.04	[16, 19]	1.83	[11, 14]	0.73
$20^3 \times 40$	16.5	-0.70	[15, 18]	0.36	[14, 19]	0.77	[9, 12]	3.04
$20^3 \times 40$	16.5	-0.71	[12, 19]	0.81	[14, 17]	1.93	–	–
$24^3 \times 48$	16.7	-0.65	[20, 23]	4.82	[19, 23]	2.32	[13, 20]	0.59
$24^3 \times 48$	16.7	-0.66	[17, 23]	0.60	[18, 23]	0.50	[13, 18]	0.09
$24^3 \times 48$	16.7	-0.67	[20, 23]	0.22	[18, 21]	0.05	[13, 16]	0.37
$24^3 \times 48$	16.7	-0.68	[17, 23]	1.53	[18, 21]	0.24	[13, 16]	1.75
$24^3 \times 48$	16.7	-0.69	[13, 23]	0.98	[15, 18]	2.70	[9, 11]	2.86
$30^3 \times 60$	17.1	-0.63	[23, 29]	0.99	[22, 27]	0.14	[14, 23]	0.74
$30^3 \times 60$	17.1	-0.64	[20, 29]	1.09	[25, 29]	1.29	[14, 17]	3.34
$30^3 \times 60$	17.1	-0.65	[20, 28]	0.70	[18, 27]	0.58	[12, 15]	0.23

Table 4.11: $Sp(6)$ meson fit ranges and reduced chi-squares in the fundamental representation. The '–' symbol denotes a case in which no reliable signal was detected.

$Sp(6)$ fundamental fermions								
Volume	β	am_0	Scalar		Tensor		Axial-tensor	
			I_{fit}	χ^2/d.o.f.	I_{fit}	χ^2/d.o.f.	I_{fit}	χ^2/d.o.f.
$12^3 \times 24$	15.6	-0.80	–	–	[8, 11]	2.05	[6, 8]	0.25
$12^3 \times 24$	15.6	-0.81	–	–	[7, 10]	2.63	–	–
$12^3 \times 24$	15.6	-0.82	–	–	[7, 9]	2.86	–	–
$12^3 \times 24$	15.6	-0.83	–	–	[8, 11]	0.46	–	–
$12^3 \times 24$	15.6	-0.84	–	–	[7, 10]	0.67	–	–
$16^3 \times 32$	16.1	-0.72	[9, 12]	1.46	[11, 14]	1.66	[9, 12]	1.00
$16^3 \times 32$	16.1	-0.73	[7, 9]	3.57	[10, 15]	0.70	[9, 12]	0.53
$16^3 \times 32$	16.1	-0.74	–	–	[11, 15]	1.21	[8, 10]	0.65
$16^3 \times 32$	16.1	-0.75	–	–	[10, 15]	0.24	[8, 10]	6.11
$16^3 \times 32$	16.1	-0.76	–	–	–	–	–	–
$20^3 \times 40$	16.5	-0.67	[13, 16]	0.27	[14, 19]	0.16	[11, 15]	0.81
$20^3 \times 40$	16.5	-0.68	[10, 12]	7.44	[14, 19]	1.30	–	–
$20^3 \times 40$	16.5	-0.69	[11, 13]	0.51	[13, 17]	0.36	[11, 14]	0.06
$20^3 \times 40$	16.5	-0.70	[8, 11]	4.92	[15, 18]	1.50	[9, 12]	2.25
$20^3 \times 40$	16.5	-0.71	–	–	[12, 15]	0.05	[9, 11]	0.67
$24^3 \times 48$	16.7	-0.65	[12, 16]	1.60	[16, 23]	1.75	[13, 19]	1.44
$24^3 \times 48$	16.7	-0.66	[14, 17]	1.35	[13, 23]	0.62	[13, 16]	5.20
$24^3 \times 48$	16.7	-0.67	[9, 12]	4.45	[20, 23]	0.06	[11, 16]	0.67
$24^3 \times 48$	16.7	-0.68	–	–	[20, 23]	0.03	[11, 13]	2.64
$24^3 \times 48$	16.7	-0.69	–	–	[12, 14]	1.06	[9, 12]	5.03
$30^3 \times 60$	17.1	-0.63	[13, 19]	2.82	[21, 27]	0.60	[14, 21]	1.57
$30^3 \times 60$	17.1	-0.64	[12, 16]	2.59	[26, 29]	0.23	[13, 20]	1.26
$30^3 \times 60$	17.1	-0.65	[10, 13]	5.02	[20, 23]	1.47	[10, 14]	3.04

Table 4.12: $Sp(6)$ meson fit ranges and reduced chi-squares in the fundamental representation. The '–' symbol denotes a case in which no reliable signal was detected.

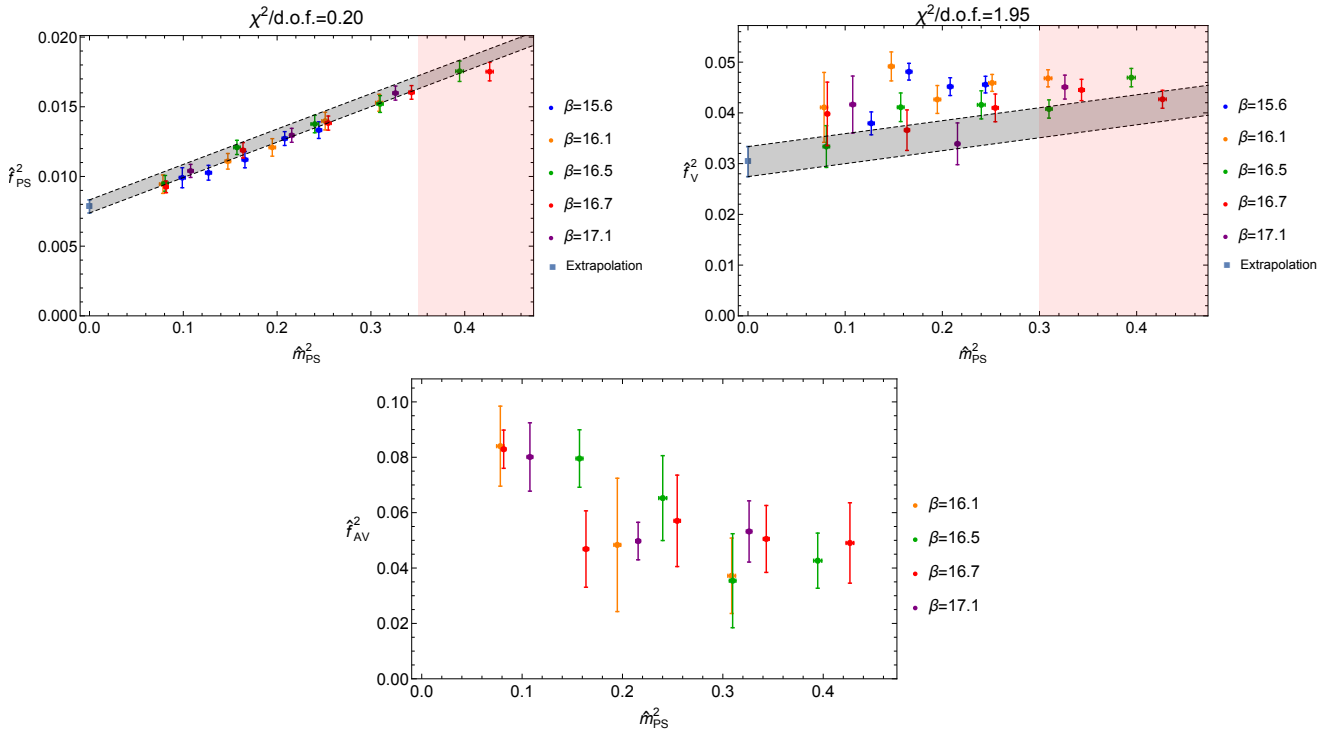

Figure 4.9: Decay constants squared for PS, V and AV channels, comprised of fermions in the fundamental representation of $Sp(6)$. The reduced chi-squared value is printed at the top of each plot. Data points in the pink shaded region are not included in the curve-fitting procedure. The grey band represents the continuum and massless extrapolation with the blue square being the observable in the chiral limit and the vertical width corresponding to the statistical error. In instances where a reliable extrapolation cannot be made, no grey band is shown. All quantities are expressed in units of gradient flow scale, w_0.

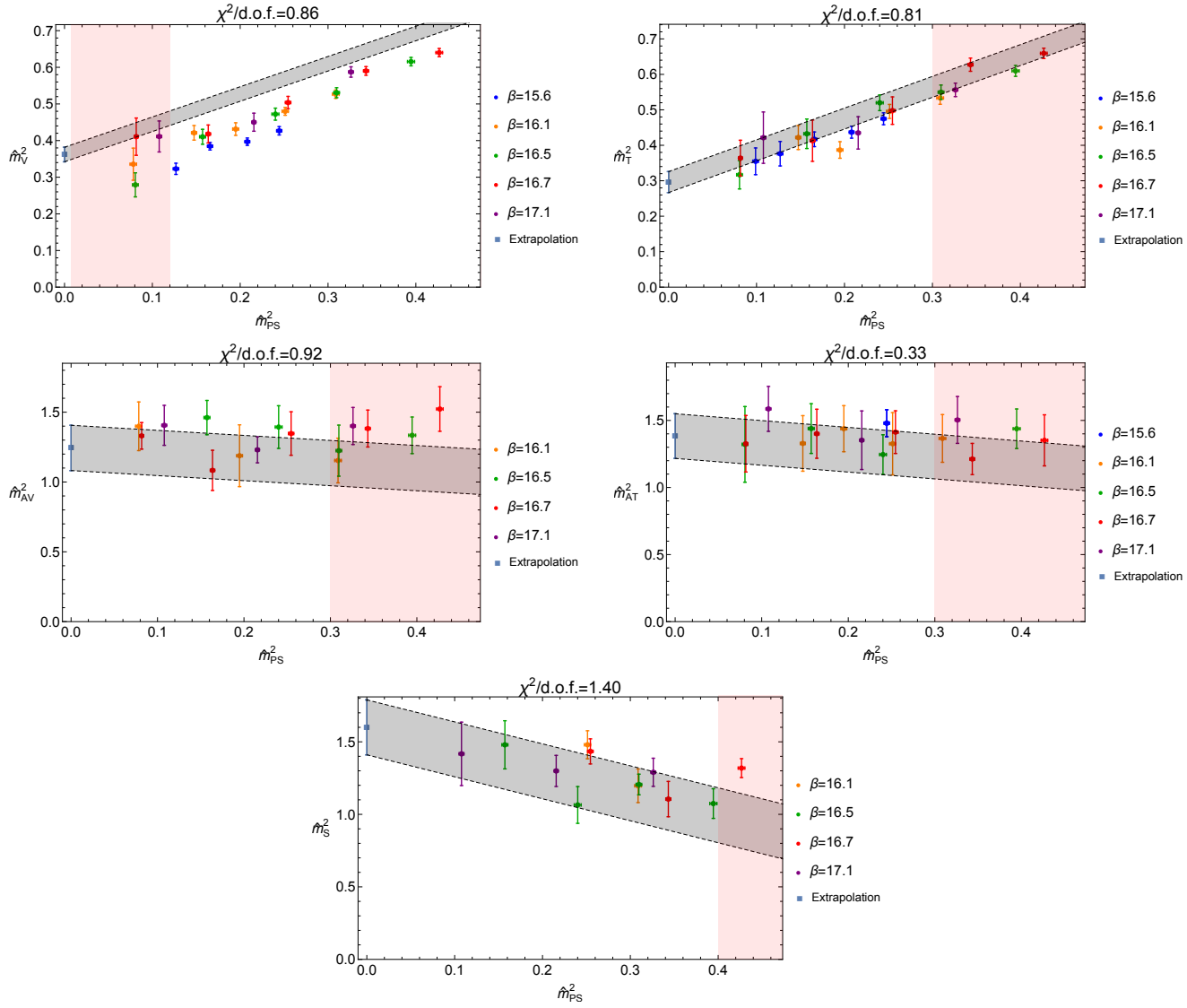

Figure 4.10: Masses squared for V, T, AV, AT and S channels, comprised of fermions in the fundamental representation of $Sp(6)$. The reduced chi-squared value is printed at the top of each plot. Data points in the pink shaded region are not included in the curve-fitting procedure. The grey band represents the continuum and massless extrapolation with the blue square being the observable in the chiral limit and the vertical width corresponding to the statistical error. In instances where a reliable extrapolation cannot be made, no grey band is shown. All quantities are expressed in units of gradient flow scale, w_0.

$Sp(6)$ antisymmetric fermions								
Volume	β	am_0	Pseudoscalar		Vector		Axial-vector	
			I_{fit}	χ^2/d.o.f.	I_{fit}	χ^2/d.o.f.	I_{fit}	χ^2/d.o.f.
$12^3 \times 24$	15.6	-1.2	[8, 11]	2.83	[9, 11]	1.07	–	–
$12^3 \times 24$	15.6	-1.21	[9, 11]	1.73	[8, 11]	4.95	–	–
$12^3 \times 24$	15.6	-1.22	[9, 11]	0.31	[8, 11]	0.43	[5, 8]	2.72
$12^3 \times 24$	15.6	-1.23	[9, 11]	4.54	[8, 11]	2.35	–	–
$12^3 \times 24$	15.6	-1.24	[8, 11]	6.39	[8, 10]	3.66	–	–
$16^3 \times 32$	16.1	-1.12	[13, 15]	0.56	[10, 13]	0.56	–	–
$16^3 \times 32$	16.1	-1.13	[12, 15]	1.06	[10, 13]	0.45	[7, 10]	0.68
$16^3 \times 32$	16.1	-1.14	[12, 15]	1.47	[10, 13]	0.04	[7, 10]	0.81
$16^3 \times 32$	16.1	-1.15	[10, 15]	1.81	[10, 13]	2.98	–	–
$16^3 \times 32$	16.1	-1.16	[10, 15]	1.28	[9, 15]	1.37	–	–
$20^3 \times 40$	16.5	-1.07	[14, 19]	0.67	[14, 18]	0.32	[10, 15]	1.55
$20^3 \times 40$	16.5	-1.08	[16, 19]	0.69	[13, 16]	1.72	[9, 11]	4.21
$20^3 \times 40$	16.5	-1.09	[15, 19]	3.96	[12, 18]	0.75	–	–
$20^3 \times 40$	16.5	-1.10	[16, 19]	0.60	[12, 15]	0.30	[7, 11]	0.67
$24^3 \times 48$	16.7	-1.04	[16, 23]	1.50	[20, 23]	0.24	[12, 18]	1.66
$24^3 \times 48$	16.7	-1.05	[18, 23]	1.30	[16, 23]	0.51	[10, 16]	0.10
$24^3 \times 48$	16.7	-1.055	[17, 23]	0.83	[16, 23]	0.09	[10, 13]	0.81
$24^3 \times 48$	16.7	-1.06	[15, 23]	1.28	[17, 23]	1.22	[11, 14]	0.04
$24^3 \times 48$	16.7	-1.065	[20, 23]	1.81	[20, 23]	0.18	[10, 13]	0.38
$24^3 \times 48$	16.7	-1.07	[20, 23]	1.44	[12, 14]	3.06	[8, 10]	0.05
$30^3 \times 60$	17.1	-1.005	[26, 29]	1.09	[18, 28]	1.01	[14, 17]	0.72
$30^3 \times 60$	17.1	-1.01	[19, 29]	1.42	[16, 23]	0.72	[12, 15]	2.01
$30^3 \times 60$	17.1	-1.015	[17, 29]	1.34	[20, 28]	0.73	[11, 14]	7.65
$30^3 \times 60$	17.1	-1.02	[23, 29]	0.80	[16, 21]	2.84	[10, 13]	0.94

Table 4.13: $Sp(6)$ meson fit ranges and reduced chi-squares in the antisymmetric representation. The '–' symbol denotes a case in which no reliable signal was detected.

$Sp(6)$ antisymmetric fermions								
Volume	β	am_0	Scalar		Tensor		Axial-tensor	
			I_{fit}	χ^2/d.o.f.	I_{fit}	χ^2/d.o.f.	I_{fit}	χ^2/d.o.f.
$12^3 \times 24$	15.6	-1.2	[6, 9]	1.89	[8, 11]	1.14	–	–
$12^3 \times 24$	15.6	-1.21	[6, 9]	1.83	[7, 11]	0.82	–	–
$12^3 \times 24$	15.6	-1.22	[6, 9]	2.14	[8, 11]	0.53	–	–
$12^3 \times 24$	15.6	-1.23	–	–	[8, 11]	0.55	–	–
$12^3 \times 24$	15.6	-1.24	[9, 11]	3.40	[7, 10]	1.31	–	–
$16^3 \times 32$	16.1	-1.12	[8, 11]	1.44	[11, 14]	0.08	[6, 9]	0.36
$16^3 \times 32$	16.1	-1.13	[7, 11]	1.24	[12, 15]	0.15	[7, 9]	0.81
$16^3 \times 32$	16.1	-1.14	[7, 10]	1.04	[11, 14]	0.20	[6, 9]	1.71
$16^3 \times 32$	16.1	-1.15	–	–	[8, 15]	1.24	–	–
$16^3 \times 32$	16.1	-1.16	–	–	[7, 10]	0.59	–	–
$20^3 \times 40$	16.5	-1.07	[9, 16]	0.35	[11, 19]	0.25	[9, 12]	1.00
$20^3 \times 40$	16.5	-1.08	[10, 14]	2.57	[12, 19]	0.86	[9, 12]	0.73
$20^3 \times 40$	16.5	-1.09	–	–	[13, 18]	0.35	[9, 11]	0.02
$20^3 \times 40$	16.5	-1.10	–	–	[8, 11]	1.31	–	–
$24^3 \times 48$	16.7	-1.04	[12, 17]	0.78	[12, 22]	1.09	[9, 11]	0.24
$24^3 \times 48$	16.7	-1.05	[9, 12]	1.72	[14, 23]	0.36	[9, 12]	1.06
$24^3 \times 48$	16.7	-1.055	[11, 15]	1.62	[11, 16]	0.98	[9, 12]	0.33
$24^3 \times 48$	16.7	-1.06	[9, 13]	2.09	[16, 23]	0.19	[9, 12]	2.18
$24^3 \times 48$	16.7	-1.065	[8, 11]	4.11	[12, 18]	1.37	[8, 10]	1.15
$24^3 \times 48$	16.7	-1.07	–	–	[10, 14]	1.61	–	–
$30^3 \times 60$	17.1	-1.005	[14, 20]	0.79	[16, 29]	0.82	[11, 14]	0.13
$30^3 \times 60$	17.1	-1.01	[14, 18]	0.47	[15, 27]	1.35	[11, 14]	0.29
$30^3 \times 60$	17.1	-1.015	–	–	[13, 24]	0.80	[9, 11]	3.30
$30^3 \times 60$	17.1	-1.02	–	–	[11, 16]	1.07	–	–

Table 4.14: $Sp(6)$ meson fit ranges and reduced chi-squares in the antisymmetric representation. The '–' symbol denotes a case in which no reliable signal was detected.

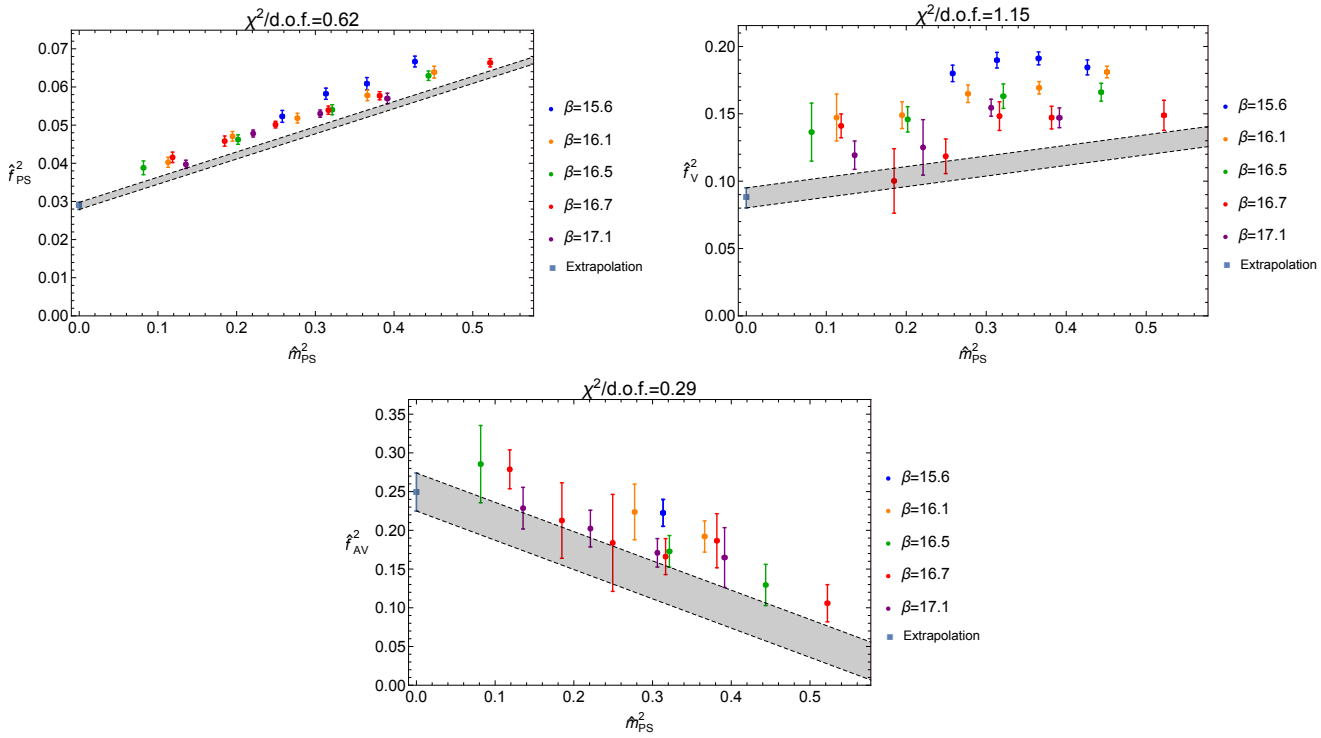

Figure 4.11: Decay constants squared for PS, V and AV channels, comprised of fermions in the antisymmetric representation of $Sp(6)$. The reduced chi-squared value is printed at the top of each plot. Data points in the pink shaded region are not included in the curve-fitting procedure. The grey band represents the continuum and massless extrapolation with the blue square being the observable in the chiral limit and the vertical width corresponding to the statistical error. In instances where a reliable extrapolation cannot be made, no grey band is shown. All quantities are expressed in units of gradient flow scale, w_0.

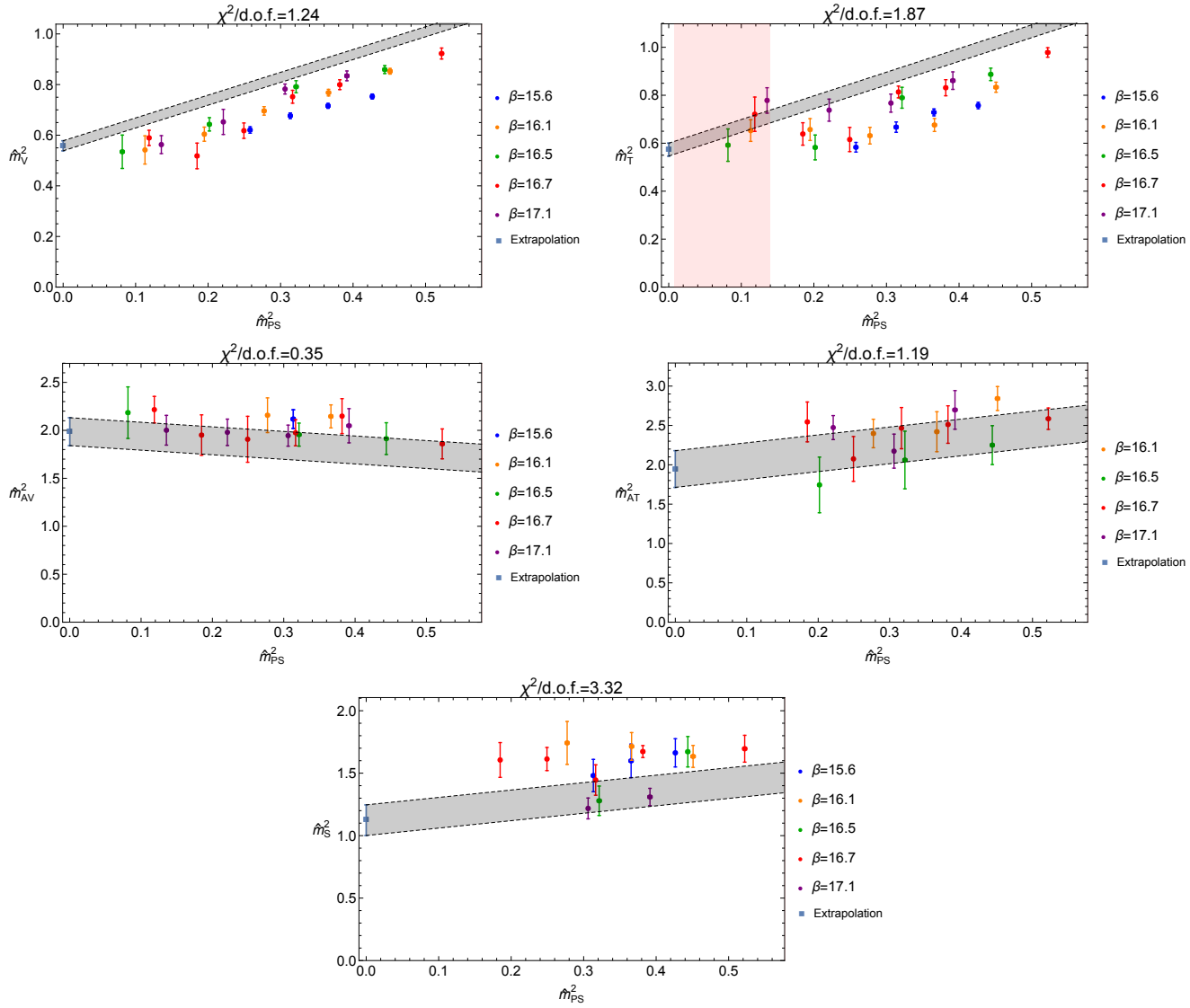

Figure 4.12: Masses squared for V, T, AV, AT and S channels, comprised of fermions in the antisymmetric representation of $Sp(6)$. The reduced chi-squared value is printed at the top of each plot. Data points in the pink shaded region are not included in the curve-fitting procedure. The grey band represents the continuum and massless extrapolation with the blue square being the observable in the chiral limit and the vertical width corresponding to the statistical error. In instances where a reliable extrapolation cannot be made, no grey band is shown. All quantities are expressed in units of gradient flow scale, w_0.

$Sp(6)$ symmetric fermions								
Volume	β	am_0	Pseudoscalar		Vector		Axial-vector	
			I_{fit}	χ^2/d.o.f.	I_{fit}	χ^2/d.o.f.	I_{fit}	χ^2/d.o.f.
$12^3 \times 24$	15.6	-1.51	[8, 11]	2.03	[8, 11]	0.76	–	–
$12^3 \times 24$	15.6	-1.52	[8, 11]	0.54	[7, 10]	1.22	–	–
$12^3 \times 24$	15.6	-1.53	[8, 11]	1.55	[7, 11]	0.98	–	–
$16^3 \times 32$	16.1	-1.36	[11, 15]	4.73	[11, 14]	7.09	[7, 10]	0.08
$16^3 \times 32$	16.1	-1.37	[12, 15]	1.29	[12, 15]	0.68	[7, 10]	1.59
$16^3 \times 32$	16.1	-1.38	[11, 15]	1.12	[12, 15]	1.25	–	–
$16^3 \times 32$	16.1	-1.39	[12, 15]	1.69	[10, 14]	0.13	[7, 10]	0.11
$16^3 \times 32$	16.1	-1.40	[11, 14]	0.47	[12, 15]	0.54	–	–
$16^3 \times 32$	16.1	-1.41	[12, 15]	0.82	[11, 14]	0.74	–	–
$16^3 \times 32$	16.1	-1.42	[11, 15]	0.95	[10, 15]	0.43	[7, 9]	0.19
$16^3 \times 32$	16.1	-1.43	[11, 15]	1.67	[9, 13]	0.19	–	–
$20^3 \times 40$	16.5	-1.30	[14, 19]	1.32	[16, 19]	1.61	[11, 14]	0.74
$20^3 \times 40$	16.5	-1.32	[15, 19]	1.63	[15, 18]	0.75	[9, 11]	0.04
$20^3 \times 40$	16.5	-1.33	[14, 19]	1.47	[14, 17]	0.67	[8, 11]	1.50
$20^3 \times 40$	16.5	-1.34	[14, 19]	1.57	[14, 19]	1.48	[7, 9]	4.13
$20^3 \times 40$	16.5	-1.35	[14, 19]	0.61	[14, 17]	0.03	[8, 11]	1.94
$24^3 \times 48$	16.7	-1.31	[17, 22]	1.34	[14, 23]	1.57	[8, 13]	0.48
$24^3 \times 48$	16.7	-1.315	[16, 23]	1.23	[13, 22]	0.45	[9, 12]	1.81
$24^3 \times 48$	16.7	-1.32	[15, 23]	0.93	[14, 23]	0.25	[10, 12]	0.21
$24^3 \times 48$	16.7	-1.325	[16, 23]	1.23	[15, 23]	0.39	[8, 11]	1.58
$30^3 \times 60$	17.1	-1.24	[19, 29]	1.35	[21, 28]	1.72	[11, 14]	0.86
$30^3 \times 60$	17.1	-1.245	[20, 29]	1.02	[16, 29]	1.03	[11, 17]	0.42
$30^3 \times 60$	17.1	-1.25	[18, 27]	1.11	[26, 29]	0.11	[12, 16]	0.55
$30^3 \times 60$	17.1	-1.255	[22, 29]	1.40	[17, 29]	1.26	[12, 18]	0.15
$30^3 \times 60$	17.1	-1.26	[20, 29]	1.13	[22, 29]	1.68	[10, 17]	0.87

Table 4.15: $Sp(6)$ meson fit ranges and reduced chi-squares in the symmetric representation. The '–' symbol denotes a case in which no reliable signal was detected.

$Sp(6)$ symmetric fermions								
Volume	β	am_0	Scalar		Tensor		Axial-tensor	
			I_{fit}	χ^2/d.o.f.	I_{fit}	χ^2/d.o.f.	I_{fit}	χ^2/d.o.f.
$12^3 \times 24$	15.6	-1.51	–	–	[7, 10]	0.11	–	–
$12^3 \times 24$	15.6	-1.52	–	–	[8, 11]	1.17	–	–
$12^3 \times 24$	15.6	-1.53	–	–	[5, 7]	0.83	–	–
$16^3 \times 32$	16.1	-1.36	[8, 11]	0.41	[10, 14]	0.48	[6, 9]	0.45
$16^3 \times 32$	16.1	-1.37	[8, 11]	0.05	[9, 14]	0.66	–	–
$16^3 \times 32$	16.1	-1.38	[7, 10]	0.50	[11, 15]	0.79	[7, 9]	0.05
$16^3 \times 32$	16.1	-1.39	[7, 12]	0.97	[10, 15]	1.49	[5, 8]	1.61
$16^3 \times 32$	16.1	-1.40	[7, 12]	1.44	[12, 15]	0.27	[5, 7]	1.42
$16^3 \times 32$	16.1	-1.41	[6, 9]	0.05	[12, 15]	0.04	–	–
$16^3 \times 32$	16.1	-1.42	[11, 15]	1.73	[8, 13]	0.97	–	–
$16^3 \times 32$	16.1	-1.43	[11, 15]	0.97	[8, 11]	0.73	–	–
$20^3 \times 40$	16.5	-1.30	[12, 15]	0.19	[12, 19]	0.82	[9, 12]	0.02
$20^3 \times 40$	16.5	-1.32	[9, 14]	1.60	[11, 17]	0.81	[8, 11]	0.75
$20^3 \times 40$	16.5	-1.33	[9, 13]	0.15	[12, 17]	0.27	–	–
$20^3 \times 40$	16.5	-1.34	[10, 14]	0.96	[12, 17]	0.15	–	–
$20^3 \times 40$	16.5	-1.35	[8, 11]	0.88	[11, 19]	0.70	–	–
$24^3 \times 48$	16.7	-1.31	[10, 14]	1.03	[16, 23]	0.69	–	–
$24^3 \times 48$	16.7	-1.315	[12, 14]	0.16	[15, 23]	1.69	[7, 10]	1.23
$24^3 \times 48$	16.7	-1.32	[8, 12]	2.00	[16, 20]	0.04	–	–
$24^3 \times 48$	16.7	-1.325	[9, 14]	0.37	[11, 18]	1.69	[7, 9]	0.26
$30^3 \times 60$	17.1	-1.24	–	–	[19, 27]	0.49	[10, 13]	0.69
$30^3 \times 60$	17.1	-1.245	[11, 16]	0.41	[14, 28]	1.02	[9, 14]	0.86
$30^3 \times 60$	17.1	-1.25	[11, 15]	0.38	[18, 29]	1.46	[9, 13]	0.20
$30^3 \times 60$	17.1	-1.255	[14, 18]	0.14	[25, 28]	0.31	[11, 14]	0.15
$30^3 \times 60$	17.1	-1.26	[10, 14]	2.75	[15, 29]	1.14	[9, 13]	0.56

Table 4.16: $Sp(6)$ meson fit ranges and reduced chi-squares in the symmetric representation. The '–' symbol denotes a case in which no reliable signal was detected.

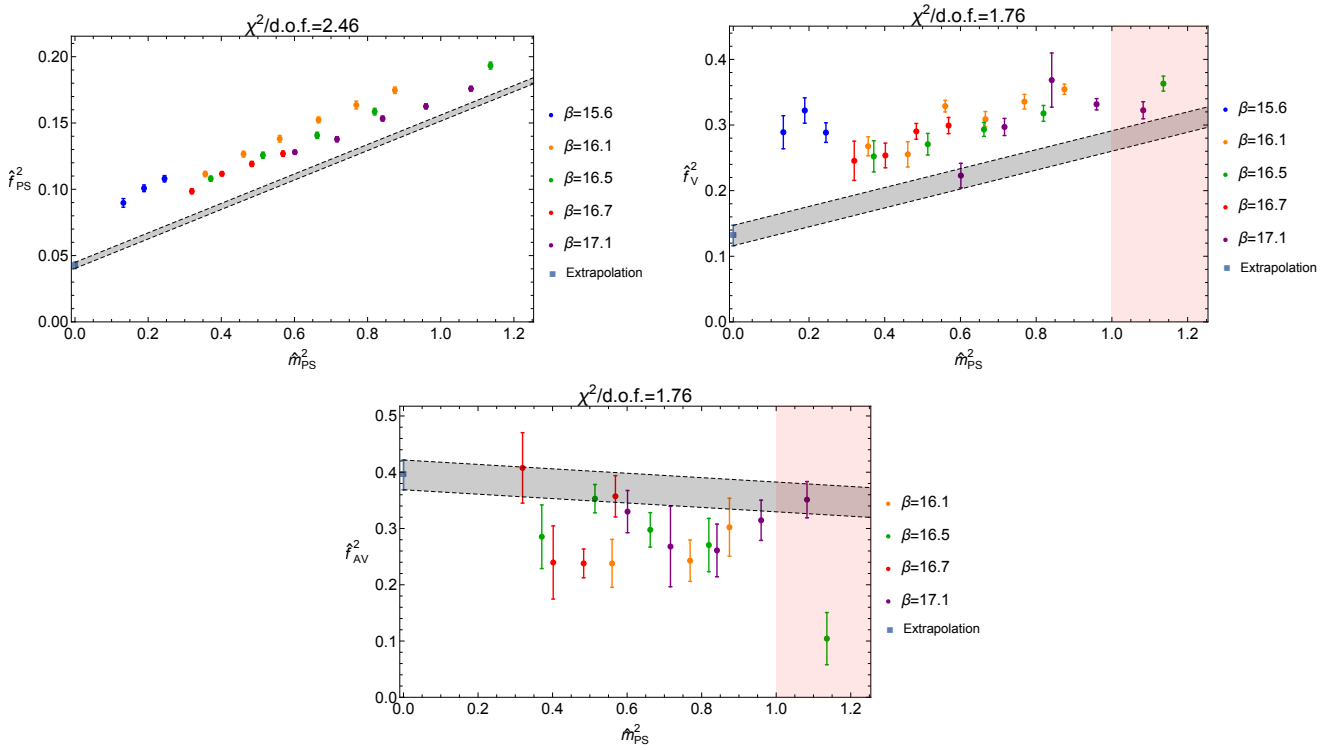

Figure 4.13: Decay constants squared for PS, V and AV channels, comprised of fermions in the symmetric representation of $Sp(6)$. The reduced chi-squared value is printed at the top of each plot. Data points in the pink shaded region are not included in the curve-fitting procedure. The grey band represents the continuum and massless extrapolation with the blue square being the observable in the chiral limit and the vertical width corresponding to the statistical error. In instances where a reliable extrapolation cannot be made, no grey band is shown. All quantities are expressed in units of gradient flow scale, w_0.

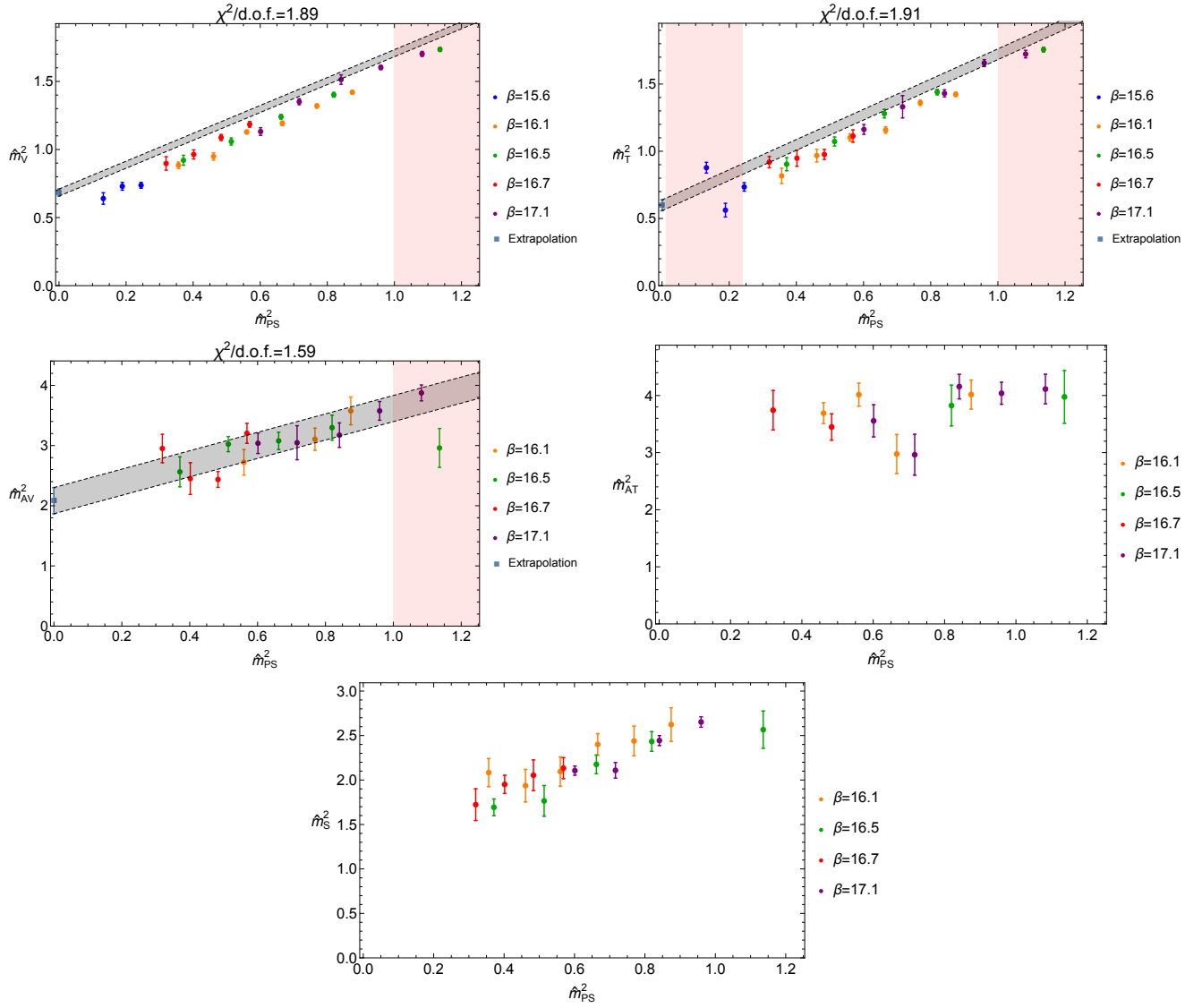

Figure 4.14: Masses squared for V, T, AV, AT and S channels, comprised of fermions in the symmetric representation of $Sp(6)$. The reduced chi-squared value is printed at the top of each plot. Data points in the pink shaded region are not included in the curve-fitting procedure. The grey band represents the continuum and massless extrapolation with the blue square being the observable in the chiral limit and the vertical width corresponding to the statistical error. In instances where a reliable extrapolation cannot be made, no grey band is shown. All quantities are expressed in units of gradient flow scale, w_0.

4.6 Discussion

In this chapter, we have provided a first determination of how the quenched meson spectrum of $Sp(2N)$ Yang-Mills varies with N and with the representation. It will also serve as a benchmark for model building and for future calculations with dynamical fermions.

The calculations for the quenched meson spectrum for $Sp(4)$ in the fundamental and antisymmetric representations show agreement with same in [13]. Our extrapolations generally show a good value of reduced chi-squared when such extrapolations could reliably be done. These comparisons are plotted in figs. 4.15 and 4.16 for fundamental and antisymmetric fermions, respectively. We also compare our chiral results for $Sp(4)$ and $Sp(6)$ for fixed representations in figs. 4.21 to 4.26. For the $Sp(4)$ data we observe that each chiral observable increases as we go from the fundamental to the antisymmetric to the symmetric representation.

The results could be improved by the addition of more statistics. Taking the same measurements from more configurations will supply a more accurate estimate of the mean and the error of each lattice result. As well as more configurations, we could supplement our results with measurements from larger β values in order to obtain more accurate results in our continuum extrapolations. In addition, computations at lighter masses should supply a more accurate extrapolation to the chiral limit; however, the closer we are to the chiral limit, the more expensive the computations become. Therefore, this calculation, as well as other computationally intensive studies is deferred to future investigations.

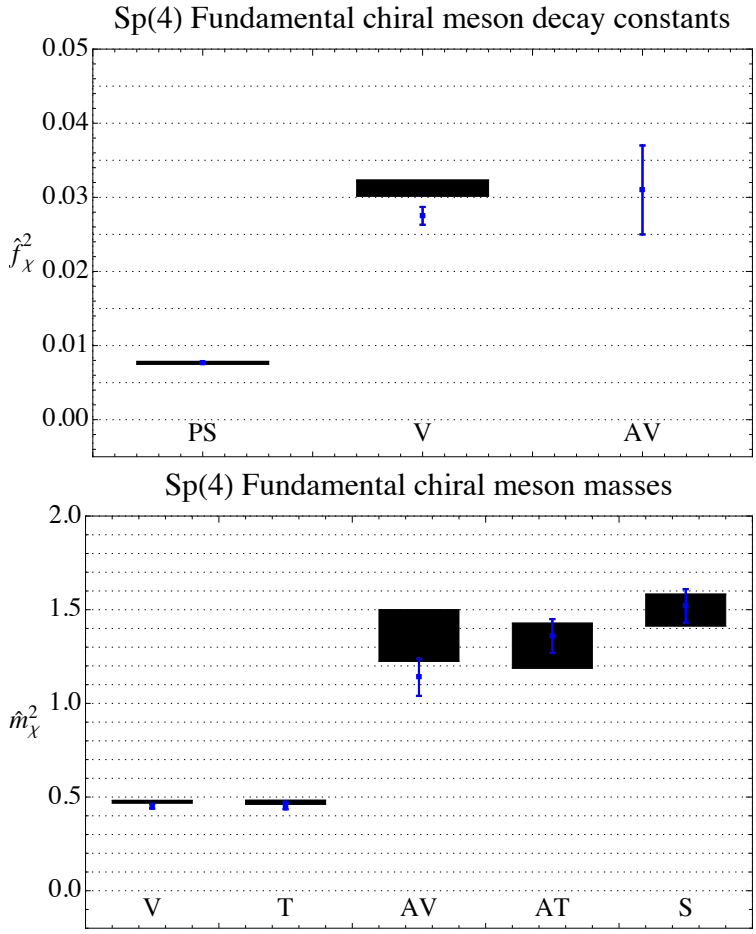

Figure 4.15: Masses and decay constants squared for mesons comprised of fermions in the fundamental representation of $Sp(4)$. The black boxes denote results computed for this thesis. Blue dots are the corresponding results from [13]. For both sets of data, the vertical width corresponds to the statistical error in the measurement. All quantities are expressed in units of gradient flow scale, w_0.

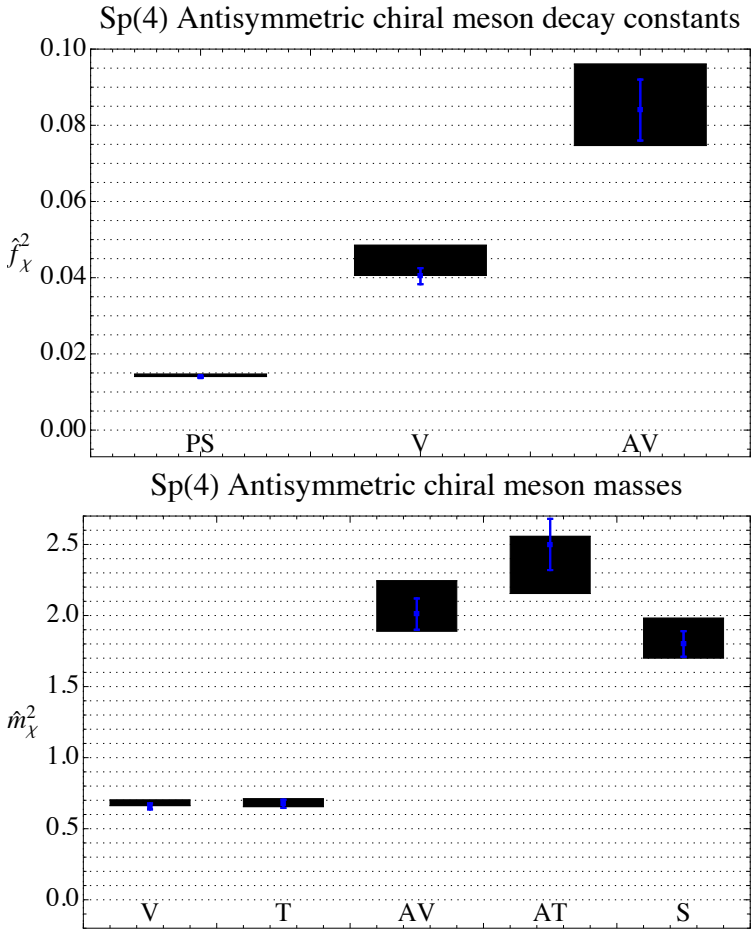

Figure 4.16: Masses and decay constants squared for mesons comprised of fermions in the antisymmetric representation of $Sp(4)$. The black boxes denote results computed for this thesis. Blue dots are the corresponding results from [13]. For both sets of data, the vertical width corresponds to the statistical error in the measurement. All quantities are expressed in units of gradient flow scale, w_0.

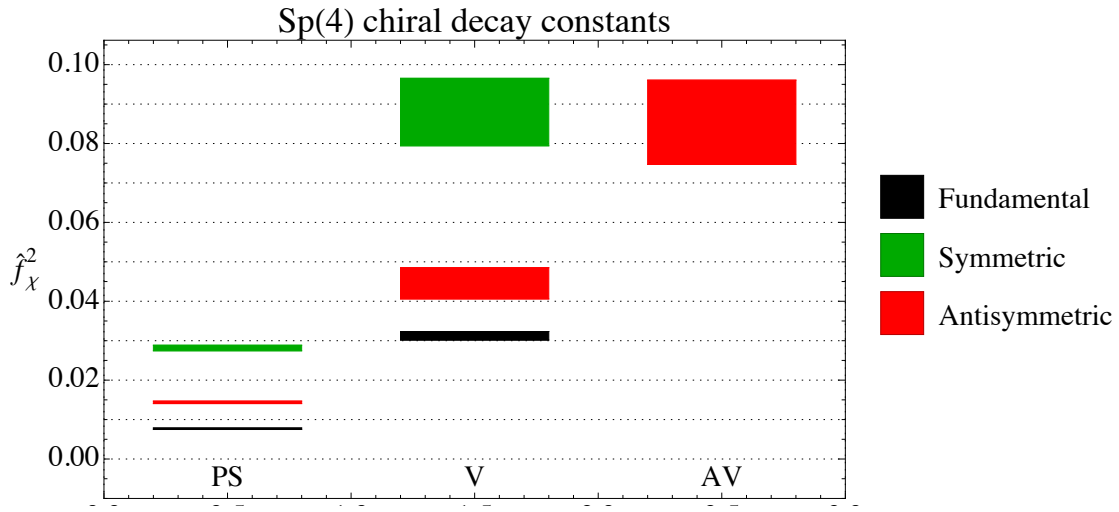

Figure 4.17: $Sp(4)$ chiral decay constants squared for fundamental, symmetric and antisymmetric fermions expressed in units of gradient flow.

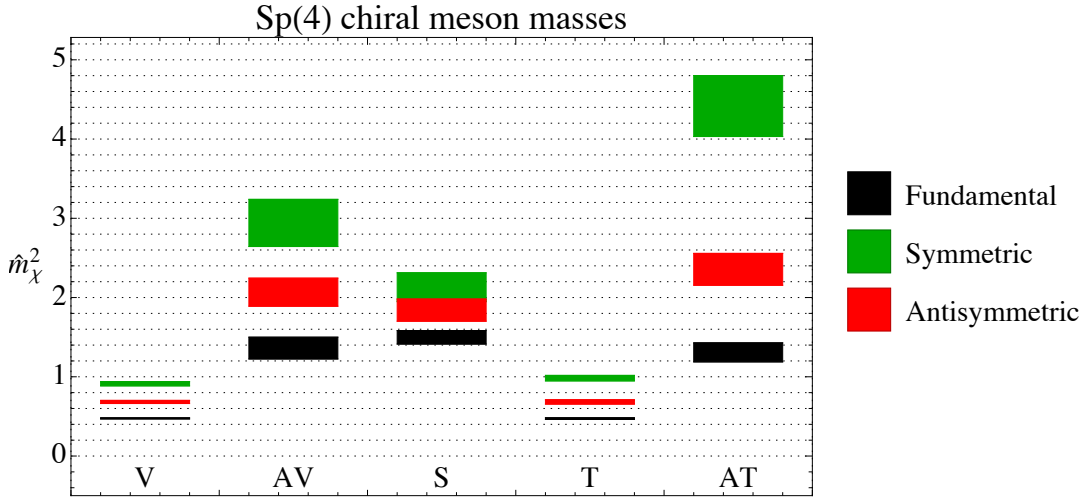

Figure 4.18: $Sp(4)$ chiral masses squared for fundamental, symmetric and antisymmetric fermions expressed in units of gradient flow.

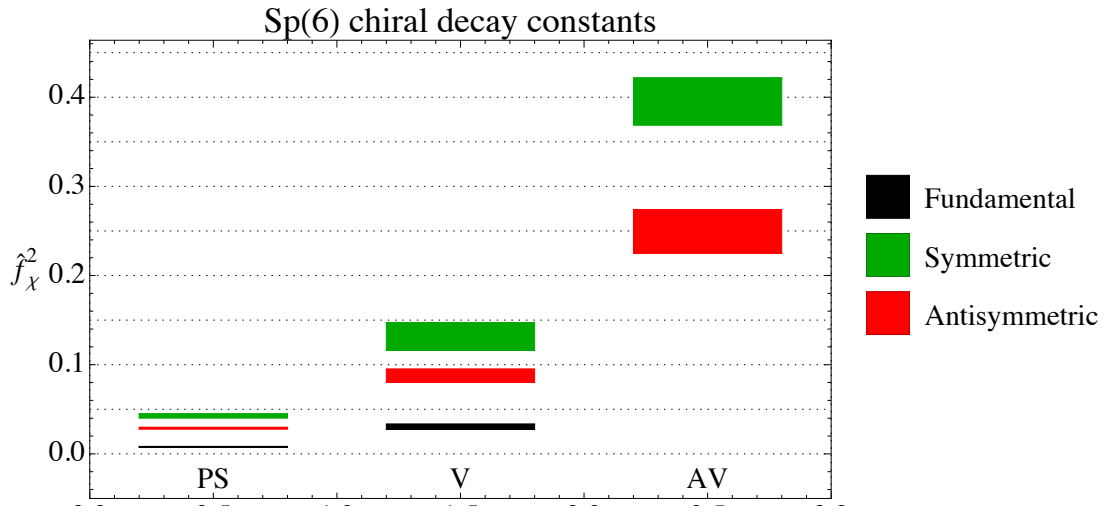

Figure 4.19: $Sp(6)$ chiral decay constants squared for fundamental, symmetric and antisymmetric fermions expressed in units of gradient flow.

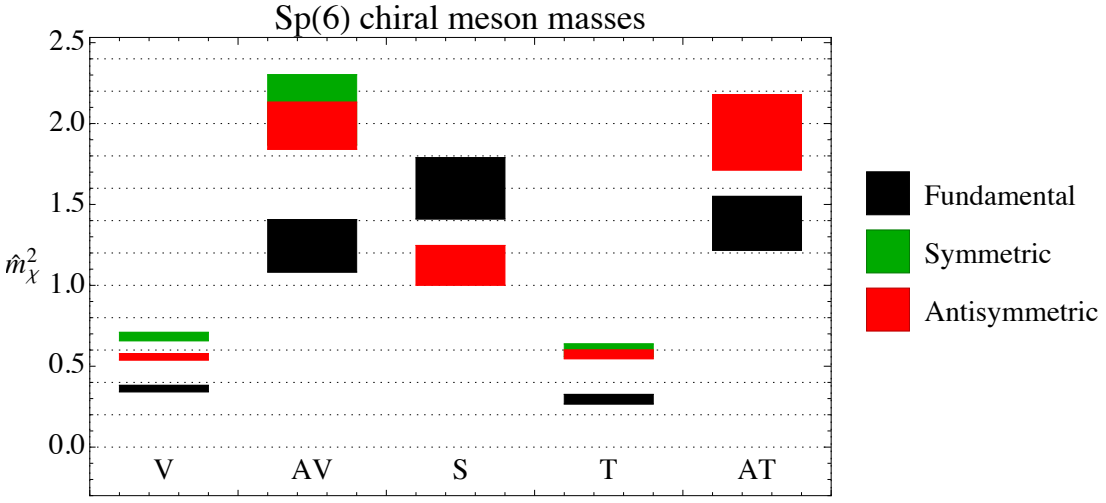

Figure 4.20: $Sp(6)$ chiral masses squared for fundamental, symmetric and antisymmetric fermions expressed in units of gradient flow.

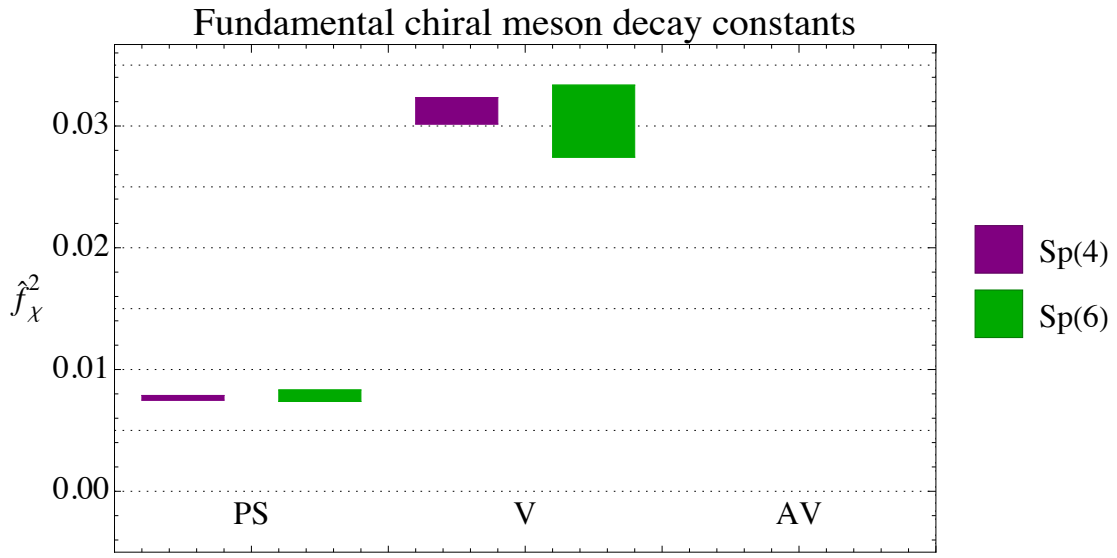

Figure 4.21: Chiral decay constants squared for fundamental fermions expressed in units of gradient flow for $Sp(4)$ and $Sp(6)$.

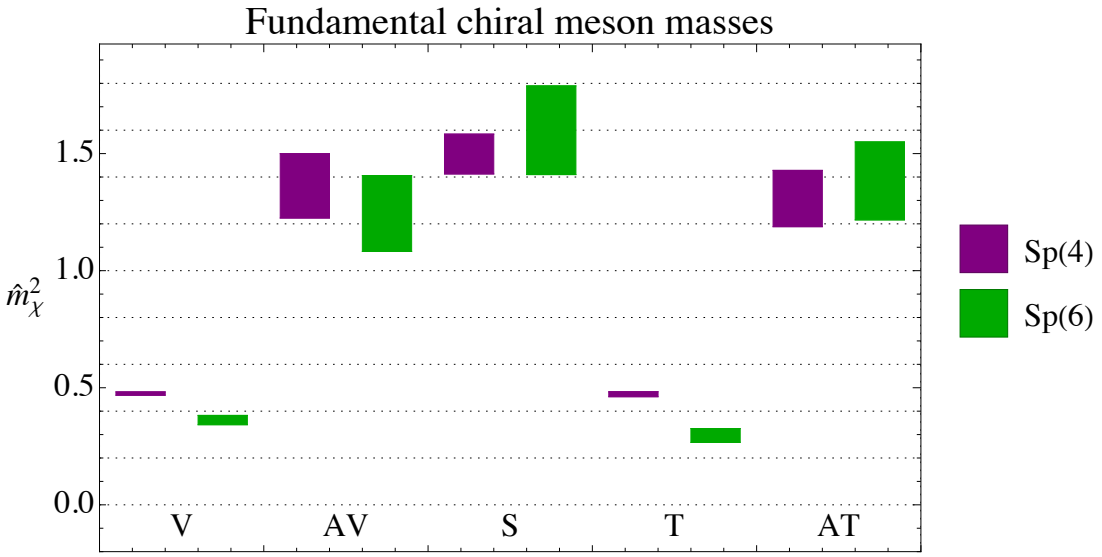

Figure 4.22: Chiral masses squared for fundamental fermions expressed in units of gradient flow for $Sp(4)$ and $Sp(6)$.

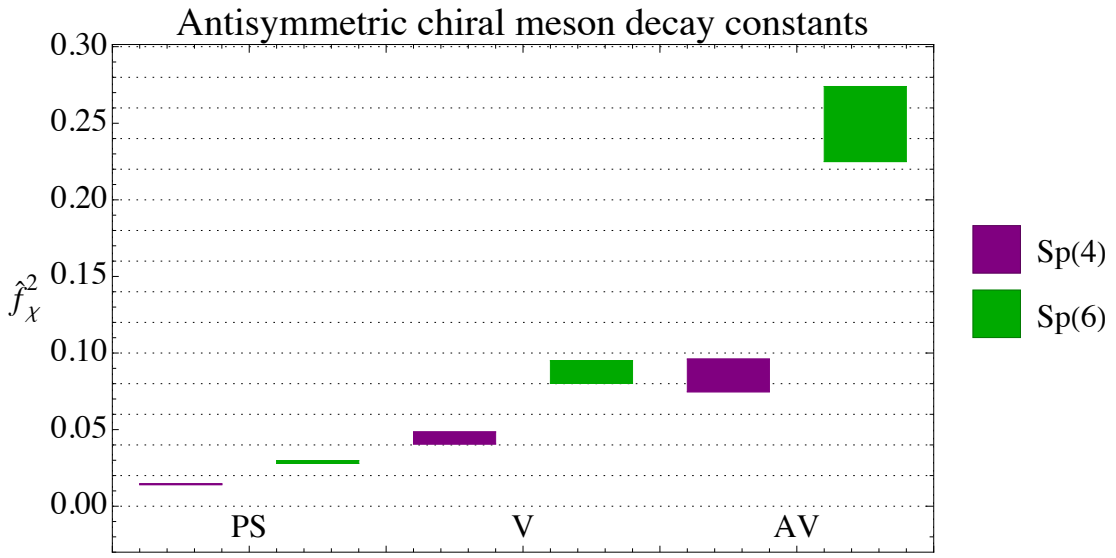

Figure 4.23: Chiral decay constants squared for antisymmetric fermions expressed in units of gradient flow for $Sp(4)$ and $Sp(6)$.

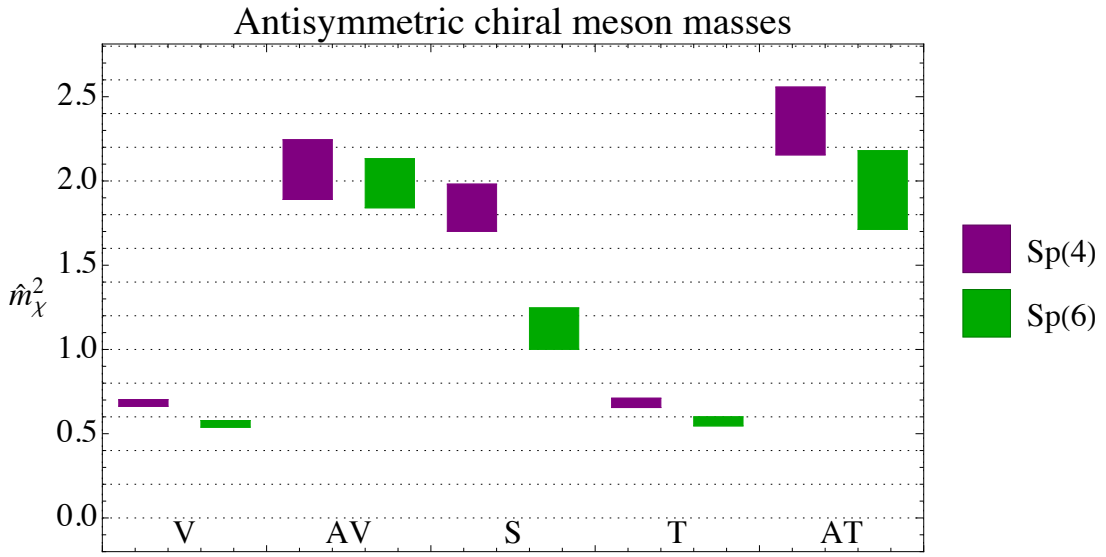

Figure 4.24: Chiral masses squared for antisymmetric fermions expressed in units of gradient flow for $Sp(4)$ and $Sp(6)$.

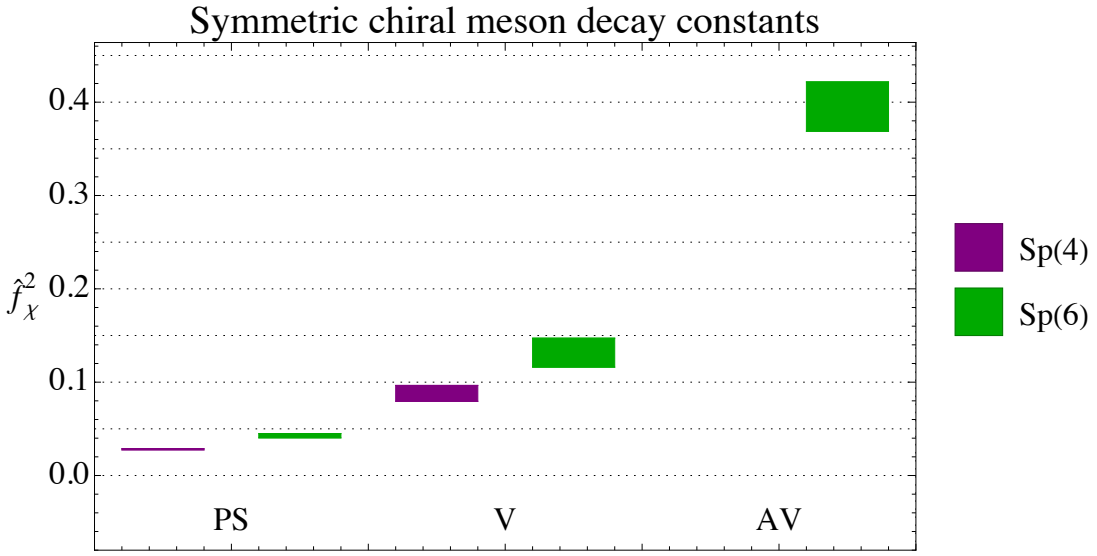

Figure 4.25: Chiral decay constants squared for fundamental fermions expressed in units of gradient flow for $Sp(4)$ and $Sp(6)$.

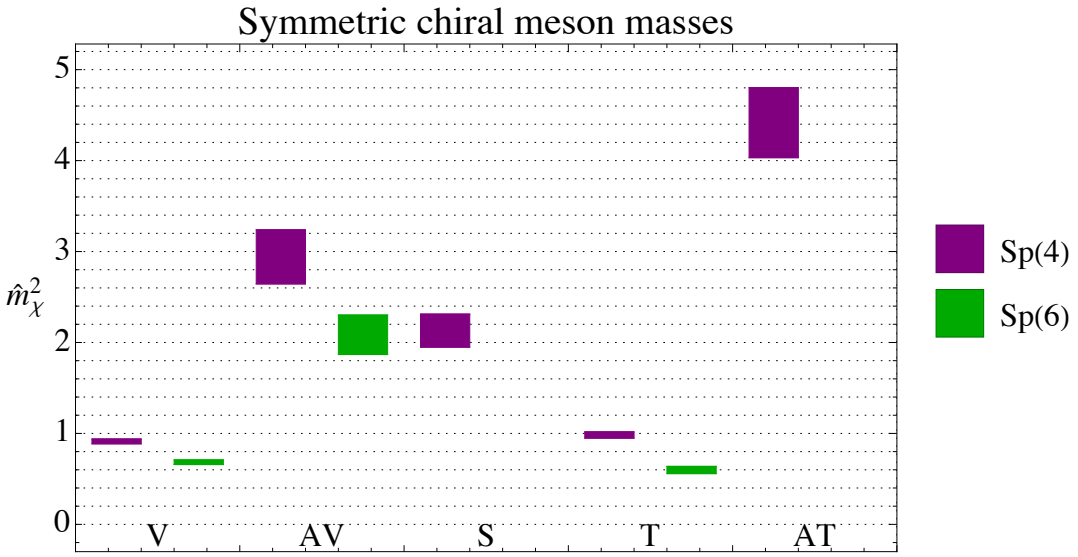

Figure 4.26: Chiral masses squared for fundamental fermions expressed in units of gradient flow for $Sp(4)$ and $Sp(6)$.

Chapter 5

Conclusion

Throughout this thesis we have focussed on the non-perturbative physics of $Sp(2N)$ Yang-Mills theories. In Chapter 3, we studied the glueball spectrum of $Sp(2N)$ Yang-Mills theories both for finite N and in the limit $N \to \infty$. In Chapter 4, we studied the quenched meson spectrum for $N = 2$ and $N = 3$ as a stepping-stone to a large-N extrapolation for the same observables. Both these values of N were examined separately for fermions in the fundamental, symmetric and antisymmetric representations (with the adjoint representation of $Sp(2N)$ being identical to the corresponding symmetric representation).

By the existence of torelon states found in our glueball calculations, we demonstrated that $Sp(4)$, $Sp(6)$ and $Sp(8)$ gauge theories confine. This both confirms and extends the work done in [56]. Confirming confinement is of great significance since there is no known way to prove this analytically. We also found good agreement between our data for the glueball spectrum of $Sp(2)$ and results in the literature for $SU(2)$. The same can be said of our $Sp(\infty)$ data compared to existing data for $SU(\infty)$.

We also examine our glueball results in the context of large-N universality.

Specifically, Casimir scaling and the mass ratio of the two states 2^{++} and 0^{++}; these are the continuum states of E^{++} and A_1^{++}, respectively. Some of the behaviour of $Sp(2N)$ and $SU(N)$ Yang-Mills as N varies is captured by fig. 3.9. Additionally, we find numerical evidence for the ratio in eq. (3.9.1) being common to all $Sp(2N)$ groups. We also find good agreement between our $Sp(4)$ results in the fundamental and antisymmetric representations and those contained in [13].

Our studies of the quenched meson spectrum for $Sp(4)$ and $Sp(6)$ are a work in progress for the quenched meson spectrum as $N \to \infty$. The sets of results for the two groups that we do have are a qualitatively similar behaviour of the spectrum for all representations in both cases which may hint towards a mild dependence on N. If confirmed by unquenched studies, this observation can have relevant implications for the question concerning the influence of N on the dynamics of $Sp(2N)$.

This work can also be considered a first step towards a first-principle computation of the Higgs mass in the new interaction, which was our original motive for studying $Sp(2N)$ groups. The mass of the pseudoscalar as computed in Chapter 4 is a composite state in which the $SU(2) \otimes U(1)$ symmetry is global and exact. In the SM, this same symmetry (the electroweak symmetry) is spontaneously broken to a $U(1)$ subgroup and the Higgs boson is a scalar fluctuation about this non-trivial vacuum. To compute the Higgs mass in the new interaction would require, in addition to unquenching, gauging a subgroup of the unbroken residual global symmetry corresponding to the SM.

The motives for studying $Sp(2N)$ gauge groups are not limited to composite Higgs models. In fact, it has been suggested that $Sp(2N)$ glueballs could play a role in dark matter scenarios [86]. In addition, the pseudo-reality of the gauge group allows us to study the finite density without having to confront the sign-problem. (For an overview of the sign-problem, see, e.g., [87].) Contrasting and comparing the behaviour of $Sp(2N)$ and of $SU(N)$ at finite density can therefore provide useful insights to

understand this regime in QCD. Combined with the universality of the large-N limit, we can determine the behaviour as a function of the chemical potential of $SU(N)$ and $SO(N)$ groups in the same limit.

Appendix A

SU(4) and *Sp(4)* generators

The following matrices are generators of $Sp(4)$ [54]:

$$T^6 = \frac{1}{2\sqrt{2}} \begin{bmatrix} 0 & 0 & -i & 0 \\ 0 & 0 & 0 & -i \\ i & 0 & 0 & 0 \\ 0 & i & 0 & 0 \end{bmatrix}, \quad T^7 = \frac{1}{2\sqrt{2}} \begin{bmatrix} 0 & 0 & 0 & -i \\ 0 & 0 & -i & 0 \\ 0 & i & 0 & 0 \\ i & 0 & 0 & 0 \end{bmatrix}, \quad T^8 = \frac{1}{2\sqrt{2}} \begin{bmatrix} 0 & -i & 0 & 0 \\ i & 0 & 0 & 0 \\ 0 & 0 & 0 & -i \\ 0 & 0 & i & 0 \end{bmatrix},$$

$$T^9 = \frac{1}{2\sqrt{2}} \begin{bmatrix} 0 & 0 & -i & 0 \\ 0 & 0 & 0 & i \\ i & 0 & 0 & 0 \\ 0 & -i & 0 & 0 \end{bmatrix}, \quad T^{10} = \frac{1}{2} \begin{bmatrix} 0 & 0 & 1 & 0 \\ 0 & 0 & 0 & 0 \\ 1 & 0 & 0 & 0 \\ 0 & 0 & 0 & 0 \end{bmatrix}, \quad T^{11} = \frac{1}{2\sqrt{2}} \begin{bmatrix} 0 & 0 & 0 & 1 \\ 0 & 0 & 1 & 0 \\ 0 & 1 & 0 & 0 \\ 1 & 0 & 0 & 0 \end{bmatrix},$$

$$T^{12} = \frac{1}{2} \begin{bmatrix} 0 & 0 & 0 & 0 \\ 0 & 0 & 0 & 1 \\ 0 & 0 & 0 & 0 \\ 0 & 1 & 0 & 0 \end{bmatrix}, \quad T^{13} = \frac{1}{2\sqrt{2}} \begin{bmatrix} 0 & 1 & 0 & 0 \\ 1 & 0 & 0 & 0 \\ 0 & 0 & 0 & -1 \\ 0 & 0 & -1 & 0 \end{bmatrix}, \quad T^{14} = \frac{1}{2\sqrt{2}} \begin{bmatrix} 1 & 0 & 0 & 0 \\ 0 & -1 & 0 & 0 \\ 0 & 0 & -1 & 0 \\ 0 & 0 & 0 & 1 \end{bmatrix},$$

$$T^{15} = \frac{1}{2\sqrt{2}} \begin{bmatrix} 1 & 0 & 0 & 0 \\ 0 & 1 & 0 & 0 \\ 0 & 0 & -1 & 0 \\ 0 & 0 & 0 & -1 \end{bmatrix}.$$

The fifteen generators of $SU(4)$ are the ten matrices stated above in combination with the following five [54]:

$$T^1 = \tfrac{1}{2\sqrt{2}} \begin{bmatrix} 0 & 1 & 0 & 0 \\ 1 & 0 & 0 & 0 \\ 0 & 0 & 0 & 1 \\ 0 & 0 & 1 & 0 \end{bmatrix}, \quad T^2 = \tfrac{1}{2\sqrt{2}} \begin{bmatrix} 0 & -i & 0 & 0 \\ i & 0 & 0 & 0 \\ 0 & 0 & 0 & i \\ 0 & 0 & -i & 0 \end{bmatrix}, \quad T^3 = \tfrac{1}{2\sqrt{2}} \begin{bmatrix} 1 & 0 & 0 & 0 \\ 0 & -1 & 0 & 0 \\ 0 & 0 & 1 & 0 \\ 0 & 0 & 0 & -1 \end{bmatrix},$$

$$T^4 = \tfrac{1}{2\sqrt{2}} \begin{bmatrix} 0 & 0 & 0 & -i \\ 0 & 0 & i & 0 \\ 0 & -i & 0 & 0 \\ i & 0 & 0 & 0 \end{bmatrix}, \quad T^5 = \tfrac{1}{2\sqrt{2}} \begin{bmatrix} 0 & 0 & 0 & 1 \\ 0 & 0 & -1 & 0 \\ 0 & -1 & 0 & 0 \\ 1 & 0 & 0 & 0 \end{bmatrix}.$$

The two groups are

$$SU(4) = \{e^{i\alpha^a T^a} : a = 1, \ldots, 15\} \tag{A.0.1}$$

$$Sp(4) = \{e^{i\alpha^a T^a} : a = 6, \ldots, 15\}. \tag{A.0.2}$$

All matrices are normalised such that $\operatorname{tr} T^a T^b = \frac{1}{2}\delta^{ab}$.

The $SU(4)$ generators written as generalised Gell-Mann matrices are stated be-

low but are less useful for our study of symmetry breaking to $Sp(4)$.

$$\lambda^1 = \begin{bmatrix} 0 & 1 & 0 & 0 \\ 1 & 0 & 0 & 0 \\ 0 & 0 & 0 & 0 \\ 0 & 0 & 0 & 0 \end{bmatrix}, \quad \lambda^2 = \begin{bmatrix} 0 & -i & 0 & 0 \\ i & 0 & 0 & 0 \\ 0 & 0 & 0 & 0 \\ 0 & 0 & 0 & 0 \end{bmatrix}, \quad \lambda^3 = \begin{bmatrix} 1 & 0 & 0 & 0 \\ 0 & -1 & 0 & 0 \\ 0 & 0 & 0 & 0 \\ 0 & 0 & 0 & 0 \end{bmatrix},$$

$$\lambda^4 = \begin{bmatrix} 0 & 0 & 1 & 0 \\ 0 & 0 & 0 & 0 \\ 1 & 0 & 0 & 0 \\ 0 & 0 & 0 & 0 \end{bmatrix}, \quad \lambda^5 = \begin{bmatrix} 0 & 0 & -i & 0 \\ 0 & 0 & 0 & 0 \\ i & 0 & 0 & 0 \\ 0 & 0 & 0 & 0 \end{bmatrix}, \quad \lambda^6 = \begin{bmatrix} 0 & 0 & 0 & 0 \\ 0 & 0 & 1 & 0 \\ 0 & 1 & 0 & 0 \\ 0 & 0 & 0 & 0 \end{bmatrix},$$

$$\lambda^7 = \begin{bmatrix} 0 & 0 & 0 & 0 \\ 0 & 0 & -i & 0 \\ 0 & i & 0 & 0 \\ 0 & 0 & 0 & 0 \end{bmatrix}, \quad \lambda^8 = \frac{1}{\sqrt{3}} \begin{bmatrix} 1 & 0 & 0 & 0 \\ 0 & 1 & 0 & 0 \\ 0 & 0 & -2 & 0 \\ 0 & 0 & 0 & 0 \end{bmatrix}, \quad \lambda^9 = \begin{bmatrix} 0 & 0 & 0 & 1 \\ 0 & 0 & 0 & 0 \\ 0 & 0 & 0 & 0 \\ 1 & 0 & 0 & 0 \end{bmatrix},$$

$$\lambda^{10} = \begin{bmatrix} 0 & 0 & 0 & -i \\ 0 & 0 & 0 & 0 \\ 0 & 0 & 0 & 0 \\ i & 0 & 0 & 0 \end{bmatrix}, \quad \lambda^{11} = \begin{bmatrix} 0 & 0 & 0 & 0 \\ 0 & 0 & 0 & 1 \\ 0 & 0 & 0 & 0 \\ 0 & 1 & 0 & 0 \end{bmatrix}, \quad \lambda^{12} = \begin{bmatrix} 0 & 0 & 0 & 0 \\ 0 & 0 & 0 & -i \\ 0 & 0 & 0 & 0 \\ 0 & i & 0 & 0 \end{bmatrix},$$

$$\lambda^{13} = \begin{bmatrix} 0 & 0 & 0 & 0 \\ 0 & 0 & 0 & 0 \\ 0 & 0 & 0 & 1 \\ 0 & 0 & 1 & 0 \end{bmatrix}, \quad \lambda^{14} = \begin{bmatrix} 0 & 0 & 0 & 0 \\ 0 & 0 & 0 & 0 \\ 0 & 0 & 0 & -i \\ 0 & 0 & i & 0 \end{bmatrix}, \quad \lambda^{15} = \frac{1}{\sqrt{6}} \begin{bmatrix} 1 & 0 & 0 & 0 \\ 0 & 1 & 0 & 0 \\ 0 & 0 & 1 & 0 \\ 0 & 0 & 0 & -3 \end{bmatrix}.$$

Appendix B

Block Structure of *Sp(2N)*

Write a generalised $2N \times 2N$ matrix in the block form

$$U = \begin{bmatrix} A & B \\ C & D \end{bmatrix} \tag{B.0.1}$$

where each of A, B, C and D is an $N \times N$ matrix. In order to be an element of $Sp(2N)$, U must satisfy the constraints

$$U^\dagger U = \mathbb{1}_{2N} \tag{B.0.2}$$

$$U^* = \Omega^\dagger U \Omega. \tag{B.0.3}$$

The definition in eq. (1.3.2) can be manipulated into the equivalent form

$$\begin{aligned} U^* &= \Omega^\dagger U \Omega \\ \implies U^T &= \Omega^\dagger U^\dagger \Omega \\ \implies \Omega U^T &= U^\dagger \Omega \end{aligned}$$

$$\implies U\Omega U^T = \Omega \qquad \text{(from the unitarity of } U\text{)}. \tag{B.0.4}$$

Unitarity gives the conditions:

$$A^\dagger A + C^\dagger C = \mathbb{1}_N \tag{B.0.5}$$
$$B^\dagger B + D^\dagger D = \mathbb{1}_N \tag{B.0.6}$$
$$A^\dagger B + C^\dagger D = 0, \tag{B.0.7}$$

and the symplectic condition in eq. (B.0.4) gives

$$AB^T = BA^T \tag{B.0.8}$$
$$CD^T = DC^T \tag{B.0.9}$$
$$AD^T - BC^T = \mathbb{1}_N. \tag{B.0.10}$$

The last of the symplectic conditions combined with the other constraints gives

$$\begin{aligned}
AD^T - BC^T &= \mathbb{1}_N \\
\implies A^*D^\dagger - B^*C^\dagger &= \mathbb{1}_N \\
\implies A^*D^\dagger D - B^*C^\dagger D &= D \\
\implies A^*(\mathbb{1}_N - B^\dagger B) - B^*(-A^\dagger B) &= D \\
\implies A^* - A^*B^\dagger B + B^*A^\dagger B &= D \\
\implies A^* - (A^*B^\dagger - B^*A^\dagger)B &= D \\
\implies A^* - \cancelto{0}{(AB^T - BA^T)}^*B &= D \\
\implies A^* &= D.
\end{aligned} \tag{B.0.11}$$

In addition,

$$\begin{aligned}
A^\dagger A + C^\dagger C &= \mathbb{1}_N \\
\implies A^\dagger A B^T + C^\dagger C B^T &= B^T \\
\implies A^\dagger A B^T + C^\dagger (B C^T)^T &= B^T \\
\implies A^\dagger A B^T + C^\dagger (A D^T - \mathbb{1}_N)^T &= B^T \\
\implies A^\dagger A B^T + C^\dagger D A^T - C^\dagger &= B^T \\
\implies A^\dagger B A^T + C^\dagger D A^T - C^\dagger &= B^T \\
\implies \cancelto{= 0}{(A^\dagger B + C^\dagger D) A^T} - C^\dagger &= B^T \\
\implies -C^\dagger &= B^T \\
\implies C &= -B^* \qquad \text{(B.0.12)}
\end{aligned}$$

These give the final block structure:

$$U = \begin{bmatrix} A & B \\ -B^* & A^* \end{bmatrix} \qquad \text{(B.0.13)}$$

with the simplified constraints:

$$AA^\dagger + BB^\dagger = \mathbb{1}_N \qquad \text{(B.0.14)}$$

$$AB^T = BA^T \qquad \text{(B.0.15)}$$

Appendix C

Plateau Seeking Algorithm

The computation of both the meson spectrum and the glueball spectrum requires the determination of a time interval $[t_1, t_2]$ in which the effective mass as a function of time, $am_{\text{eff}}(t)$, exhibits a plateau. At first sight, this would seem to be quite a subjective process but we can attempt to automate it and, thus, make it less prone to human-error. We anticipate that certain circumstances may require the fit to be done manually but the implementation of the algorithm for the work carried out in this thesis resulted in a great many of the results being determined without the need for human intervention. (In general, the algorithm only failed at small lattice volumes or in channels with large masses compared to the pseudoscalar – typically the axial-vector and axial-tensor states.) It also computed the results in a more reproducible manner as well as making the large number of correlators that had to be analysed a less daunting task. Though the algorithm was only used for the meson spectrum in this work, it is applicable to the computation of the glueball spectrum or, indeed, any computation that involves the determination of a fit range. (Though we use this algorithm to detect plateaux, it could be applied to any problem that involves finding an optimum range across which to fit

data to a curve.) Below, we denote the fit range from initial time t_i to final time t_f by $[t_i, t_f]$ and the chi-squared (not the reduced chi-squared) value in the same interval by $\chi^2(t_i, t_f)$.

1. In order for effective masses to qualify for a plateau, they must, first of all, be both real and positive. If this is not the case, the measurements will not make physical sense. As shown in fig. C.1, there may not be a valid signal across a large portion of the lattice and the measurement must be discarded. However, we should be careful not to exclude results such as those in fig. C.2 in which there is a valid mass signal which, nonetheless, does not persist across the whole temporal width of the lattice. An objective way to determine this is to seek the longest list of consecutive t-values for which $am_{\text{eff}}(t)$ is both real and positive. If this list contains fewer than, say, 40% of the values of am_{eff} fit the above criteria, the results must be done manually.

2. Once we have a list of consecutive values of am_{eff} each of which is both real and positive, the largest t value is used as the provisional value for t_f and the smallest as the provisional value for t_i. We denote these values by t_f^{tmp} and t_i^{tmp}, respectively.

3. With our provisional values t_i^{tmp} and t_f^{tmp}, we hold the latter fixed and increase t_i^{tmp} by one lattice width until at least one of the following conditions is met:

   (a) $\chi^2(t_i^{\text{tmp}} + 1, t_f^{\text{tmp}}) > \chi^2(t_i^{\text{tmp}}, t_f^{\text{tmp}})$;

   (b) $\chi^2(t_i^{\text{tmp}}, t_f^{\text{tmp}})$ falls below the value required for a 10% confidence-of-fit level. This value will depend on the number of degrees of freedom corresponding to the fit range;

(c) The number of t-values is at a prescribed minimum. For example, we may wish the plateau length to consist of no fewer than three t-values. Alternatively, we may demand that the number of degrees of freedom be no less than 1 or some other specified minimum.

Condition 3a corresponds to the effective mass beginning to fluctuate around the corresponding ground-state energy. In some pathological cases, this may occur at very early times, but such fit ranges will have very large χ^2 values and will be superseded in the subsequent steps of this algorithm or, perhaps, the measurement will be discarded entirely. Condition 3b corresponds to our ability to say with a given confidence level that the curve fits the data. This 10% value is not inviolable but is simply used as a starting point. The final of the three conditions, 3c, simply puts a safety net in the algorithm to prevent us fitting too few data points to our model. We may wish to discard results for which only condition 3c is satisfied but the results in this thesis for which this was the case were examined, nonetheless.

4. With our latest values of t_i^{tmp} and t_f^{tmp}, we now examine the fit at neighbouring values of t_i^{tmp} and t_f^{tmp}. For a given value of n, we determine the $\chi^2(t_i^{\text{tmp}}, t_f^{\text{tmp}})$ value for starting values $t_i^{\text{tmp}} \pm 1$, $t_i^{\text{tmp}} \pm 2$, $\ldots$, $t_i^{\text{tmp}} \pm n$ and finishing values $t_f^{\text{tmp}} - 1$, $\ldots$, $t_f^{\text{tmp}} - n$. The value of n depends on the width of the lattice but is usually between 2 and 4. In each case we accept the fit range as a *candidate* if $\chi^2(t_i^{\text{tmp}}, t_f^{\text{tmp}})$ falls below the threshold required for 10% confidence-of-fit. If no such fit range exists for any interval, we repeat the above but seeking only a 5% confidence-of-fit. If there are still no valid fit ranges, the interval must be determined manually (or the result may have to be discarded altogether). Of the

candidate fit ranges, we select the one for which

$$\frac{\chi^2(t_i^{\rm tmp}, t_f^{\rm tmp})}{(\text{d.o.f.})(t_f - t_i + 1)^2} \tag{C.0.1}$$

is minimised. The term, d.o.f. refers to the number of degrees of freedom in the fit. The motive for dividing by $(t_f - t_i + 1)^2$ is to determine the minimum value of the reduced chi-squared while maximising the length of the plateau. The length of the plateau is squared for empirical reasons. When we divided by $(t_f - t_i + 1)$, longer plateaux with acceptable chi-squared values were rejected but in the case of dividing by $(t_f - t_i + 1)^3$, long fit ranges with unacceptably large chi-squared values were used. The exponent of 2 is, again, not final and may be subject to revision.

5. Once we have a fit range $[t_i^{\rm tmp}, t_f^{\rm tmp}]$, we carry out a "robustness-check" to make sure that the end points of the fit range do not influence the value of the fitted mass too significantly. For our fit range $[t_i^{\rm tmp}, t_f^{\rm tmp}]$ with effective mass m_1 and error $\delta(m_1)$, we compute the effective mass m_2 in the range $[t_i^{\rm tmp} + 1, t_f^{\rm tmp}]$ with corresponding error $\delta(m_2)$. If the inequality $|m_1 - m_2| < \delta(m_1)$ holds then the effective mass in the original range is not influenced too severely by its endpoints; the measurement changes within the margin of error. If this is not the case, we reduce the fit range to $[t_i^{\rm tmp} + 1, t_f^{\rm tmp}]$ and repeat the above step until, either, we reach our prescribed minimum plateau length or until the change in effective mass *is* within the margin of error. This fit-range is our final answer.

There are a few ad-hoc parameters in the foregoing algorithm: the value of 40% in step 1, the requirement of 10% confidence of fit in condition 3b and the value of 2 in the exponent of $(t_f - t_i + 1)$ in eq. (C.0.1). A more detailed examination of this

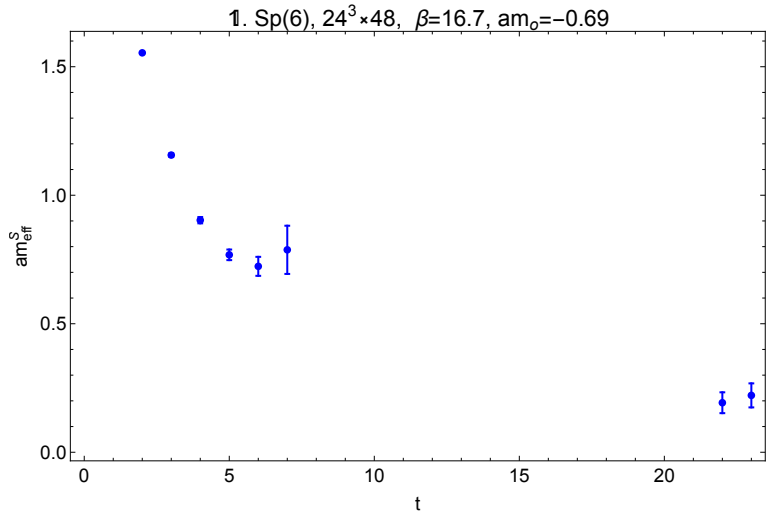

Figure C.1: An example of a mass signal that takes non-real values in the middle of the lattice. This plot has been included here for the sake of example but was not used in the final results.

algorithm, say, in the context of machine learning will almost certainly improve upon these values and even the algorithm as a whole. Such a study, however, is beyond the scope of this thesis.

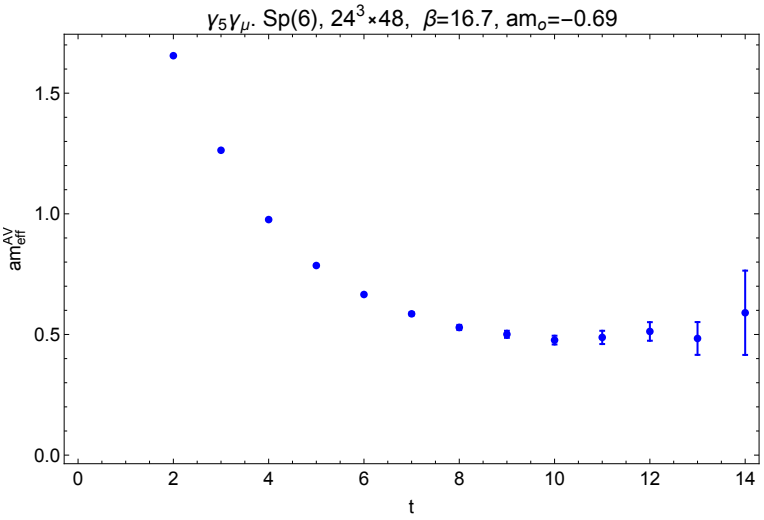

Figure C.2: An example of a valid mass signal that does not persist for the entire temporal width of the lattice. The temporal width of the lattice is 48 but the signal disappears for $t > 14$.

Bibliography

[1] H. Georgi and D. B. Kaplan, "Composite Higgs and Custodial SU(2)," *Phys. Lett. B*, vol. 145, pp. 216–220, 1984.

[2] D. B. Kaplan, H. Georgi, and S. Dimopoulos, "Composite Higgs Scalars," *Phys. Lett. B*, vol. 136, pp. 187–190, 1984.

[3] D. B. Kaplan and H. Georgi, "SU(2)×U(1) breaking by vacuum misalignment," *Physics Letters B*, vol. 136, no. 3, pp. 183–186, 1984.

[4] M. J. Dugan, H. Georgi, and D. B. Kaplan, "Anatomy of a composite Higgs model," *Nuclear Physics B*, vol. 254, pp. 299–326, 1985.

[5] E. Bennett, D. K. Hong, J.-W. Lee, C.-J. D. Lin, B. Lucini, M. Piai, and D. Vadacchino, "$Sp(4)$ gauge theory on the lattice: towards $SU(4)/Sp(4)$ composite Higgs (and beyond)," *arXiv e-prints*, p. arXiv:1712.04220, Dec 2017.

[6] L. Vecchi, "A dangerous irrelevant UV-completion of the composite Higgs," 2016.

[7] T. Ma and G. Cacciapaglia, "Fundamental composite 2HDM: $SU(N)$ with 4 flavours," *Journal of High Energy Physics*, vol. 2016, Mar 2016.

[8] G. Panico and A. Wulzer, "The Composite Nambu-Goldstone Higgs," *Lect. Notes Phys.*, vol. 913, pp. pp.1–316, 2016.

[9] O. Witzel, "Review on composite Higgs models," 2019.

[10] G. Cacciapaglia, G. Ferretti, T. Flacke, and H. Serdio, "Light scalars in composite Higgs models," *Frontiers in Physics*, vol. 7, Mar 2019.

[11] G. Cacciapaglia, C. Pica, and F. Sannino, "Fundamental composite dynamics: A review," 2020.

[12] G. Ferretti, "Gauge theories of partial compositeness: scenarios for Run-II of the lhc," *Journal of High Energy Physics*, vol. 2016, Jun 2016.

[13] E. Bennett, D. Hong, J.-W. Lee, C.-J. Lin, B. Lucini, M. Mesiti, M. Piai, J. Rantaharju, and D. Vadacchino, "$Sp(4)$ gauge theories on the lattice: Quenched fundamental and antisymmetric fermions," *Physical Review D*, vol. 101, 04 2020.

[14] E. Bennett, J. Holligan, D. K. Hong, J.-W. Lee, C.-J. D. Lin, B. Lucini, M. Piai, and D. Vadacchino, "Glueballs and strings in $Sp(2N)$ Yang-Mills theories," *Phys. Rev. D*, vol. 103, p. 054509, Mar 2021.

[15] V. Drach, P. Fritzsch, A. Rago, and F. Romero-López, "Singlet channel scattering in a composite Higgs model on the lattice," 2021.

[16] K. G. Wilson, "Confinement of quarks," *Physical Review D*, vol. 10, pp. 2445–2459, Oct 1974.

[17] A. Hietanen, R. Lewis, C. Pica, and F. Sannino, "Fundamental composite Higgs dynamics on the lattice: $SU(2)$ with two flavors," *Journal of High Energy Physics*, vol. 2014, Jul 2014.

[18] W. Detmold, M. McCullough, and A. Pochinsky, "Dark nuclei. II. nuclear spectroscopy in two-color QCD," *Physical Review D*, vol. 90, Dec 2014.

[19] R. Arthur, V. Drach, M. Hansen, A. Hietanen, C. Pica, and F. Sannino, "$SU(2)$ gauge theory with two fundamental flavors: A minimal template for model building," *Physical Review D*, vol. 94, Nov 2016.

[20] R. Arthur, V. Drach, A. Hietanen, C. Pica, and F. Sannino, "$SU(2)$ gauge theory with two fundamental flavours: Scalar and pseudoscalar spectrum," 2016.

[21] C. Pica, V. Drach, M. Hansen, and F. Sannino, "Composite Higgs dynamics on the lattice," *EPJ Web of Conferences*, vol. 137, p. 10005, 2017.

[22] J.-W. Lee, B. Lucini, and M. Piai, "Symmetry restoration at high-temperature in two-color and two-flavor lattice gauge theories," *Journal of High Energy Physics*, vol. 2017, Apr 2017.

[23] V. Drach, T. Janowski, and C. Pica, "Update on $SU(2)$ gauge theory with $n_f = 2$ fundamental flavours.," *EPJ Web of Conferences*, vol. 175, p. 08020, 2018.

[24] V. Ayyar, T. DeGrand, M. Golterman, D. C. Hackett, W. I. Jay, E. T. Neil, Y. Shamir, and B. Svetitsky, "Spectroscopy of $SU(4)$ composite Higgs theory with two distinct fermion representations," *Physical Review D*, vol. 97, Apr 2018.

[25] V. Ayyar, T. DeGrand, D. C. Hackett, W. I. Jay, E. T. Neil, Y. Shamir, and B. Svetitsky, "Baryon spectrum of $SU(4)$ composite Higgs theory with two distinct fermion representations," *Physical Review D*, vol. 97, Jun 2018.

[26] V. Ayyar, T. DeGrand, D. C. Hackett, W. I. Jay, E. T. Neil, Y. Shamir, and B. Svetitsky, "Finite-temperature phase structure of $SU(4)$ gauge theory with multiple fermion representations," *Physical Review D*, vol. 97, Jun 2018.

[27] V. Ayyar, T. DeGrand, D. C. Hackett, W. I. Jay, E. T. Neil, Y. Shamir, and B. Svetitsky, "Partial compositeness and baryon matrix elements on the lattice," *Phys. Rev. D*, vol. 99, no. 9, p. 094502, 2019.

[28] G. Cossu, L. Del Debbio, M. Panero, and D. Preti, "Strong dynamics with matter in multiple representations: $SU(4)$ gauge theory with fundamental and sextet fermions," *The European Physical Journal C*, vol. 79, Jul 2019.

[29] E. Bennett, D. K. Hong, J.-W. Lee, C.-J. D. Lin, B. Lucini, M. Piai, and D. Vadacchino, "$Sp(4)$ gauge theories on the lattice: $N_f = 2$ dynamical fundamental fermions," *Journal of High Energy Physics*, vol. 2019, Dec 2019.

[30] H. Georgi, "The Higgs as a pseudo-Goldstone boson," *Comptes Rendus Physique*, vol. 8, no. 9, pp. 1029–1047, 2007. The mystery of the Higgs particle.

[31] R. Foot, A. Kobakhidze, and R. R. Volkas, "Electroweak Higgs as a pseudo-Goldstone boson of broken scale invariance," *Physics Letters B*, vol. 655, p. 156161, Nov 2007.

[32] G. Ferretti and D. Karateev, "Fermionic UV completions of composite Higgs models," *Journal of High Energy Physics*, vol. 2014, Mar 2014.

[33] S. Laporta and E. Remiddi, "The Analytical value of the electron (g-2) at order α^3 in QED," *Phys. Lett.*, vol. B379, pp. 283–291, 1996.

[34] T. Aoyama, T. Kinoshita, and M. Nio, "Revised and Improved Value of the QED Tenth-Order Electron Anomalous Magnetic Moment," *Phys. Rev.*, vol. D97, no. 3, p. 036001, 2018.

[35] M. Tanabashi *et al.*, "Review of particle physics," *Phys. Rev. D*, vol. 98, p. 030001, Aug 2018.

[36] G. Aad *et al.*, "Observation of a new particle in the search for the Standard Model Higgs boson with the ATLAS detector at the LHC," *Phys. Lett.*, vol. B716, pp. 1–29, 2012.

[37] S. Chatrchyan *et al.*, "Observation of a New Boson at a Mass of 125 GeV with the CMS Experiment at the LHC," *Phys. Lett.*, vol. B716, pp. 30–61, 2012.

[38] P. W. Higgs, "Broken Symmetries and the Masses of Gauge Bosons," *Phys. Rev. Lett.*, vol. 13, pp. 508–509, 1964.

[39] P. W. Higgs, "Broken symmetries, massless particles and gauge fields," *Phys. Lett.*, vol. 12, pp. 132–133, 1964.

[40] F. Englert and R. Brout, "Broken symmetry and the mass of gauge vector mesons," *Phys. Rev. Lett.*, vol. 13, pp. 321–323, Aug 1964.

[41] P. W. Anderson, "Plasmons, gauge invariance, and mass," *Phys. Rev.*, vol. 130, pp. 439–442, Apr 1963.

[42] Y. Nambu, "Quasi-particles and gauge invariance in the theory of superconductivity," *Phys. Rev.*, vol. 117, pp. 648–663, Feb 1960.

[43] J. Goldstone, "Field theories with superconductor solutions," *Il Nuovo Cimento (1955-1965)*, vol. 19, pp. 154–164, Jan 1961.

[44] M. Thomson, *Modern Particle Physics*. New York: Cambridge University Press, 2013.

[45] M. Gell-Mann, "Symmetries of baryons and mesons," *Phys. Rev.*, vol. 125, pp. 1067–1084, Feb 1962.

[46] M. E. Peskin and D. V. Schroeder, *An Introduction to Quantum Field Theory*. Reading, USA: Addison-Wesley, 1995.

[47] S. L. Adler, "Axial-vector vertex in spinor electrodynamics," *Phys. Rev.*, vol. 177, pp. 2426–2438, Jan 1969.

[48] J. S. Bell and R. Jackiw, "A PCAC puzzle: $\pi^0 \to \gamma\gamma$ in the σ-model," *Nuovo Cimento A Serie*, vol. 60, pp. 47–61, Mar. 1969.

[49] K. Fujikawa, "Path-integral measure for gauge-invariant fermion theories," *Phys. Rev. Lett.*, vol. 42, pp. 1195–1198, Apr 1979.

[50] M. D. Schwartz, *Quantum Field Theory and the Standard Model*. Cambridge University Press, 3 2014.

[51] M. Gell-Mann and M. Levy, "The axial vector current in beta decay," *Nuovo Cim.*, vol. 16, p. 705, 1960.

[52] D. Tong, "Lectures on Gauge Theory: Chiral Symmetry Breaking," p. 243, Accessed: February 2021.

[53] E. Katz, A. E. Nelson, and D. G. E. Walker, "The Intermediate Higgs," *Journal of High Energy Physics*, vol. 2005, p. 074074, Aug 2005.

[54] E. Bennett, D. Ki Hong, J.-W. Lee, C.-J. David Lin, B. Lucini, M. Piai, and D. Vadacchino, "Higgs compositeness in $Sp(2N)$ gauge theories determining the low-energy constants with lattice calculations," *EPJ Web of Conferences*, vol. 175, p. 08011, 2018.

[55] M. Hamermesh, *Group theory and its Application to Physical Problems*. Reading, MA: Addison-Wesley, 1962.

[56] K. Holland, M. Pepe, and U.-J. Wiese, "The deconfinement phase transition of $Sp(2)$ and $Sp(3)$ Yang-Mills theories in 2+1 and 3+1 dimensions," *Nuclear Physics B*, vol. 694, p. 3558, Aug 2004.

[57] R. A. Diaz and R. Martinez, "The Custodial symmetry," *Rev. Mex. Fis.*, vol. 47, pp. 489–492, 2001.

[58] G. 't Hooft, "A Planar Diagram Theory for Strong Interactions," *Nucl. Phys. B*, vol. 72, p. 461, 1974.

[59] D. Tong, "Lectures on Gauge Theory: Large N," p. 286, Accessed: February 2021.

[60] C. Lovelace, "Universality at large-N," *Nuclear Physics B*, vol. 201, no. 2, pp. 333–340, 1982.

[61] D. K. Hong, J.-W. Lee, B. Lucini, M. Piai, and D. Vadacchino, "Casimir scaling and Yang-Mills glueballs," *Physics Letters B*, vol. 775, p. 8993, Dec 2017.

[62] N. Cabibbo and E. Marinari, "A New Method for Updating $SU(N)$ Matrices in Computer Simulations of Gauge Theories," *Phys. Lett. B*, vol. 119, pp. 387–390, 1982.

[63] A. Kennedy and B. Pendleton, "Improved Heat Bath Method for Monte Carlo Calculations in Lattice Gauge Theories," *Phys. Lett. B*, vol. 156, pp. 393–399, 1985.

[64] C. Gattringer and C. B. Lang, *Quantum Chromodynamics on the Lattice*. Springer, 2010.

[65] M. Teper, "An Improved Method for Lattice Glueball Calculations," *Physics Letters B*, vol. 183, pp. 345–350, Jan 1987.

[66] M. Albanese, F. Costantini, G. Fiorentini, F. Flore, M. P. Lombardo, R. Tripiccione, P. Bacilieri, L. Fonti, P. Giacomelli, E. Remiddi, M. Bernaschi, N. Cabibbo, E. Marinari, G. Parisi, G. Salina, S. Cabasino, F. Marzano, P. Paolucci, S. Petrarca, F. Rapuano, P. Marchesini, R. Rusack, and Ape Collaboration, "Glueball Masses and String Tension in Lattice QCD," *Physics Letters B*, vol. 192, pp. 163–169, Jun 1987.

[67] B. Lucini, M. Teper, and U. Wenger, "Glueballs and k-strings in $SU(N)$ Gauge Theories: Calculations with Improved Operators," *Journal of High Energy Physics*, vol. 2004, p. 012, Jun 2004.

[68] R. Johnson, "Angular momentum on a lattice," *Physics Letters B*, vol. 114, no. 2, pp. 147 – 151, 1982.

[69] B. Berg and A. Billoire, "Glueball spectroscopy in 4D $SU(3)$ Lattice Gauge Theory (I)," *Nuclear Physics B*, vol. 221, no. 1, pp. 109 – 140, 1983.

[70] K. Ishikawa, G. Schierholz, and M. Teper, "Calculation of the glueball mass spectrum of $SU(2)$ and $SU(3)$ non-abelian lattice gauge theories I: Introduction and $SU(2)$," *Zeitschrift für Physik C Particles and Fields*, vol. 19, pp. 327–352, Dec 1983.

[71] C. Michael, "The Glueball Spectrum From Lattice Gauge Theory," *Acta Phys. Polon.*, vol. B21, p. 119, 1990.

[72] B. Lucini, "Glueballs from the Lattice," *PoS*, vol. QCD-TNT-III, p. 023, 2013.

[73] H. J. Rothe, *Lattice gauge theories: An Introduction*, vol. 43. World Scientific, 1992.

[74] M. Luscher, K. Symanzik, and P. Weisz, "Anomalies of the Free Loop Wave Equation in the WKB Approximation," *Nucl. Phys. B*, vol. 173, p. 365, 1980.

[75] G. S. Bali, F. Bursa, L. Castagnini, S. Collins, L. Del Debbio, B. Lucini, and M. Panero, "Mesons in large-N QCD," *JHEP*, vol. 06, p. 071, 2013.

[76] B. Lucini, A. Rago, and E. Rinaldi, "Glueball masses in the large-N limit," *Journal of High Energy Physics*, vol. 2010, Aug 2010.

[77] B. Lucini and M. Panero, "$SU(N)$ gauge theories at large-N," *Physics Reports*, vol. 526, p. 93163, May 2013.

[78] A. Athenodorou and M. Teper, "$SU(N)$ gauge theories in 3+1 dimensions: glueball spectrum, string tensions and topology," 2021.

[79] A. Athenodorou, E. Bennett, G. Bergner, D. Elander, C.-J. D. Lin, B. Lucini, and M. Piai, "Large mass hierarchies from strongly-coupled dynamics," *Journal of High Energy Physics*, vol. 2016, Jun 2016.

[80] E. Bennett, J. Holligan, D. K. Hong, J.-W. Lee, C.-J. D. Lin, B. Lucini, M. Piai, and D. Vadacchino, "Color dependence of tensor and scalar glueball masses in Yang-Mills theories," *Physical Review D*, vol. 102, Jul 2020.

[81] H. Nielsen and M. Ninomiya, "A no-go theorem for regularizing chiral fermions," *Physics Letters B*, vol. 105, no. 2, pp. 219–223, 1981.

[82] G. Martinelli and Y.-C. Zhang, "The Connection Between Local Operators on the Lattice and in the Continuum and Its Relation to Meson Decay Constants," *Phys. Lett. B*, vol. 123, p. 433, 1983.

[83] G. P. Lepage and P. B. Mackenzie, "Viability of lattice perturbation theory," *Physical Review D*, vol. 48, p. 22502264, Sep 1993.

[84] S. Borsnyi, S. Drr, Z. Fodor, C. Hoelbling, S. D. Katz, S. Krieg, T. Kurth, L. Lellouch, T. Lippert, and et al., "High-precision scale setting in lattice QCD," *Journal of High Energy Physics*, vol. 2012, Sep 2012.

[85] M. Lüscher, "Properties and uses of the Wilson flow in lattice QCD," *Journal of High Energy Physics*, vol. 2010, Aug 2010.

[86] L. B. Okun, "THETA PARTICLES," *Nucl. Phys. B*, vol. 173, pp. 1–12, 1980.

[87] G. Aarts, "Introductory lectures on lattice QCD at nonzero baryon number," *J. Phys. Conf. Ser.*, vol. 706, no. 2, p. 022004, 2016.

Acronyms

χPT chiral perturbation theory. 119

χSB chiral symmetry breaking. 3, 5, 6, 11, 18–21, 24

CHM composite Higgs Models. 2, 18

EFT Effective Field Theory. 1, 3, 6, 10, 18, 21, 23, 24

EW Electroweak. 1, 5, 11, 19, 20

EWSB Electroweak symmetry breaking. 11, 20

GMOR Gell-Mann–Oakes–Renner. 18, 24

LFT Lattice Field Theory. 2, 25, 28

NGB Nambu-Goldstone bosons. 7, 11, 14, 18

NLO next-to-leading order. 119

NNT Nielsen-Ninomiya Theorem. 107, 108

PNGB pseudo-Nambu-Goldstone boson. 3, 11, 20, 21, 24

QCD Quantum Chromodynamics. viii, 5, 11–13, 15–18, 24, 25, 28, 29, 53, 109, 119, 158

QED Quantum Electrodynamics. 27, 28, 31

QFT Quantum Field Theory. 1, 6, 109

SM Standard Model. 1–3, 5–11, 19, 20, 157

SSB spontaneous symmetry breaking. 7, 8, 20

VEV vacuum expectation value. 9, 15, 17, 56, 58, 71